

NEURAL SYSTEMS MODELING

– THREE CASE STUDIES

A Dissertation presented to
The Faculty of the Graduate School
University of Missouri – Columbia

In Partial Fulfillment
of the Requirements for the Degree
Doctor of Philosophy

by

CHARLIE FRANKLIN

Dr. Satish S. Nair, Dissertation Supervisor

MAY 2017

The undersigned, appointed by the Dean of the Graduate School, have examined the dissertation entitled

NEURAL SYSTEMS MODELING

–THREE CASE STUDIES

presented by Charlie Franklin

a candidate for the degree of Doctor of Philosophy

and hereby certify that in their opinion it is worthy of acceptance.

Dr. Satish S. Nair

Dr. David Schulz

Dr. Guilherme DeSouza

Dr. Naz Islam

ACKNOWLEDGEMENTS

I would like to express my appreciation and gratitude to my advisor, Dr. Satish Nair, for the guidance and mentorship he provided me, from my honors research as a freshman, to my undergraduate research as a senior, through to the completion of this degree. I am fortunate to have had the opportunity to work with him.

I would also like to thank my committee members, Dr. David Schulz, Dr. Guilherme DeSouza, and Dr. Naz Islam for their friendly guidance and suggestions offered to me throughout my graduate studies.

TABLE OF CONTENTS

ACKNOWLEDGEMENTS	ii
LIST OF ILLUSTRATIONS	iv
LIST OF TABLES	v
CHAPTER 1 Introduction.....	1
CHAPTER 2 Generation and preservation of the slow underlying membrane potential oscillation in a model bursting neuron.....	5
CHAPTER 3 Cellular and synaptic correlates of pattern formulation in a hippocampal model.....	50
CHAPTER 4 Genesis of Hippocampal Theta Rhythm in a Computational Model.....	101
CHAPTER 5 Summary.....	137
APPENDICES	142
PUBLICATIONS.....	147
VITA.....	149

LIST OF ILLUSTRATIONS

Figure	Page
1. The underlying membrane potential oscillations and corresponding currents for the three example cases	43
2. The underlying membrane potential oscillations resulting from variations in conductance of each of the individual currents in the LC	44
3. Relationships among conductances in the proposed modules for the LC	45
4. Relationships among conductances in the proposed current modules for the AB cell and <i>Aplysia</i> R15 cell	47
5. The changes in peak and duration of the underlying oscillation in AB and <i>Aplysia</i> R15	49
6. Structure and characterization of the 3D hippocampal network	97
7. Morphology of inhibitory connections in the CA3 network	98
8. Distinctive features of inhibition by BCs and OLM cells	99
9. Comparison of effects of back-projection from CA3 to DG	100
10. Network 3D structure and CA3 local circuitry	131

LIST OF TABLES

Table	Page
1. Biophysical details of example case 1 (cardiac ganglion LC)	41
2. Parameter values for CA3 PNs.....	92
3. Parameter values for DG PNs	93
4. Parameter values for BC and OLM cells	94
5. Summary of synaptic properties used in the CA3 network model.....	132
6. CA3 cell parameter values	134
7. DG cell parameter values	135
8. BC and OLM cell parameter values	136

CHAPTER 1 – INTRODUCTION

Neuroscience attempts to better understand the function and behavior of neurons and networks in the brain and body. Computational neuroscience has grown as a research field to provide an important tool and aid in the study of neuroscience. Beginning with the work of Hodgkin and Huxley to study mathematical properties of ionic currents in a squid axon, mathematical models of neurons and their ionic currents have been extensively studied and developed. The mathematical models represent neurons as equivalent circuits to study their electrical properties. These neuron models can be combined into larger networks to study network behavior of biological structures. Computational models allow neuroscientists to test hypotheses much faster than physical experiments on biological cells, for example in changing parameters of neurons that would be very time consuming and difficult in biological experiments. These models can be used to make predictions to assist neuroscientists. Neuroscientists can use the predictions to focus their biological experiments to work more efficiently and have a higher rate of success in their experiments. Any results obtained in biological experiments can be used to make the model more accurate and improve its predictive value.

Models of biological networks allow neuroscientists to study biological systems in ways that biological experiments cannot. While single cell neuron models attempt to replicate the membrane potential and ionic current behavior of individual neurons, network models connect many individual cell models with synaptic connections to study the interaction and communication between cells in a biological system. Network models can simultaneously track and analyze the behavior of hundreds or even thousands of individual neurons and the synaptic connection activity between them. This gives neuroscientists

another tool to study complex biological systems to help understand the underlying mechanisms and functions of biological phenomena that take place in large biological structures.

The mathematical equations that describe these behaviors of the neurons and their ionic currents are often highly nonlinear and therefore do not have an analytical solution. Computer simulation must be used to simulate the ionic currents and cell potentials over time. Biologically realistic models select parameter values to match biological cell values in an attempt to reproduce the ionic currents and cell potentials as closely as possible to actual biological cell recordings.

This dissertation involves three studies of computational models at both the individual neuronal level and the network level. Each study is presented in the form of a stand-alone journal article as described below.

1. *Generation and preservation of the slow underlying membrane potential in a model bursting neuron.* A biophysical model of a class of slow-wave bursting cells with six active currents was developed to investigate and generalize correlations among maximal current conductances that might generate and preserve its underlying oscillation. The underlying oscillation of the membrane potential was divided into three phases: generation, maintenance, and termination. The contributions of this study include: i) suggestion that different current modules can co-regulate to preserve the characteristics of each phase, ii) co-regulation of a burst current and a potassium current within distinct boundaries maintains the dynamics during the generation phase, iii) co-regulation of a transient calcium and a delayed rectifier potassium current maintain the peak and duration

of the underlying oscillation, and iv) a calcium-activated potassium current ensures appropriate termination of the oscillation while adjusting duration independent of the peak.

2. Cellular and synaptic correlates of pattern formulation in a hippocampal model.

We adapted a computational network model of the hippocampus to include biologically realistic conductance-based cells in CA3 and dentate gyrus (DG) regions. Single cell biophysical models were developed for principal cells and the two abundant interneuron types in CA3, basket cells (BCs) and for oriens lacunosumoleculare (OLM) interneurons. The network model included synaptic current dynamics, spatial connectivity patterns, short-term synaptic plasticity, and known effects of acetylcholine, and enabled an investigation into the cellular and synaptic correlates of pattern formation in CA3, when a specific pattern is projected from the entorhinal cortex (EC). The contributions of this study include: i) inhibition was found to be the dominant factor influencing the recruitment of a CA3 cell into a pattern, ii) differential connectivity and inhibitory dynamics between BCs and OLM cells enabled the former to control the recruitment of specific pyramidal cells into the CA3 pattern, and the latter to regulate pattern size, iii) BCs and OLM cells participate in a disynaptic inhibitory mechanism, and iv) biological realism in both connectivity and cell types also suggested that back-projections from CA3 to DG both stabilized patterns in CA3, and also helped increase pattern storage capacity in CA3.

3. Genesis of Hippocampal Theta Rhythm in a Computational Model.

The mechanisms involved in the generation of hippocampal theta remain poorly understood. We have outlined the procedure to study the genesis of theta by adapting a computational network model of the rodent hippocampus. The model had biologically realistic conductance-based single cells models for principal cells and the two abundant interneuron

types in CA3 and dentate gyrus (DG) regions. The interneuron types were, basket cells (BCs) and oriens lacunosum-moleculare (OLM) interneurons, and the present study incorporated realistic gap junction and chemical synapse connectivity among and between these interneurons. The network model also included synaptic current dynamics, spatial connectivity patterns, short-term synaptic plasticity, and known effects of acetylcholine.

CHAPTER 2

GENERATION AND PRESERVATION OF THE SLOW UNDERLYING MEMBRANE POTENTIAL OSCILLATION IN MODEL BURSTING NEURONS

ABSTRACT

The *underlying membrane potential oscillation* of both forced and endogenous slow-wave bursting cells affects the number of spikes per burst which in turn affects outputs down-stream. We use a biophysical model of a class of slow-wave bursting cells with six active currents to investigate and generalize correlations among maximal current conductances that might generate and preserve its underlying oscillation. We propose three phases for the underlying oscillation for this class of cells: generation, maintenance, and termination, and suggest that different current modules co-regulate to preserve the characteristics of each phase. Co-regulation of I_{Burst} (I_B) and I_A currents within distinct boundaries maintains the dynamics during the generation phase. Similarly, co-regulation of I_{CaT} and I_{Kd} maintains the peak and duration of the underlying oscillation, while the calcium-activated I_{KCa} ensures appropriate termination of the oscillation, and adjusts the duration independent of peak.

INTRODUCTION

Ultimately the output of a given neuron type is most directly determined by the makeup and characteristics of voltage-gated ion channels inserted in the membrane at a given time. Yet neurons exhibit remarkably robust electrical behavior even when underlying biological parameters of the same cells in different individuals show a great

deal of variability (Golowasch et al. 1992; Swensen and Bean 2005; Schulz et al. 2006; Khorkova and Golowasch 2007). A compelling question from this phenomenon is how the individual components of biological cells possess variable underlying mechanisms and yet converge to generate highly similar functional output. One possibility is that different ionic conductances compensate for one another, and potentially are co-regulated, in order to maintain a particular output. For example, at the level of mRNA, quantitative single-cell PCR analyses on individual neurons of the stomatogastric ganglion (STG) revealed different sets of correlated ion channel mRNA levels in each class of identified neuron (Schulz et al. 2007), some of which have been demonstrated to hold true at the level of membrane conductance (Khorkova and Golowasch 2007), suggesting that cellular output in the STG may be determined in part by characteristic sets of correlated expression of ion channel genes and their subsequent ionic currents. This hypothesis is strongly supported by the fact that over-expression of a hyperpolarizing conductance (G_A) in the pyloric dilator neuron of the STG leads to very little or no change in its activity via a compensatory upregulation of a depolarizing conductance (G_H) (MacLean et al. 2003, 2005). These results suggest that positive co-regulation of G_A and G_H exerts a stabilizing force on bursting output in these cells, thus *maintaining* the cells in a parameter space that allows for appropriate activity.

Alternatively, there is evidence that when faced with more radical alterations to their output, cells can decouple these stabilizing mechanisms in order to regain, *de novo*, their patterns of activity. For example, when STG neurons are cultured in isolation, they undergo dramatic changes in their firing patterns, from silent to tonic spiking until finally they recover a bursting phenotype (Turrigiano et al. 1995; Haedo and Golowasch 2006).

Underlying these changes in firing patterns are a negative relationship between depolarizing (G_{Ca}) and hyperpolarizing (G_K) conductances (Olypher and Prinz 2010); G_{Ca} and G_{Na} (depolarizing conductances) are up-regulated while G_K (hyperpolarizing conductances) are down-regulated (Turrigiano et al. 1995; Haedo and Golowasch 2006). These results suggest that when forced into a parameter space that does not produce appropriate output, there is a decoupling of stabilizing co-regulation that allows cells to travel *across* parameter space to achieve bursting output.

Motivated by these biological phenomena, the present paper investigates common mechanisms for robustness of a particular characteristic of a class of slow-wave bursting cells, the ‘underlying membrane potential oscillation’. The underlying oscillation, which is revealed in the membrane potential trace if the spikes are removed (e.g., see Fig. 1), determines the number of spikes per burst for such cells, which in turn affects outputs down-stream, such as muscle actuation. We use a biophysical modeling approach to examine the parameter space that allows for such underlying oscillations, in order to determine both potential co-regulations among currents that might preserve this oscillation for slow-wave bursting cells, as well as how discrete boundaries may exist between conductances that shift a cell from oscillatory to other forms of firing.

Underlying oscillation controls burst characteristics. Underlying oscillations can lead to bursting in both forced and endogenous bursters. In forced bursters, such oscillations are typically elicited in response to a synaptic stimulus, and are also referred to as ‘driver potentials’ by some authors (e.g., Tazaki and Cooke 1979). An underlying oscillation in such a cell is a graded depolarization from rest and re-polarization to rest of the cell on the

order of a few hundred milliseconds. The depolarization is typically 20-30 mV above the resting state. There are numerous mechanisms that cells use to generate a bursting phenotype (see Coombes and Bressloff (2005) and Izhikevich (2003, 2007) for comprehensive surveys). The classification of bursters using phenomenological models has been well studied. Izhikevich (2007) lists various types of fast-slow bursters for a class of such mathematical model systems. However, such a classification of bursters from an electrophysiology perspective is lacking presently.

Our primary test case in this modeling study, the large cell (LC) of the crab cardiac ganglion, is a motor neuron characterized as a forced burster that exhibits a typical driver potential profile. An underlying oscillation in the LC occurs with a depolarization driven mainly by Ca^{2+} currents and with repolarization driven by K^{+} currents (Tazaki and Cooke 1979, 1986, 1990; Berlind 1982; Cooke 2002). Similar calcium currents have also been implicated in depolarization during bursting in lamprey spinal motoneurons (Grillner et al. 2001), and low-threshold calcium currents have been shown to be involved in the rhythmic activity of leech heart interneurons (Ivanov and Calabrese 2000). Bursts can be initiated by increased calcium or persistent sodium currents, or by decreased potassium currents, and a combination of these mechanisms is typically used (Harris-Warrick 2002). An initial study of the relationships of ion channel mRNA copy numbers revealed strong correlations in channel expression in LCs. Among these was a robust relationship between *cacophony*, which encodes a voltage-gated calcium channel, and *shab*, which encodes a delayed rectifier conductance (Tobin et al. 2009). Based on these observations, Ball et al. (2010) used a computational model to show that co-variations in a potentially related set of ionic conductances (G_{CaT} and G_{Kd}) preserves the peak and duration of driver potentials

of LCs in a crab cardiac ganglion. In our study, in addition to extending the investigation of co-variation to other conductances in the LC, we generalize this concept to two other types of slow-wave bursting neurons with distinct intrinsic underlying oscillations. The biophysical models reported in the present paper elucidate the development of the underlying membrane potential oscillation for such cells from a biologically realistic, i.e., electrophysiology, perspective.

Hypothesis about phases of the underlying oscillation. The sum total of these experimental and modeling studies led us to hypothesize that the underlying oscillation for a slow-wave bursting cell has three phases: generation, maintenance, and termination, and that different currents or “modules” of currents are co-regulated to preserve the characteristics of each phase. *Generation* is the phase where the underlying oscillation is initiated, by a synaptic pulse for the forced case, and intrinsically for the endogenous case. The peak and duration of the oscillation are controlled during the *maintenance* phase. *Termination* (or repolarization) is the phase where the underlying oscillation ends and the membrane potential is brought back to its rest value.

We investigated whether distinct modules of ionic currents were primarily responsible for the different phases of *generation*, *maintenance* (of peak value and duration), and *termination* of the underlying oscillation, and if so, whether they co-varied to preserve the peak and duration of the underlying oscillation. We investigated these hypotheses using the LC model studied by our group (Ball et al. 2010), a forced burster cell that has six active currents I_B , I_A , I_{Na} , I_{CaT} , I_{Kd} and I_{KCa} , and a passive leak current. We then investigated whether the correlations were preserved for randomly selected points in

the LC maximal conductance parameter space, and then devised yet another strategy to test their validity. We considered the question “Would the correlations hold for other types of cells reported in the literature that expressed the same set of conductances?” This led us to consider example cases 2 and 3, the anterior burster (AB) neuron of the STG (Soto-Treviño et al. 2005) and the *Aplysia* R15 neuron (Bower and Beeman 1998), using models reported in the literature.

METHODS

We considered two properties to characterize the slow underlying membrane potential oscillation, its peak and duration. The highest value of the membrane potential was defined as the *peak* of the slow underlying membrane potential oscillation. *Duration* of the oscillation was calculated, as in Tazaki and Cooke (1979), by extending lines down from the points of maximum rates of rise and fall of the oscillation, in the membrane potential vs. time plot. Duration was the time between the intersections of these two lines with the resting potential of the cell (Ball et al. 2010; fig SM1 in the supplementary material). In the endogenous cases, resting potential was taken to be the value of the membrane potential immediately prior to the upswing of an underlying oscillation.

Example Case 1: The cardiac ganglion large cell (LC) is a forced burster, and a model with two compartments was developed using biological data (Ball et al. 2010). The soma compartment contained the following currents: two calcium currents - a persistent calcium current I_{CaS} (referred to as the burst current I_B in the following) and a transient calcium current I_{CaT} ; three potassium currents – an early transient potassium current I_A , a delayed

rectifier potassium current I_{Kd} , and a calcium-dependent potassium current I_{KCa} ; and a leak current. The axon compartment contained the fast I_{Na} and I_{Kd} currents responsible for action potential generation. This model is described in more detail below. The effects of the sodium current I_{Na} were blocked to observe the dynamics of the underlying oscillation. There was no significant change in the shape of the underlying oscillation with I_{Na} present (data not shown; also seen somewhat in some figures in Cooke 2002) and so I_{Na} was blocked for ease of analysis.

Example Case 2: The second example is an anterior burster (AB) neuron, an endogenous oscillator of the crab STG from Soto-Treviño et al. (2005). The AB model has two compartments, a soma and an axon. The soma contained all currents in example case 1 (two calcium currents, three potassium currents, and the leak current), while the axon compartment contained the fast I_{Na} and I_{Kd} currents responsible for action potential generation. Again, blocking the sodium current had an insignificant effect on the shape of the underlying oscillation, and so this was continued for ease of analysis.

Example Case 3: The third example case is an *Aplysia* R15 ‘regular burster’ cell that generates an endogenous, regular, pattern of bursts. It was modeled after the *Aplysia* R15 cell at temperatures below 16°C, and it contained channel models taken from measurements on bursting neurons in *Tritonia* and *Anisidoris* (Bower and Beeman 1998). The model consisted of a single compartment that contained all of the currents cited for the soma compartment of the previous models, as well as a fast sodium current I_{Na} . I_{Na} was not blocked in this case to allow for activation of the high threshold current I_{CaT} that otherwise

fails to activate at lower voltages. The burst current (I_B) was a mixture of I_{CaS} and I_{NaP} in this case, providing the underlying generation current, and so they were co-varied and considered as a single burst current I_B for this example case. Since this model includes spiking, the underlying oscillation was obtained by filtering the high frequency spikes using a first order low-pass filter with a time constant of 0.5 sec. This filtered response (dashed line in Fig. 1C) was used to calculate peak and duration of the underlying oscillation.

We provide below the modeling details pertaining to example case 1, the LC. The models for the example cases 2 and 3 cells reported in the literature use the same form for membrane and current kinetics, and so are not reported here. The parameter values for example cases 2 and 3 were obtained from the literature, and can also be found in the supplementary material.

Model of crustacean cardiac ganglion LC – Example Case 1

We use the LC model to illustrate the basic structure of the biophysical equations that have the same form for all example cases. In LCs, driver potential (underlying oscillation) generation and the associated conductances appear to be located in the soma, while action potentials are produced distally in the axon (Tazaki and Cooke 1979b). Studies of LCs have shown that an inward calcium current is responsible for depolarization in the driver potential (Tazaki and Cooke 1979a, 1979b, 1983b, 1986, 1990). Analyses of tail currents (Tazaki and Cooke 1990) revealed that calcium current inactivation occurs with two apparent time constants, a shorter time constant of 40 ms, followed by a longer time constant of 180 ms. Two types of calcium currents were implemented in the model to

reproduce this behavior: a persistent calcium current I_{CaS} and a transient calcium current I_{CaT} . Three outward potassium currents have been found in LCs (Tazaki and Cooke 1979a, 1986): an early outward current I_A , a delayed outward current I_{Kd} , and a calcium-dependent potassium current I_{KCa} . The soma was modeled with these five active currents and a leak current. The axonal compartment was modeled with transient sodium current I_{Na} , I_{Kd} and a leak current to produce action potentials in response to depolarizing currents.

Eqns. 1 and 2 represent the membrane voltage equations for the two compartments of the LC,

$$C_s \frac{dV_s}{dt} = -g_{Ls}(V_s - E_{Ls}) - g_c(V_s - V_a) - \sum I_s^{\text{int}} \quad (1)$$

$$C_a \frac{dV_a}{dt} = -g_{La}(V_a - E_{La}) - g_c(V_s - V_a) - \sum I_a^{\text{int}} \quad (2)$$

where V_s/V_a are the somatic/axonal membrane potentials, $I_s^{\text{int}}/I_a^{\text{int}}$ are the intrinsic currents in the soma/axon compartments; C_s/C_a are the membrane capacitances of the soma/axon compartments; g_{Ls}/g_{La} , and E_{Ls}/E_{La} represent the leak conductance and reversal potential for the soma/axon compartments, and g_c is the coupling conductance between the soma and the axon. The passive properties of the model were adjusted to reproduce the input resistance and resting potential of LCs recorded *in vitro*. The values for the leak conductance, membrane capacitance and cytoplasmic (axial) resistance are listed in Table 1.

Current kinetics. The cells in the crustacean cardiac ganglion share many similarities in form and function with those in the well-studied STG (Buchholtz et al. 1992; Golowasch et al. 1992; Turrigiano et al. 1995; Prinz et al. 2003; Prinz et al. 2004). Accordingly,

kinetics of the currents in the LC model and the ranges for maximal conductances were based on the current models in a database of model STG neurons (Prinz et al. 2003). The ionic current for channel i was modeled as $I_i = g_i m^p h^q (V - E_i)$, where g_i is its maximal conductance, m its activation variable (with exponent p), h its inactivation variable (with exponent q), and E_i its reversal potential. The kinetic equation for each of the gating variables x (m or h) takes the form

$$\frac{dx}{dt} = \frac{x_\infty(V, [Ca^{2+}]) - x}{\tau_x(V)} \quad (3)$$

where x_∞ is the voltage- and/or calcium-dependent steady state and τ_x is the voltage-dependent time constant. The maximal conductances for all ionic currents and the expressions for the gating variables x_∞ and τ_x , were largely the same as in the STG database (Prinz et al. 2003), and are listed in Table 1.

Calcium dynamics. Intracellular calcium modulates the conductance of the calcium-activated potassium current and influences the magnitude of the inward calcium current in the LC (Tazaki and Cooke 1990). A calcium pool was modeled in the LC with its concentration governed by the first-order dynamics of Eqn. 4 (Prinz et al. 2003; Soto-Treviño et al. 2005),

$$\frac{d[Ca^{2+}]}{dt} = -F \times I_{Ca} - \frac{[Ca^{2+}] - [Ca^{2+}]_{rest}}{\tau_{Ca}} \quad (4)$$

where $F=0.256 \mu\text{M/nA}$ is the constant specifying the amount of calcium influx that results per unit (nA) inward calcium current, and τ_{Ca} represents the calcium removal time constant from the pool. Voltage-clamp experiments of the calcium current in the LC (Tazaki and Cooke 1990) showed the intracellular calcium buffering time constant to be

640 ms, and so this value was used for τ_{Ca} . This calcium concentration was also used in the Nernst equation to determine the reversal potential for calcium currents, assuming an extracellular calcium concentration of 13 mM, at a temperature of 25°C, as used in electrophysiological experiments by Tazaki and Cooke (1979a, 1979b, 1979c).

As mentioned, example cases 2 and 3 also had the same currents as example case 1, resulting in the same set of equations 1-4, albeit with different parameters and activation/inactivation functions (see supplementary material Tables SM1 and SM2). The activation values for the *Aplysia* R15 model were used in table form from experimental values (Bower and Beeman 1998). All the models have been validated by their authors (Bower and Beeman 1998; Soto-Treviño et al. 2005; Ball et al. 2010). For the present study, the models for all the example cases were developed using the General Neural Simulation System (GENESIS; Bower and Beeman 1998), with an integration time step of 10 μ s.

RESULTS

Slow underlying oscillations in the nominal model

The nominal models of the three example cases produced underlying membrane potential wave forms with the following characteristics: the LC model had a peak of -31 mV and a duration of 283 ms; the AB model had a peak of -27 mV and duration of 151 ms; and the *Aplysia* R15 model had a peak of -38 mV and duration of 10.4 s. Figure 1A shows the plots of the LC currents that made up the underlying oscillation initiated after a current pulse of 40 nA for 20 ms (see Ball et al. 2010). The initial spike in the voltage and currents in Fig. 1A was a result of this current pulse. Note that the other two example cases are endogenous bursters and so do not require such input pulses. The underlying membrane potential oscillations and the corresponding currents for the AB and *Aplysia* R15 cells are

shown in Figs. 1B and 1C, respectively. The membrane potential in Fig. 1C exceeded 0 mV at the peak of action potentials, but was cut off at -30 mV to focus on the underlying slow wave oscillation. The current plot in Fig. 1C was also zoomed in to the -50 to 50 nA scale to focus on the slow currents.

Effects of maximal conductance variations of individual currents. We began our investigation of the effects of altering maximal conductances with the LC model. All five maximal conductances were varied individually to 0.5, 3 and 5 times their nominal value, to investigate the effect on duration and peak of the underlying membrane potential oscillation. Representative results for LC are shown in Fig. 2, where the small arrows indicate traces that represent silent and endogenous behaviors. Increasing G_B from 0.5 to 5 times its nominal value resulted in moving the cell progressively from not producing an underlying oscillation at 0.5 times the nominal value, to a forced burster at the nominal value, and then to an endogenous burster at 3 and 5 times nominal value (Fig. 2A). Changing only G_A across the same range had exactly the opposite effect, i.e., increasing G_A over this range moved the cell progressively from being a forced burster to not producing an underlying oscillation (Fig. 2B). Increasing only G_{CaT} from 0.5 to 5 times its nominal value caused the peak to increase by 18% and the duration to decrease by 64%, as shown in Fig 2C. Actual values for peak and duration for the plots in Figs. 2A-2E are given in Fig. 2F. Similar changes to G_{Kd} had exactly opposite effects to those of G_{CaT} , i.e., increasing G_{Kd} from 0.5 to 3 times its nominal value decreased peak by 46% and increased duration by 175% (Fig. 2D). Increasing the conductance to 5 times its nominal value caused the cell to become silent. A cell was considered silent if the membrane potential did not rise more

than 10 mV above its ‘rest’ membrane potential. Finally, increases in only G_{KCa} from 0.5 to 5 times the nominal value had little effect on the peak, reducing it by only 3%, while it caused a decrease in duration of 34% (Fig. 2E). The results in Fig. 2 suggested pairs of currents that might oppose each other in their effects on membrane potential characteristics, which we then investigated as possible ‘modules’ subject to co-regulation.

The currents in the other example cases, the AB cell and the *Aplysia* R15 cell, exhibited similar characteristics, but both were endogenous oscillators at nominal conductance values. Peak and duration values for individual current conductance variations for the AB cell and the *Aplysia* R15 cell are shown in supplementary material Tables SM3A and SM3B respectively. In both cells, increasing only G_A (to 1.5 times the nominal value for AB and to 4 times for *Aplysia* R15) caused the cell to cease endogenous oscillation. Decreasing only G_B (to 0.5 times the nominal value for AB and to 0.2 times for *Aplysia* R15) also gave the same result. Increasing only G_{CaT} across the same range (0.5 to 5 times the nominal) caused an increase in peak (AB: 29.6%, R15: 8%) and a simultaneous decrease in duration (AB: 60.9%, R15: 46.5%) for both AB and *Aplysia* R15 models. Increasing only G_{Kd} over the range caused both lower peaks (AB: 25.9%, R15: 2.9%) and shorter durations (AB: 45.7%, R15: 60.9%). In both models, increasing only G_{KCa} reduced the duration (AB: 18%, R15: 51.2%) with a saturation effect, but with little effect on peak height (AB: 3.7%, R15: 5%). Decreasing only G_{KCa} below nominal values lengthened the duration. These trends were similar to those seen for example case 1.

Role of current modules in various phases of the underlying oscillation of the LC

We first set out to exhaustively examine the role of the ionic conductances as combined units, or ‘modules’, in the generation, maintenance, and termination of bursting activity using one of our model cells, the LC of the cardiac ganglion.

Generation of the underlying oscillation. Increases in only G_B from 0.5 to 5 times its nominal value caused the LC to move from silent, to forced bursting, to endogenous bursting. The exact opposite behavior was observed when increases in only G_A were considered, raising the question whether G_B and G_A might co-regulate to preserve the generation of the slow underlying oscillation. We hypothesized that the pair G_B and G_A act as the ‘generation module’, and thus we varied both the conductances proportionally, i.e., co-varied them, to investigate the effects on the underlying oscillation.

For the LC, which is a forced burster, the underlying oscillation had to be initiated by an input pulse that was sufficiently strong to activate I_B which then began the generation of an oscillation. For the LC, a 40nA 20ms pulse was chosen for the plots in Fig. 3. Ball et al. (2010) showed that the underlying oscillation had similar peaks and durations even with variations in input stimulus amplitude. Since I_A countered I_B during the generation of the underlying oscillation, we investigated whether there was a boundary in the G_B - G_A parameter space to separate a forced burster from an endogenous one, and similarly, separated a forced burster from a “silent” cell (i.e., a cell that does not produce an underlying oscillation in response to a given input stimulus). Our investigation led to the finding of two characteristic boundary lines for the LC, as shown in Fig. 3A1 (note that the nominal model has a multiplier of 1 for G_A and G_B). Data points in Fig. 3A1 were generated

by specifying fixed values of either G_A or G_B , then increasing or decreasing the other conductance incrementally until the generation dynamics were changed. All other conductances were kept at nominal values. The solid upper line delineates the boundary between forced and endogenous oscillations, and the lower dashed line separates the forced bursters from the silent cells. For instance, if G_B is increased from a point below this boundary to one above it, keeping G_A constant, the cell will transition from a forced burster to an endogenous one. The upper boundary is not affected by the strength of the stimulus since the entire line is a bifurcation line (Izhikevich 2007) for the system as G_B and G_A are varied. The line separates endogenous from non-endogenous behavior and no stimulus is needed to generate oscillations above the line. If, on the other hand, the cell is located in the middle of the forced burster (meaning it is silent without an input stimulus) region and G_A is increased keeping G_B constant, the cell moves below the lower boundary line into the silent region where no oscillation can be initiated with the given input stimulus.

Increasing the input stimulus beyond the nominal value lowered the dashed line (and vice versa), as expected, since a stronger input pulse requires less G_B to initiate the oscillation. Conversely, a larger G_A is required to prevent the oscillation with a stronger pulse. Since I_B is activated during the pulse, and is responsible for initiating the underlying oscillation, stronger pulses increasingly activated I_B . If the input pulse is stronger, the underlying oscillation can be initiated with a smaller G_B but more activated I_B . Therefore, stronger input pulses lowered the boundary for initiation along the G_B axis. Doubling the length of the input stimulus lowered the initiation boundary line by 14%, while a doubling of both length and magnitude of the stimulus lowered it by 36%.

Examination of the effects of varying the other conductances revealed that G_{Kd} could be viewed as having a role in the ‘generation module’; higher multiples of G_{Kd} resulted in shifting the LC from a forced burster to a silent cell (Fig. 2D). To investigate the role of G_{Kd} in the generation of bursting, we added this conductance to the co-variance experiments with G_B and G_A . While G_{Kd} was able to suppress bursting activity at high conductance values ($> 4x$ multiplier), this conductance made no substantial impact on the boundary lines that separated the regions of generation (Fig. 3A2), and thus was not considered to be part of the generation module. The effect of G_{CaT} was on the generation boundaries was also studied. As shown in Fig. 3A2, increasing G_{CaT} from 1 to 5 times the nominal value did lower the endogenous boundary, but not substantially, and so this current was not considered to be part of the generation module.

Maintenance of the underlying oscillation. Previous modeling experiments in the LC have shown that the peak and duration of the underlying oscillation can be preserved by I_{CaT} and I_{Kd} (Ball et al. 2010). Our non-intuitive finding from examining the individual current conductance variations in Figs. 2C and 2D (see also 2F), indicated, in addition, that increasing only G_{CaT} decreased the duration of the oscillation, and increasing only G_{Kd} increased it. To study the potential relationship between G_{CaT} and G_{Kd} in preserving peak and duration of the oscillation, each was varied from 0.5 to 5 times its nominal values across the 2-dimensional space.

As cited, the nominal LC model produced an underlying membrane potential oscillation with a peak of -31 mV and duration of 283 ms. For comparison with biological ranges, in biological recordings from 79 cells, the oscillation duration had a mean of 250

ms with a SD of 50 ms, and the peak had a mean of -32 mV and SD of 3 mV (Tazaki and Cooke 1979b). This represents a SD of 20% of the mean for duration. Figures 3B1 and 3B2 show the % changes in peak and duration values, respectively, as G_{CaT} and G_{Kd} are varied from 0.5 to 5 times their nominal values (with all other G_i constant). The figures were generated using peak and duration data at every .5 multiple of G_{CaT} and G_{Kd} in the two-dimensional space. MATLAB was then provided the data at the grid points (shown by dots in the figures) and its contour plot utility generated the trends shown. The positive (negative) directional arrows indicate increasing (decreasing) peaks and durations. They show that a 1:1 variation might help preserve both features, with a deviation of 13% in peak and 7% in duration for a 5x increase in nominal values for both conductances.

How should the ratio of $G_{CaT}:G_{Kd}$ vary to best maintain the peak and duration of the oscillation? Our model experiments showed that this was dependent on the nominal biological values of the conductances. In the nominal LC cell, equal increases in both G_{CaT} and G_{Kd} strengthened I_{CaT} disproportionately, yielding larger peaks and shorter durations for the underlying oscillation. Using this insight, we were able to determine that a 1:1.1 ratio in variations of $G_{CaT}:G_{Kd}$ best preserved the features (see Table SM4 in the supplementary material for numerical estimates). The ratio for co-regulation will thus depend on the relative strengths of G_{CaT} and G_{Kd} at nominal values for different types of cells (see other example cases below).

We then investigated the relationship between peak and duration in a given maintenance phase of the underlying oscillation by performing a regression analysis on the outputs for the entire range of G_{CaT} and G_{Kd} values. Figure 3C shows that peak and duration had an approximately linear inverse relationship when only G_{CaT} and G_{Kd} were permitted

to vary over the two-dimensional space, i.e., higher peaks resulted in shorter durations and vice versa ($R^2 = 0.89$). This relationship can be explained by noting that higher peaks provided more Ca^{2+} influx, which led to faster and stronger termination via I_{KCa} , as well as to faster inactivation of the depolarizing Ca^{2+} currents. This relationship allows for a prediction of the peak based solely on duration, or vice versa, assuming G_{KCa} to be fixed. This also shows how G_{CaT} and G_{Kd} can maintain the duration of the oscillation by controlling the level of depolarization, i.e., peak, for fixed values of G_{KCa} , supporting our counter-intuitive prediction that higher peaks result in shorter durations.

Termination of the underlying oscillation. Model experiments showed that I_{KCa} was the main current in controlling termination of the oscillation for the LC, due to its dependence on calcium for activation. Without I_{KCa} , the oscillation returned to the resting potential only after 603 ms, primarily due to the slow inactivation of I_{CaS} . Although the G_{CaT} - G_{Kd} module controlled both peak and duration as discussed in the previous section, G_{KCa} was found to modulate the duration of the oscillation with little effect on peak (Fig. 3D). Larger G_{KCa} promoted shortening of the duration, but with a saturation effect. Varying G_{KCa} from 0.5 to 5 times the nominal value resulted in the duration values changing from +16% to -24% of the nominal duration. Importantly, for any duration set by a fixed value of G_{KCa} , the G_{CaT} - G_{Kd} module could maintain that duration and peak if they co-varied in a particular proportion.

Although inter-burst interval is not considered in this study due to the fact that it depends additionally on synaptic inputs, it is noted that increasing G_{KCa} may increase the

refractory period, i.e., it may extend the time elapsed before another successful oscillation can be generated with the same input stimulus.

Conservation of generation, maintenance, and termination modules in other model bursting cells

After establishing the role of these ionic conductances in all phases of bursting output, we sought out, as cited, two other independent model neurons from the literature, the STG AB cell (Soto-Treviño et al. 2005) and the *Aplysia* R15 cell (Bower and Beeman 1998) to determine whether these findings from the LC model applied to other types of bursting cells that had the same currents.

Generation of the underlying oscillation. Our initial LC results indicated that G_B and G_A may form a module controlling the generation of the underlying oscillation. Further, we were able to establish boundary lines across conductance levels for G_B and G_A that governed the transition from silent cells to forced bursters to endogenous oscillators for the LC. Our results for AB and R15 were consistent with and extended these observations.

Example case 2, AB cell: For the AB cell, the nominal parameter values placed the endogenous burster in the upper region of the parameter space in Fig. 4A. A 5nA pulse for 10ms was used for generating the boundaries below the ‘nominal’ point (large filled circle) in the figure. The amplitude of this stimulus was sufficient to initiate the oscillation and the duration of the pulse was 5-10% of the oscillation duration, similar to example case 1. As shown in the figure, we were able to replicate the finding of these boundary lines for the AB cell. In addition, the boundaries were steepest for this example case. Increasing the

input stimulus also altered the lower boundary in AB; doubling the duration of the input stimulus lowered the boundary line by 14%, while doubling both duration and magnitude lowered it by 28%.

Example case 3, Aplysia R15 cell: For the R15 neuron, as expected, the parameter values also placed this endogenous burster in the upper endogenous region in the parameter space of Fig. 4A. Using the same logic as in example cases 1 and 2, a 40nA pulse for 250ms was used for generating the boundaries. The slopes of the boundaries were smallest in this case, indicating that a comparatively larger change in G_A was needed to counter an increase in G_B . Doubling the duration of the input stimulus lowered the lower boundary line by 21%, while doubling both duration and magnitude of the stimulus lowered it by 28%.

All three example cases had boundary lines with different slopes due to the differences in the maximal current conductances and kinetics for each of the models. Furthermore, individual adjustments to the other current conductances (G_{CaT} , G_{Kd} and G_{KCa}) did have some effect on the endogenous boundaries. At nominal conductance values for the other currents, increasing G_{KCa} to 5 times nominal value raised the endogenous boundary line by only 3.3% and 5% respectively, for example cases 1 (LC) and 2 (AB). In example case 3 (R15), increasing it to 5 times nominal value raised the endogenous boundary by 445%. Increasing only G_{CaT} to 5 times the nominal value shifted the endogenous boundaries down only by 23% and 9%, respectively, for LC and R15. For AB, an increase of G_{CaT} to 5 times the nominal value caused the cell to become endogenous even with G_{CaS} set to 0. Increasing only G_{Kd} to 5 times the nominal value shifted the endogenous boundaries up by 33% in LC, 289% in AB, and 9% in R15. Thus, while G_B

and G_A appear to form a module to conserve the generation of bursting, the unique output of a cell is, as always, a mix of the total ionic conductances present at any given time.

Maintenance of the underlying oscillation. Our initial LC analysis identified a relationship between G_{CaT} and G_{Kd} that maintained the peak and duration of the underlying oscillation. Our model experiments with the AB and R15 cells also yielded consistent findings.

Example case 2, AB cell: The nominal AB model produced an underlying membrane potential oscillation with a peak of -27 mV and duration of 151 ms. For comparison with biological ranges, in biological recordings from isolated AB neurons, the oscillation duration had a mean of approximately 170 ms with a SD of ~20 ms, and with the peak amplitude had a mean of ~9 mV and SD of ~0.7 mV (Bal et al. 1988). This represents a SD of 12% of the mean for duration. Figures 5A1 and 5A2 show plots of the % changes in peak and duration values, respectively, as G_{CaT} and G_{Kd} were varied from 0.5 to 5 times their nominal values (with all other G_i constant) for AB. These figures were generated in the same manner as Figures 3B1 and 3B2. Positive (negative) directional arrows indicated increasing (decreasing) peak heights and durations. Gray areas in Figs. 5A1 and 5A2 show cases where G_{Kd} was too large to allow normal endogenous oscillations. A 1:1 ratio of co-variation for G_{CaT} and G_{Kd} was found to result in a deviation of 65% in peak and 160% in duration with a 5x increase in nominal values for both conductances. In the nominal AB cell, equal increases in both G_{CaT} and G_{Kd} strengthened I_{Kd} disproportionately. We found that a 1:0.5 ratio for $G_{CaT}:G_{Kd}$ best preserved the features of the underlying oscillation for the model AB cell (see Table SM5 in supplementary material for numerical estimates).

Example case 3, Aplysia R15 cell: The nominal *Aplysia* R15 cell model had an underlying membrane potential oscillation with a peak of -38 mV and duration of 10.4 s. For comparison with biological ranges, in biological recordings from n=7 R15 neurons, the oscillation duration had a mean of approximately 8.5 s with a SD of ~1.875 s, and the peak amplitude had a mean of ~8.5 mV and SD of ~0.6 mV (Coyer 1986). This represents a SD of 22% of the mean for duration. Figures 5B1 and 5B2 show plots of the % changes in peak and duration values, respectively, as G_{CaT} and G_{Kd} were varied from 0.5 to 5 times their nominal values (with all other G_i constant). These figures were generated in the same manner as Figures 3B1 and 3B2, i.e., positive (negative) directional arrows indicated increasing (decreasing) peak heights and durations. A 1:1 variation was found to result in a change of 8% in peak and 92% in duration for a 5x increase from nominal values of both conductances. Again, careful analysis revealed that a ratio of 1:0.35 in covariations for $G_{CaT}:G_{Kd}$ best preserved the output features (see Table SM6 in the supplementary material for numerical estimates) for the model R15 cell.

As in the LC example, we performed regression analyses on height vs. duration for the entire range of G_{CaT} and G_{Kd} values, for AB and R15 model cells. For the *Aplysia* R15 cell, we removed values where G_{Kd} was too strong because this prevented action potentials and so affected the activation of G_{CaT} . Figure 4B shows that for AB and R15 cells, as with the LC, oscillation height and duration had an inverse relationship when only G_{CaT} and G_{Kd} were permitted to vary independently across the two-dimensional space, i.e., higher peaks resulted in shorter durations and vice versa. R^2 values were 0.71 and 0.87 respectively, for the AB and *Aplysia* R15 model cells.

Termination of the underlying oscillation. G_{KCa} was found to modulate the duration of the oscillation without affecting peak in AB and R15 cells, as it did in the case of the LC. Larger G_{KCa} promoted shortening of the duration, but with a saturation effect (Fig. 4C). Varying G_{KCa} from 0.5 to 5 times the nominal value resulted in the duration values changing from +7% to -13% and +62% to -21% of nominal duration values for the AB and R15 cells, respectively. As in the LC case, for any duration set by a fixed value of G_{KCa} , the G_{CaT} - G_{Kd} module could maintain that duration and peak if they co-varied in the right proportion.

DISCUSSION

Slow-wave bursting cells exhibit a characteristic underlying oscillation in their membrane potential. We investigated how maximal conductances of the active ionic currents might interact to preserve the peak and duration of such oscillations, for both forced and endogenous bursters. This led to the several findings related to the role of individual currents and current groups (modules) in shaping the characteristics of the phases of the oscillation. The LC and AB models are likely fold/homoclinic or ‘square wave’ bursters with the intracellular Ca^{2+} concentration as the slow resonant variable. Ca^{2+} builds up during the oscillation and the cell transitions back to resting through the Ca^{2+} gated activation of I_{KCa} and the Ca^{2+} gated inactivation of I_B . The time constant for I_B is not ‘slow’ for these two examples. However, for the R15 model the time constant of I_B is ten times higher than those of the fast currents and so I_B acts as an additional slow variable, leading to circle/circle or ‘parabolic’ bursting (Izhikevich 2007). Since the paper focuses

on insights from an electrophysiology perspective, these analytical issues have not been emphasized here.

Characteristics of the slow-wave underlying oscillation

Role of individual currents in shaping the underlying oscillation. Analysis of the effects of individual variations in maximal current conductances (e.g., Fig. 2, where the effects of varying individual current conductances are shown) showed that the peak and duration are not robust to changes in each conductance. However, co-regulation of certain current ‘module’ conductances was discovered to largely preserve the features of generation and to preserve its peak and duration. Based on an analysis of the individual currents during the slow wave underlying oscillation, and the effects of individual conductance variations as shown in Fig. 2, the role of the active currents involved in the underlying oscillation can be summarized as follows: I_A countered I_B during the generation of the oscillation, with I_{CaT} taking over for the majority of the faster depolarizing dynamics of the oscillation. Depolarization activated I_{Kd} which then countered I_{CaT} to control the peak of the oscillation. I_{CaT} and I_{Kd} had similar effects but with opposite signs. Ca^{2+} buildup within the cell strengthened I_{KCa} which terminated the oscillation by repolarizing the membrane potential. I_{Kd} decreased as the oscillation went down, while I_{KCa} increased and I_B inactivated. This implies that I_{KCa} contributed to termination (together with inactivation of I_{CaT} and I_B) of the oscillation. It is noted that because I_{Nap} may be involved in generation of the oscillation in some cells, it could be included in the term burst current I_B in such an analysis. *Individual current variations thus affect the dynamics of the underlying oscillation in different, yet somewhat related ways.*

Peak and duration of an underlying oscillation are strongly related. Counter to intuition, it was found that increasing the hyperpolarizing current I_{Kd} lengthened the duration of the oscillation. It was also found that increasing the depolarizing current I_{CaT} shortened the duration. Two reasons account for these phenomena. First, higher peaks occurred when the depolarizing current I_{CaT} was stronger. This caused greater activation of Ca^{2+} currents leading to a larger buildup of calcium. This buildup, along with a higher voltage, led to stronger and quicker activation of I_{KCa} , resulting in a faster termination of the oscillation. Second, higher peaks (voltages) also caused the depolarizing Ca^{2+} currents to inactivate earlier and cause quicker termination. On the other hand, increases in G_{Kd} caused lower peaks. Lower peaks caused less activation of the Ca^{2+} currents and less buildup of calcium, resulting in a later onset of the terminating I_{KCa} current, and slower inactivation of the depolarizing Ca^{2+} currents. Thus, counter to intuition, stronger I_{Kd} lengthened the duration of the oscillation and stronger I_{CaT} shortened it. Also, higher peaks were found to correspond to shorter durations, and vice versa.

Separate current modules control different phases of the underlying oscillation

An underlying oscillation of a slow-wave bursting cell can be divided into three phases: generation, maintenance of peak and duration, and termination. Opposing currents with similar activations seem to pair together to control these separate phases. I_B and I_A form the *generation module* since, when varied individually, they act in opposite ways to control the generation of the oscillation. It is noted that the other currents do have an effect on the boundary lines as quantified earlier, but a key observation is that for fixed values of

those currents, I_B and I_A could always be co-varied to control generation of the underlying oscillation.

Similarly, I_{CaT} and I_{Kd} form the *maintenance module*, i.e., they can be appropriately co-varied to preserve the peak and duration of the oscillation. These currents have faster dynamics and higher voltage activations, providing them with finer control for shaping the peak and duration of the oscillation, with I_{CaT} promoting higher peaks and shorter durations, and I_{Kd} doing the opposite. Again, the other currents did affect peak and duration values, but with those fixed, co-variation of only I_{CaT} and I_{Kd} was found to preserve peak and duration of the oscillation.

I_{KCa} was found to act as a *termination module* due to its calcium-dependent activation. The activation of I_{KCa} occurred only after calcium build-up during the depolarized phase of the oscillation. Hence, it became active only during the termination phase and had little effect on the early dynamics. Although I_{KCa} did affect the duration of the maintenance module to a limited extent, it had little effect on peak. It is not considered a part of the maintenance ‘module’ since it cannot be co-varied with either G_{CaT} or G_{Kd} to maintain both duration *and* peak height, has a saturation effect in its limited ability to shorten the duration, and alters other properties such as after-hyperpolarization (AHP). Moreover, as cited, it was found that for any fixed G_{KCa} , G_{CaT} and G_{Kd} can be co-varied appropriately to maintain the peak and duration of that oscillation, indicating that G_{KCa} plays only a secondary role during the maintenance phase. In summary, I_{KCa} can be viewed as semi-independent of the other modules with its primary role being termination of the oscillation.

Once the correlations were determined in the LC model for the baseline case, we questioned whether the correlations were general and held throughout the conductance space. As cited earlier, in addition to investigating whether the correlations were preserved for randomly selected points in the parameter space, we devised a different strategy to test their validity. We considered example cases 2 and 3, the AB cell and the R15 cell, both of which had the same set of conductances.

To investigate whether the correlations would hold at other locations in the parameter space for the LC model, we considered several widely-separated points in the maximal conductance space. For the G_{CaS} - G_A generation boundary, four points were considered: (1x G_{CaT} , 1x G_{Kd} , 1x G_{KCa}), (5x G_{CaT} , 1x G_{Kd} , 1x G_{KCa}), (1x G_{CaT} , 5x G_{Kd} , 1x G_{KCa}), and (5x G_{CaT} , 5x G_{Kd} , 1x G_{KCa}). Here G_i represents the nominal value of the conductance i . The correlation did hold at each point and also the boundary did not deviate by more than 33% for any of these tested points. This boundary was also found to deviate very little for maximal changes in G_{KCa} , less than 4% difference for 5x G_{KCa} . Since the boundary was found to exist for maximal changes in each of the conductances, as well as in the maximal two-dimensional space of G_{CaT} and G_{Kd} , without drastic changes to the boundaries for any of these conditions, we feel that the G_{CaS} - G_A module will hold for any set of G_{CaT} , G_{Kd} , and G_{KCa} .

Further, the coregulation of G_{CaT} with G_{Kd} to preserve the duration and peak was also found to hold for variations in the other three parameters. Three random points from the parameter space were selected: (1.25x G_{CaS} , 1x G_A , 1x G_{CaT} , 0.8x G_{Kd} , 1.5x G_{KCa}), (1.75x G_{CaS} , 2x G_A , 1x G_{CaT} , 0.75x G_{Kd} , 0.5x G_{KCa}), (2.5x G_{CaS} , 3.5x G_A , 1.6x G_{CaT} , 2.5x G_{Kd} , 5x G_{KCa}). Our finding is that a ratio between G_{CaT} and G_{Kd} , albeit different for different

sets of parameters, can be found that preserves the duration and peak of the underlying oscillations. For all three random points in the parameter space, we were able to find appropriate ratios that preserved the characteristics. Since the insight is also based on the similarities of the current kinetics (shapes of the activation/inactivation curves and time constants), we believe it is general enough and should hold for other points in the conductance space.

The current I_{KCa} does not activate until the end of the oscillation after enough calcium has accumulated inside the cell. For each of the points chosen, we consistently found that I_{KCa} shortened the duration without any significant effect on the peak of the underlying oscillation. So, random sampling of points in the multi-dimensional space for the LC model indicates that the G_{CaS} - G_A generation boundary is present for other points in the $(G_{Kd}, G_{CaT}, G_{KCa})$ space, and that it is possible to find a ratio of G_{Kd} to G_{CaT} for other points in the (G_{CaS}, G_A, G_{KCa}) space that preserves duration and peak of the oscillations. The generation boundaries and the G_{Kd} to G_{CaT} ratios themselves do vary depending on the other parameters, but they have been shown to exist for all points where the cell is not silent. As cited, the kinetics of the activation and inactivation curves for the currents involved also support the existence of these correlations. These correlations were then found to hold for example cases 2 and 3 also. *Thus, we conclude that distinct currents or modules of currents largely control the different phases of the underlying oscillation for such slow wave bursters, with G_B and G_A controlling generation, G_{CaT} and G_{Kd} controlling maintenance of peak and duration, and G_{KCa} primarily controlling termination.*

The G_B - G_A parameter sub-space has characteristic ‘functional’ boundary lines

Model experiments revealed that the G_B - G_A parameter subspace was divided into three separate functional regions, by two characteristic boundaries: an upper region where the parameter values led to an endogenous oscillation, a middle region where forced oscillations occurred such that the cell was silent (i.e. does not produce an underlying oscillation) until an appropriate input stimulus caused an oscillation, and a lower region where the cell did not produce an oscillation irrespective of the stimulus strength. Changes in the other conductances (G_{CaT} , G_{Kd} , and G_{KCa}) had an effect, albeit minor, on either the location or the overall shape of the characteristic boundaries. The leak current may appear to play a role similar to that of the burst current in the generation module, in some cases. However, we feel that it should not be grouped with I_A in the generation module for several reasons. Firstly, I_{leak} switches between being an inward or outward current due to its reversal potential being close to the ‘rest’ for both AB and R15 cells, whereas I_A is always an outward current. Thus, in the AB and R15 models, I_{leak} assists I_B with depolarization during the early part of the ‘rest’ phase but then assists I_A in hyperpolarizing the cell prior to the upswing of the membrane potential. Kuznetsova et al (2010) report that in dopaminergic neurons, A-type potassium currents can increase the firing frequency of pacemaking neurons, if the conductance is reduced. We find a similar result for all three model cases in that the inter burst interval decreases as G_A is reduced. However, reducing G_{leak} actually prolongs the amount of time until the initiation of an oscillation in the AB and R15 models, playing an exactly opposite role. Secondly, I_{leak} is not an active current. For that reason, I_{leak} can only increase linearly with membrane potential changes. I_{leak} is thus not capable of countering the rapidly increasing nonlinear activation of I_B during the

generation phase. However, I_A also has a nonlinear activation curve that increases rapidly around ‘rest’, making it an ideal candidate to counter I_B . To prevent a forced oscillation by an input current injection in the LC, it was found that the % increase in I_{leak} had to be 2.3 times that of the % increase in G_A . To prevent endogenous oscillation in the other models, it was found that the % increase in I_{leak} had to be ten times that of the % increase in G_A for the AB model (1.25 times for the R15 cell), showing that I_A correlates much more strongly with I_B , compared to I_{leak} . Thirdly, I_{leak} is persistent and so affects other phases of the oscillation more compared to the rapidly inactivating I_A . This means that increases to G_A will alter primarily the generation module, but increases to G_{leak} can affect the entire course of the oscillation, including the AHP.

We thus find that the mechanism delineating endogenous oscillating, forced bursting, and non-bursting is most directly attributable to the relative contributions of G_B and G_A . Furthermore, these conductances can co-vary to maintain generation of the underlying oscillation, a feature that may explain similar variability in conductances reported in recent studies (Ball et al. 2010).

G_{Kd} and G_{CaT} can co-regulate to maintain peak and duration

For slow-wave bursting cells with the active currents cited, a proportional ratio could always be found for G_{CaT} and G_{Kd} such that the peak and duration of the underlying oscillation were preserved by co-regulating the two conductances in that ratio. For example case 1 (LC), a $G_{CaT}:G_{Kd}$ ratio of 1:1.1 best preserved the peak and duration values, indicating that the strength of I_{CaT} was comparable to that of I_{Kd} . Remarkably, this ratio is consistent with the relationship in mRNA copy number for two channels that may

contribute to this relationship, *cacophony* and *shab* (Tobin et al. 2009). However, the precise relationship between mRNA copy number and conductance is unknown for these channels. For example cases 2 and 3 (AB cell and the *Aplysia* R15 cell), I_{Kd} was stronger compared to I_{CaT} when each conductance was varied in the similar proportion from its nominal value. So, a near 1:1 co-regulation did not preserve the peak and duration in this case, with positive changes resulting in lower peaks and longer durations. However, co-regulation in $G_{CaT}:G_{Kd}$ in ratios of 1:0.5 and 1:0.35 respectively, for the AB cell and *Aplysia* R15 cell, ensured that the peak and duration were preserved. These results are consistent with those reported for channel mRNA; different cell types of the STG often have similar correlations among channel mRNA levels that differ in the slope of their relationship (Schulz et al. 2007). *Therefore, even with different activation curves and conductances for the currents in the three example cases, co-regulation of G_{CaT} and G_{Kd} can preserve the peak height and duration of the underlying oscillation in all the cases.*

CONCLUSIONS

If compensatory mechanisms exist to stabilize or regenerate the output of neurons, then a balance must be struck between stabilizing mechanisms and those that initiate processes of plasticity for recovery of output. Evidence of stabilizing mechanisms has been documented at multiple levels. For example, STG neurons collected from intact networks with ongoing activity show distinct correlations at the level of both ion channel expression (Schulz et al. 2007) and membrane conductance (Khorkova and Golowasch 2007). Furthermore, when an STG cell with intact ongoing activity is challenged with an over-expression of a hyperpolarizing conductance (G_A), it is able to maintain its output by

a complementary upregulation of a depolarizing conductance G_H (MacLean et al. 2003, 2005). Thus, evidence for co-regulation of conductances to stabilize or maintain output exists to justify this line of thought. However, when the output of a cell is changed dramatically, there appear to be plasticity mechanisms that override these stabilizing forces to recover rhythmic activity. For example, when an STG neuron is isolated in cell culture, it undergoes a series of changes in firing pattern ranging from tonic spiking to silent before recovery of bursting is obtained (Turrigiano et al. 1995; Haedo and Golowasch 2006). These mechanisms include an increase in inward currents such as calcium currents and a decrease in outward potassium currents (Turrigiano et al. 1995; Haedo and Golowasch 2006). In a modeling study of the functional recovery of STG neurons, a full account of the regulation was found in the case of correlated or anticorrelated changes of the maximal conductances of the calcium and potassium currents (Olypher and Prinz 2010). Thus, these two classes of maintenance of output, stabilization and recovery, may represent changes in the relationship among currents from co-variation to independent or inverse regulation.

Our study identifies potentially conserved ‘modules’ involved in different phases of output conservation. In addition, we identify boundaries amongst these relationships that divide the output of these cells into endogenous oscillating, forced bursting, and silent (not producing underlying oscillations). These modules allow for targeted hypothesis generation for examining potential regulatory mechanisms. For example, if a cell loses its ability to generate bursting, this may represent disruption in the relationship of G_B and G_A . In this case, as with the cultured STG neurons, the cells seem to shift into the “silent” phase of the generation module boundary. One possible mechanism towards recovery of bursting activity could be an uncoupling of compensatory co-regulation of the generation module,

so that the cell can once again cross boundaries (by upregulating G_B and/or downregulating G_A) and re-enter the oscillating zone (see Fig. 3A1 for example boundary regions).

Limitations. The present study has some limitations that should be noted. First, preservation of the underlying oscillation in a biological cell may not simply entail balancing maximal conductances, but may also result from post-translational mechanisms modifying channel kinetics. While compensatory changes that stabilize neuronal output in the absence of changes in channel kinetics have been demonstrated in *Drosophila* neurons (Peng and Wu 2007), homeostatic regulation may occur at multiple levels of processing. Second, our model assumes co-localization for all conductances known to generate the underlying oscillation. However, little is known about functional compartmentalization of channel types in these cells. The study considers a class of bursters with six active currents, and future studies could explore co-regulation features in other types of bursting cells. Also, the reported models and analyses can be extended to include post-translational and other relevant mechanisms as they become better understood biologically, and can then be used to study their effect on preserving output function.

REFERENCES

- Bal T, Nagy F, Moulins M. The pyloric central pattern generator in crustacea: A set of conditional neuronal oscillators. *J Comp Physiol* 163: 715-727, 1988.
- Ball JM, Franklin CC, Schulz DJ, Nair SS. Co-regulation of ion channel conductances preserves output in a computational model of a crustacean cardiac motor neuron. *J Neurosci* (in press)
- Berlind A. Spontaneous and repetitive driver potentials in crab cardiac ganglion neurons. *J Comp Physiol* 149: 263-276, 1982.
- Bower JM, Beeman D. *The book of GENESIS: exploring realistic neural models with the GEneral NEural SIMulation System*. New York: Springer-Verlag, 1998.
- Buchholtz F, Golowasch J, Epstein R, Marder E. Mathematical model of an identified stomatogastric ganglion neuron. *J Neurophysiol* 67: 332-340, 1992.
- Cooke IM. Reliable, responsive pacemaking and pattern generation with minimal cell numbers: the crustacean cardiac ganglion, *portunus sanguinolentus*. *Bio Bull* 202: 108-136, 2002.
- Coombes S, Bressloff P. *Bursting: The Genesis of Rhythm in the Nervous System*. Singapore: World Scientific Press, 2005.
- Coyer PE. An analysis of the bursting behaviour of the Aplysia R15 neurone during exposure to normoxia and hypoxia with and without external calcium present. *Comp Biochem Physiol A Comp Physiol* 85(1): 121-7, 1986.
- Golowasch J, Buchholtz F, Epstein R, Marder E. Contribution of individual ionic currents to activity of a model stomatogastric ganglion neuron. *J Neurophysiol* 67: 341-349, 1992.
- Grillner S, Wallen P, Hill R, Cangiano L, El Manira A. Ion channels of importance for the locomotor pattern generation in the lamprey brainstem-spinal cord. *J Physiol* 33: 23-30, 2001.
- Haedo RJ, Golowasch J. Ionic mechanism underlying recovery of rhythmic activity in adult isolated neurons. *J Neurophysiol* 96(4): 1860-1876, 2006.
- Harris-Warrick RM. Voltage-sensitive ion channels in rhythmic motor systems. *Current Opinions Neurobiol* 12: 646-651, 2002.
- Ivanov AI, Calabrese RL. Intracellular Ca²⁺ dynamics during spontaneous and evoked activity of leech heart interneurons: Low-threshold Ca²⁺ currents and graded synaptic transmission. *J Neurosci* 20(13): 4930-4943, 2000.

- Izhikevich E. Simple model of spiking neurons. *IEEE Trans Neural Networks* 14: 1569-1572, 2003.
- Izhikevich E. *Dynamical systems in neuroscience - the geometry of excitability and bursting*. Cambridge, MA: The MIT Press, 2007.
- Khorkova O, Golowasch J. Neuromodulators, not activity, control coordinated expression of ionic currents. *J Neurosci* 27(32): 8709-8718, 2007.
- MacLean JN, Zhang Y, Johnson BR, Harris-Warrick RM. Activity-independent homeostasis in rhythmically active neurons. *Neuron* 37: 109-120, 2003.
- MacLean JN, Zhang Y, Goeritz ML, Casey R, Oliva R, Guckenheimer J, Harris-Warrick RM. Activity-independent coregulation of IA and Ih in rhythmically active neurons. *J Neurophysiol* 94: 3601-3617, 2005.
- Olypher AV, Prinz AA. Geometry and dynamics of activity-dependent homeostatic regulation in neurons. *J Comput Neurosci* (February 9, 2010). doi: 10.1007/s10827-010-0213-z.
- Peng IF, Wu CF. Drosophila cacophony channels: A major mediator of neuronal Ca²⁺ currents and a trigger for K⁺ channel homeostatic regulation. *J Neurosci* 27: 1072-1081, 2007.
- Prinz A, Billimoria CP, Marder E. Alternative to hand-tuning conductance-based models: Construction and analysis of databases of model neurons. *J Neurophysiol* 90: 3998-4015, 2003.
- Prinz A, Bucher D, Marder E. Similar network activity from disparate circuit parameters. *Nat Neurosci* 7: 1345-1352, 2004.
- Schulz DJ, Goaillard JM, Marder E. Variable channel expression in identified single and electrically coupled neurons in different animals. *Nat Neurosci* 9: 356-362, 2006.
- Schulz DJ, Goaillard JM, Marder E. Quantitative expression profiling of identified neurons reveals cell-specific constraints on highly variable levels of gene expression. *Proc Nat Acad Sci* 104: 13187-13191, 2007.
- Soto-Treviño C, Rabbah P, Marder P, Nadim F. Computational model of electrically coupled, intrinsically distinct pacemaker neurons. *J Neurophysiol* 94: 590-604, 2005.
- Swensen AM, Bean BP. Robustness of burst firing in dissociated purkinje neurons with acute or long-term reductions in sodium conductance. *J Neurosci* 25: 3509-3520, 2005.
- Tazaki K, Cooke IM. Spontaneous electrical activity and interaction of large and small cells in cardiac ganglion of the crab, *portunus sanguinolentus*. *J Neurophysiol* 42: 975-999, 1979a.

Tazaki K, Cooke IM. Isolation and characterization of slow, depolarizing responses of cardiac ganglion neurons in the crab, *portunus sanguinolentus*. *J Neurophysiol* 42: 1000-1021, 1979b.

Tazaki K, Cooke IM. Ionic bases of slow, depolarizing responses of cardiac ganglion neurons in the crab, *portunus sanguinolentus*. *J Neurophysiol* 42: 1022-1046, 1979c.

Tazaki K, Cooke IM. Separation of neuronal sites of driver potential and impulse generation by ligaturing in the cardiac ganglion of the lobster, *homarus americanus*. *J Comp Physiol* 151: 329-346, 1983b.

Tazaki K, Cooke IM. Currents under voltage clamp of burst-forming neurons of the cardiac ganglion of the lobster, *homarus americanus*. *J Neurophysiol* 56: 1739-1762, 1986.

Tazaki K, Cooke IM. Characterization of Ca current underlying burst formation in lobster cardiac ganglion motoneurons. *J Neurophysiol* 63: 370-384, 1990.

Tobin AE, Cruz-Bermúdez ND, Marder E, Schulz DJ. Correlations in ion channel mRNA in rhythmically active neurons. *PLoS One* 4(8): e6742, 2009.

Turrigiano G, LeMasson G, Marder E. Selective regulation of current densities underlies spontaneous changes in the activity of cultured neurons. *J Neurosci* 15: 3640-3652, 1995.

Table 1. Biophysical details of example case 1 (cardiac ganglion LC)

1A: Model parameters.

Current Parameters				
	Soma		Axon	
	G_{max} (mS/cm ²)	E_{rev} (mV)	G_{max}	E_{rev} (mV)
I_{Na}	--	--	600	50
I_{Kd}	190	-73	200	-73
I_A	90.25	-73	--	--
I_{KCa}	40	-73	--	--
I_B	6.83	Nernst	--	--
I_{CaT}	2.4	Nernst	--	--
I_{Leak}	0.04	-55	0.04	-55
Other Parameters				
Surface Area	8.88 x 10 ⁻³ cm ²		0.98 x 10 ⁻³ cm ²	
Capacitance	2.35 μF/cm ²		2.13 μF/cm ²	
Base $[Ca^{2+}]_{in}$	0.5 μM		--	
$\tau_{Ca^{2+}}$	640 ms		--	
$F_{Ca^{2+}}$	0.256 μM/nA		--	
R_{axial}	1.5 MΩ		--	

1B: Gating functions for these currents.

I_{ion}	x^p	x_∞ (V in mV, [Ca] in μ M)	τ_x ms, (V in mV)
I_{Na}	m^3	$\frac{1}{1 + \exp\left(\frac{V + 25.5}{-5.29}\right)}$	$2.64 - \frac{2.52}{1 + \exp\left(\frac{V + 120}{-25}\right)}$
	h	$\frac{1}{1 + \exp\left(\frac{V + 48.9}{5.18}\right)}$	$\frac{1.34}{1 + \exp\left(\frac{V + 62.9}{-10}\right)} \times \left(1.5 + \frac{1}{1 + \exp\left(\frac{V + 34.9}{3.6}\right)}\right)$
I_B	m^3	$\frac{1}{1 + \exp\left(\frac{V + 35}{-7.2}\right)}$	$2.8 + \frac{14}{\exp\left(\frac{V + 27}{10}\right) + \exp\left(\frac{V + 70}{-13}\right)}$
	h_1	$\frac{1}{1 + \exp\left(\frac{V + 62}{6.2}\right)}$	$120 + \frac{300}{\exp\left(\frac{V + 55}{9}\right) + \exp\left(\frac{V + 65}{-16}\right)}$
	h_2	$\frac{13}{13 + [Ca]}$	640
I_{CaT}	m^3	$\frac{1}{1 + \exp\left(\frac{V + 27.1}{-7.2}\right)}$	$43.4 - \frac{42.6}{1 + \exp\left(\frac{V + 68.1}{-20.5}\right)}$
	h	$\frac{1}{1 + \exp\left(\frac{V + 32.1}{5.5}\right)}$	$210 - \frac{179.6}{1 + \exp\left(\frac{V + 55}{-16.9}\right)}$
I_A	m^3	$\frac{1}{1 + \exp\left(\frac{V + 29.2}{-7.8}\right)}$	$23.2 - \frac{20.8}{1 + \exp\left(\frac{V + 32.9}{-15.2}\right)}$
	h	$\frac{1}{1 + \exp\left(\frac{V + 56.9}{4.9}\right)}$	$77.2 - \frac{58.4}{1 + \exp\left(\frac{V + 38.9}{-26.5}\right)}$
I_{Kd}	m^4	$\frac{1}{1 + \exp\left(\frac{V + 18.3}{-9.8}\right)}$	$14.4 - \frac{12.8}{1 + \exp\left(\frac{V + 28.3}{-19.2}\right)}$
I_{KCa}	m^4	$\frac{[Ca]}{[Ca] + 3} \times \frac{1}{1 + \exp\left(\frac{V + 28.3}{-12.6}\right)}$	$180.6 - \frac{150.2}{1 + \exp\left(\frac{V + 46}{-22.7}\right)}$

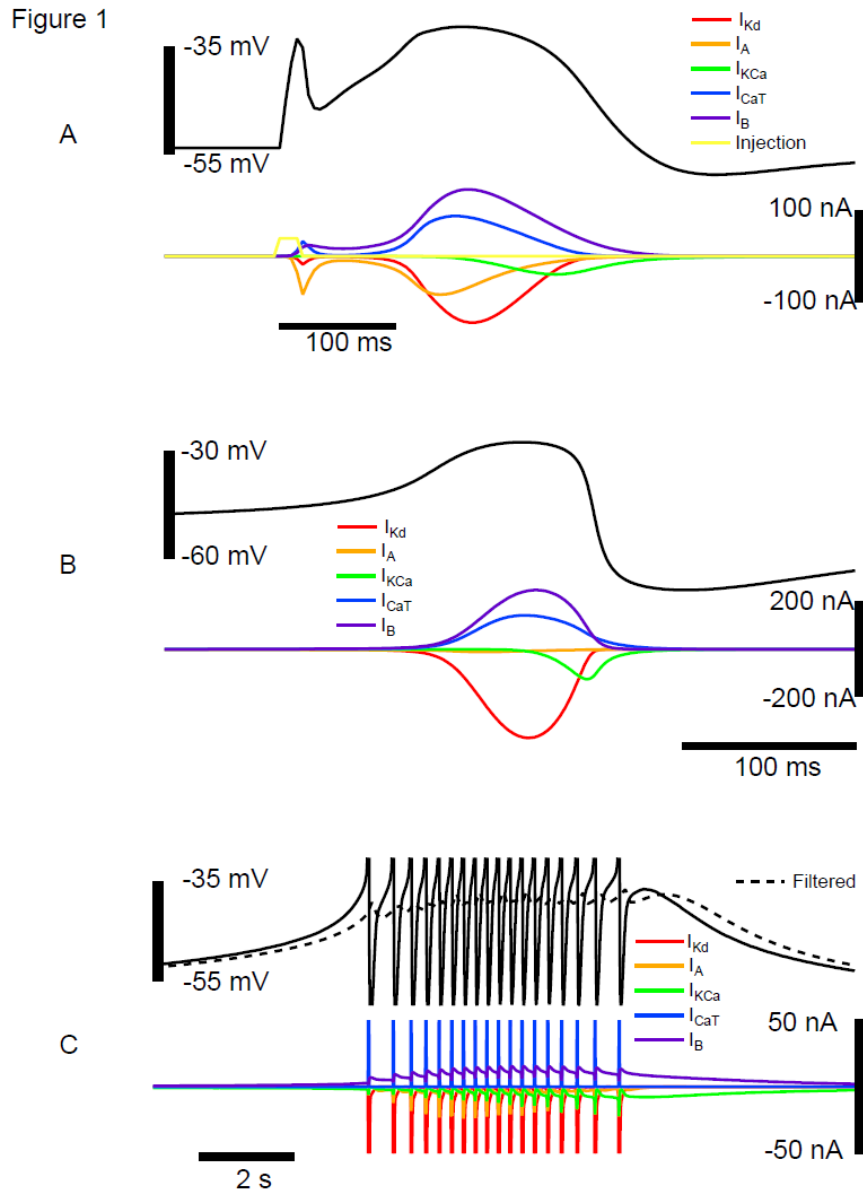


FIG. 1. The underlying membrane potential oscillations and corresponding currents for the three example cases: A. Large Cell (LC) of the crustacean cardiac ganglion, B. Anterior Burster (AB) cell of the crustacean stomatogastric ganglion, C. R15 cell of the *Aplysia* abdominal ganglion. The voltage trace has been cut off at -30 mV for the *Aplysia* R15 cell to magnify the underlying oscillation. The current trace has also been cut off at -50 nA and 50 nA for the *Aplysia* R15 cell to magnify the slow currents.

Figure 2

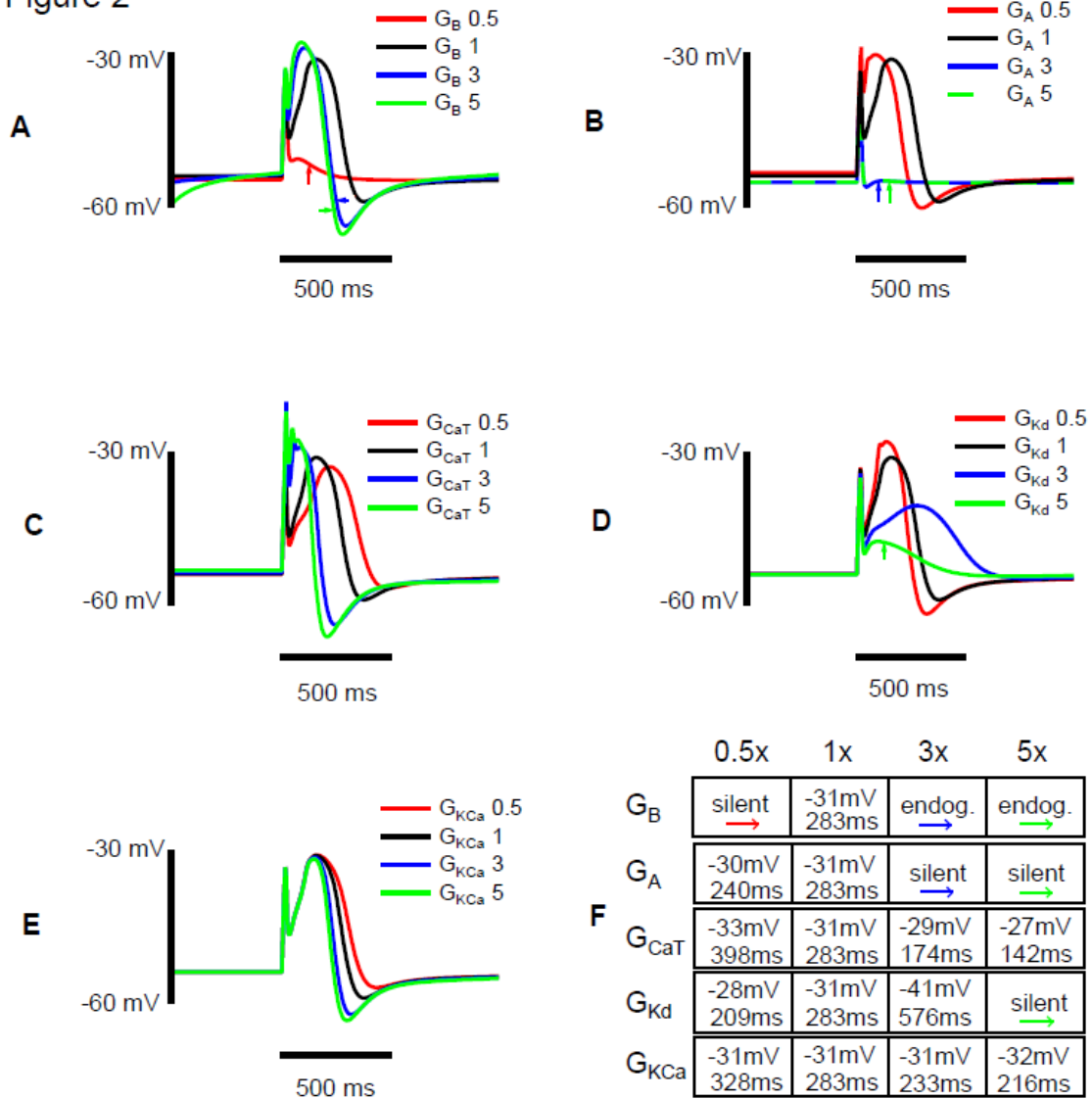


FIG. 2. The underlying membrane potential oscillations resulting from variations in conductance of each of the individual currents in the LC. Values shown are 0.5x, 1x, 3x, and 5x of the nominal conductance values. A. G_B , red arrow denotes silent behavior for 0.5x case, blue and green arrows denote endogenous oscillatory behavior for 3x and 5x cases. B. G_A , blue and green arrows denote silent behavior for 3x and 5x cases. C. G_{CaT} D. G_{Kd} , green arrow denotes silent behavior for the 5x case. E. G_{KCa} . F. Peak and duration values for individual conductance variations shown in plots A-E.

Figure 3

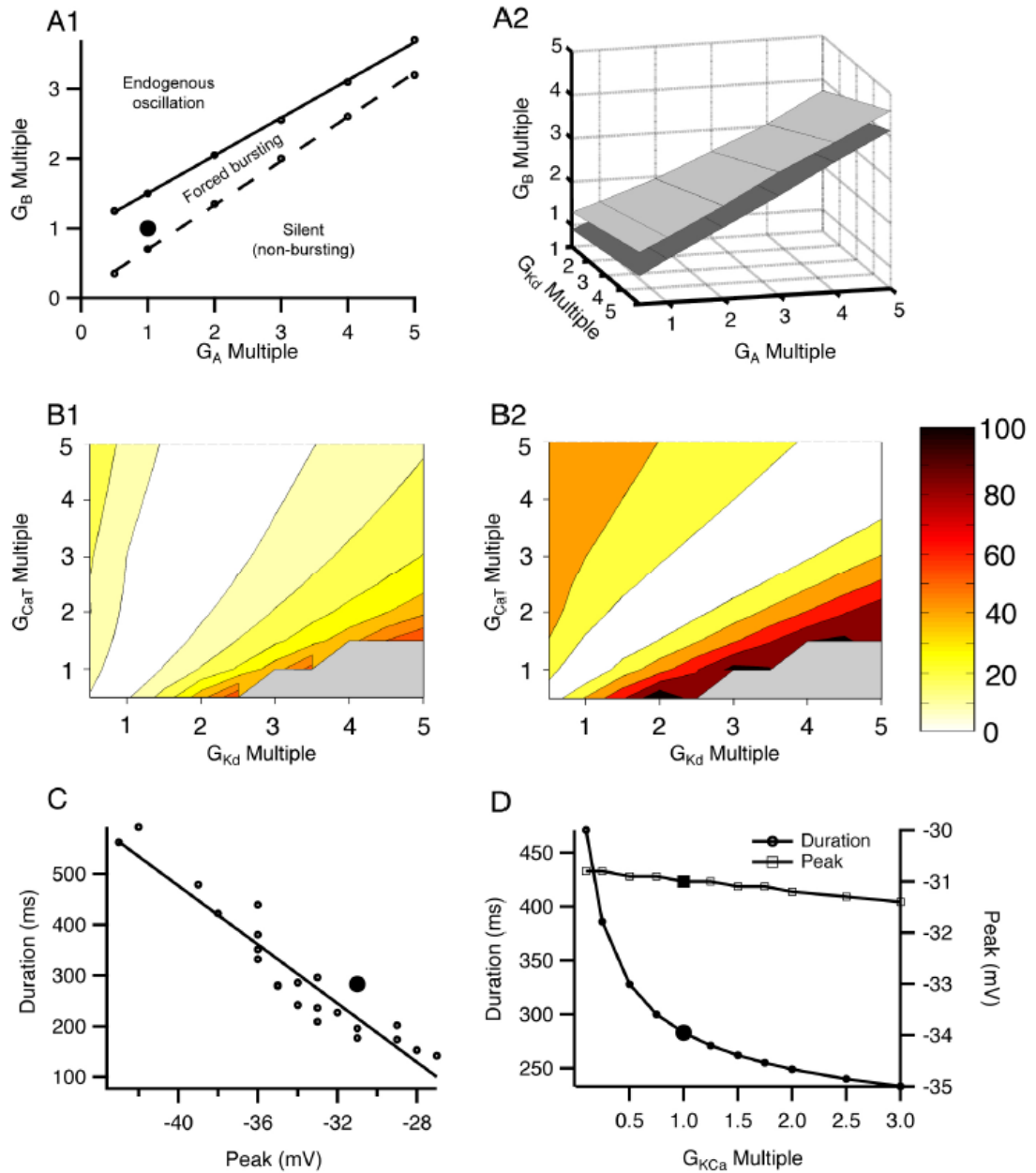


FIG. 3. Relationships among conductances in the proposed modules for the LC.

A1. Characteristic G_B - G_A boundaries. Upper boundary (solid line) represents the transition from endogenous oscillation to forced bursting, and lower boundary (dashed line) is the transition from forced burster to silent cell (i.e., does not produce an underlying oscillation). X-axis is the conductance multiplier for variation from the nominal values of

G_A , and Y-axis is the conductance multiplier for variation from nominal values of G_B . Nominal model values are at 1,1 of the x-y axes.

A2. Co-variation of G_B - G_A preserves the shape of the upper boundary of Fig. 3A1 even with variations in G_{Kd} (3rd axis) and G_{CaT} (top surface is 1x nominal G_{CaT} , while the lower surface is 5x nominal G_{CaT} value; G_{KCa} is 1x for both surfaces).

B. Change in peak (B1) and duration (B2) of the underlying oscillation, with variations in G_{CaT} and G_{Kd} from 0.5 to 5 times the nominal value (other G_i at nominal values). Percentage change from nominal values of peak and duration are indicated by the color map. Grey areas in the figure indicate conductance pairs that did not produce a proper underlying oscillation. Positive (negative) directional arrows indicated increasing (decreasing) peak heights and durations.

C. The peak of the underlying oscillation varied inversely with duration when G_{CaT} and G_{Kd} were varied individually across a 0.5x to 5x range of their nominal (in bold) values.

D. Relationship of duration and peak as G_{KCa} is varied, with all other G_i held at nominal (in bold) values.

Figure 4

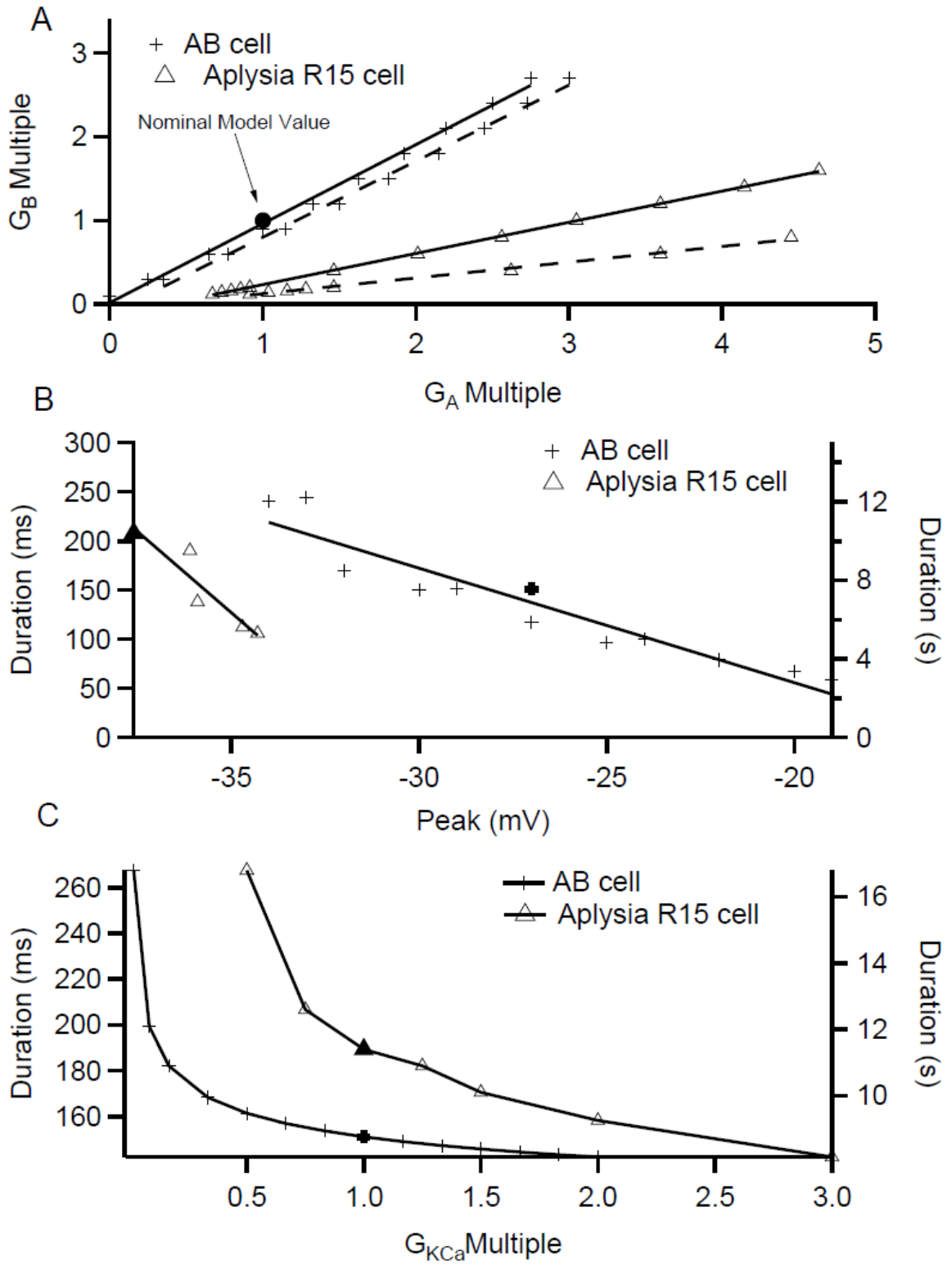


FIG. 4. Relationships among conductances in the proposed current modules for the AB cell and *Aplysia* R15 cell also follow the same pattern as found for the LC.

A. Characteristic G_B - G_A boundaries. Upper boundary (solid line) represents the transition from endogenous oscillation to forced bursting, and lower boundary (dashed line) is the transition from a forced burster to a silent cell (i.e., does not produce an underlying oscillation). X-axis is the conductance multiplier for variation from the nominal values of G_A , Y-axis is the conductance multiplier for variation from nominal values of G_B . Nominal model values are at location (1,1).

B. As in Figure 3C, the peak of the underlying oscillation varied inversely with duration when G_{CaT} and G_{Kd} were varied individually across a 0.5x to 5x range of their nominal (in bold) values, for the AB and *Aplysia* R15 example cells also.

C. The variation of duration with G_{KCa} , with all other G_i held at nominal (in bold) values, followed a similar pattern to that for the LC (Fig. 3D).

Figure 5

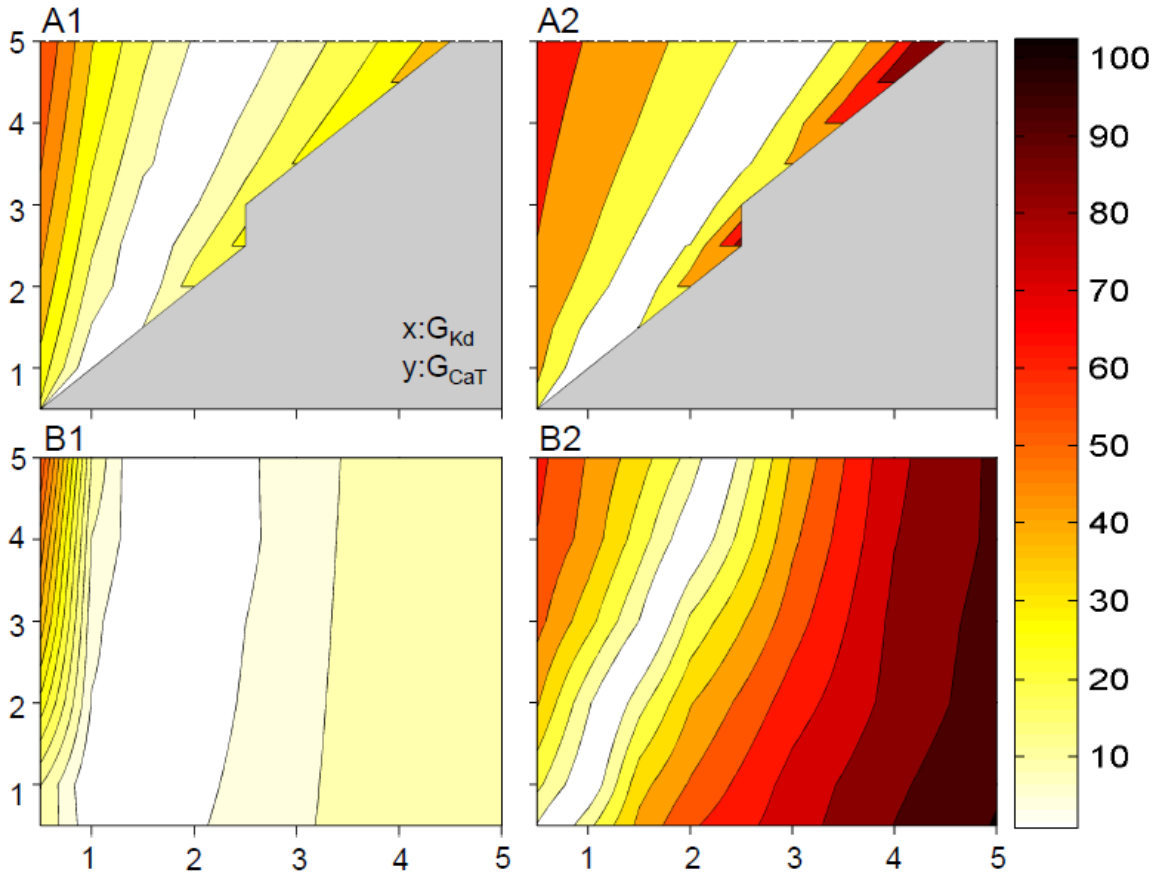


FIG. 5. The changes in peak and duration of the underlying oscillation in AB and *Aplysia* R15, with variations in G_{CaT} and G_{Kd} from 0.5 to 5 times their nominal value (other G_i at nominal values), followed a similar pattern to that found in the LC. Percentage change from nominal values of peak and duration are indicated by the color map. Positive (negative) directional arrows indicated increasing (decreasing) peak heights and durations. Grey areas in the figure indicate conductance pairs that did not produce a proper underlying oscillation: A1. AB cell Peak; A2. AB cell Duration; B1. *Aplysia* R15 cell Peak; B2. *Aplysia* R15 cell Duration.

CHAPTER 3

CELLULAR AND SYNAPTIC CORRELATES OF PATTERN FORMATION IN A HIPPOCAMPAL MODEL

ABSTRACT

The hippocampus processes contextual information that likely involves both place awareness and episodic memory. We studied the underlying mechanisms in hippocampal memory formation by adapting a computational network model of the rodent hippocampus to incorporate biologically realistic conductance-based cells in CA3 and dentate gyrus (DG) regions. Single cell biophysical models were developed for principal cells and for the two abundant interneuron types in CA3, basket cells (BCs) and oriens lacunosum-moleculare (OLM) interneurons. The network model included synaptic current dynamics, spatial connectivity patterns, short-term synaptic plasticity, and known effects of acetylcholine. The model was then used to investigate the cellular and synaptic correlates of pattern formation in CA3 when a specific pattern was projected from the entorhinal cortex (EC). Multiple analyses suggested that inhibition was the most significant factor influencing the recruitment of a CA3 cell into a pattern. The normalized relative importance of the afferents in influencing this recruitment was as follows: 1 for inhibition, 0.65 for EC, 0.49 for DG, and 0.07 for the CA3 recurrent collaterals. Furthermore, differential connectivity and inhibitory dynamics between BCs and OLM cells was found to enable the former to control the recruitment of specific pyramidal cells into the CA3 pattern, and the latter to regulate pattern size. Analysis also revealed the participation of a disynaptic inhibitory mechanism in this recruitment. Finally, biological realism in both connectivity and cell types suggested that back-projections from CA3 to DG both stabilized

patterns in CA3, and helped increase pattern storage capacity in CA3 by 16%. This first fully biologically-based network model of the hippocampus also provides a test-bed for studying phenomena such as genesis of oscillations that are thought to require models with high fidelity.

INTRODUCTION

The hippocampus has long been implicated in memory storage and retrieval. Through the process of memory retrieval, termed “pattern completion”, the CA3 region of the hippocampus aids in the retrieval of previously learned memory traces even from partial cues or noisy inputs (Marr 1971). In contrast, the dentate gyrus (DG) functions to separate neural representations of similar memories, via a different circuit, to optimize their storage and later retrieval (Marr 1971); for review, see Hunsaker and Kesner 2013). Computational models of pattern separation and completion in the hippocampus have provided an important conceptual framework to study the underlying mechanisms (Hasselmo et al. 1995; Treves and Rolls 1992) and several of their predictions have been validated experimentally (Leutgeb et al. 2007; Neunuebel and Knierim 2014; Rolls and Kesner 2006). The differential roles for CA3 and DG have inspired a formulation that divides the major synaptic pathways in this circuit as either biasing the circuit towards pattern completion or separation. For example, the input from the entorhinal cortex (EC) to CA3 has been theorized to provide sufficient plasticity to store patterns and allow their later retrieval (pattern completion), while the connections from DG to CA3 have been theorized to transmit separated representation of memory patterns to CA3. More recently, there has also been interest in the role of the previously neglected back-projections from CA3 to DG

(Myers and Scharfman 2011). This projection has been theorized to enhance the ability of the network to perform pattern separation, but has not been fully characterized (Myers and Scharfman 2011).

Locally in CA3, the recurrent excitatory connections have been associated with memory retrieval or pattern completion, with many computational studies employing recurrent local connectivity to store patterns of neuronal activity. Inhibitory pathways, however, have not been as well examined. Previous modeling studies used generic forms of inhibition, and only a few explicitly modeled interneurons (Cutsuridis et al. 2010; Kunec et al. 2005) and these did not study their specific roles. Nonetheless, hippocampal interneurons display substantial heterogeneity in terms of their connectivity patterns and temporal dynamics, and likely contribute differentially to memory formation.

While there seems to be consensus about the interactions between the various hippocampal regions at the population level, the relative contribution of the excitatory and inhibitory mechanisms to the dynamics during pattern formation remains unclear. Moreover, the interplay of multiple cell types in a distributed circuit makes it difficult to unravel the roles of such interactions in experiments. A computational model knows no such limitations. We developed a biologically realistic network model of the CA3 and DG regions of the rodent hippocampus that included pyramidal neurons (PNs) and two interneuron types. The model was developed by matching biological data including neuronal firing patterns, synaptic dynamics, short-term synaptic plasticity, neuromodulatory effects, and the three-dimensional organization of the regions. Dissection of the neural pathways of the network replicated findings from previous theoretical models on the role of major hippocampal pathways in pattern completion and separation. The

present model provided several new insights into the hippocampal mechanisms during pattern formation in CA3, including the contributions of specific excitatory and inhibitory connections. Inhibition was found to be the most important factor in determining which CA3 PN was recruited into a pattern. Furthermore, the model suggested differential roles for BCs and OLM cells in pattern formation, with BCs being more closely involved in recruiting a particular CA3 PN into a CA3 pattern (i.e., cell assembly selection) and OLMs in stabilizing the general network activity. Finally, we found support for the hypothesis that back-projections from CA3 to the dentate gyrus enhance pattern separation (Myers and Scharfman 2011), and also quantified the corresponding increase in storage capacity in CA3.

METHODS

We developed a network model of the rodent hippocampus in a prior study using Izhikevich single cell models, synaptic currents, spatial connectivity patterns, short- and long-term plasticity and known neuromodulator effects (Hummos et al. 2014). The model included CA3 and DG regions that received inputs from EC. The present study used the same model, except for replacing the Izhikevich single cell models with biophysical conductance-based models matched to biological data. We provide information related to the single cell models followed by an overview of the network model and key features. The reader is referred to our previous study for details, including a complete listing of other parameters (Hummos et al. 2014). The model, developed using the package NEURON (Carnevale and Hines 2006), will be made available upon publication via the public database ModelDB (<http://senselab.med.yale.edu/ModelDB/>).

Single cell models

Single neurons were modeled using the Hodgkin-Huxley formulation (Byrne et al. 2014) and included multiple compartments with known currents and neuromodulator receptors. CA3 model cells included PNs and the two most abundant interneuron types, BCs and OLM cells (Vida 2010). DG model cells included granule cells, BCs, and Hilar Perforant Path-associated (HIPPA) cells. All model neurons were matched to the salient features reported in biology. CA3 PNs fire in bursts of 2-3 action potentials as well as individual spikes (Tropp Sneider et al. 2006). These PNs respond to current injections with an initial burst followed by either silence or tonic firing at different frequencies (Brown and Randall 2009; Hemond et al. 2008) and are also capable of bursting in response to a very short (2-5 ms) current pulse with a burst of action potentials that out-live the stimulus (Brown and Randall 2009; Wong and Prince 1981). Model CA3 PNs had a resting potential of -75 mV, input resistance of 80 M Ω and time constant of 21 ms. Parvalbumin-positive basket cells (BCs) are characterized by fast spiking patterns and a small membrane time constant (~10 ms) and little spike frequency adaptation (Bartos and Elgueta 2012). The cell model had these characteristics, with a resting potential of -64 mV and firing rate vs. current injection relationship that matched data in Buhl et al. (1996). OLM cells have a high input resistance (496 M Ω) and slow membrane time constant (71 ms) (Lawrence et al. 2006). Action potentials are followed by a characteristic long-lasting, slow after-hyperpolarization with rebound spikes occurring commonly on repolarization. Model OLM cells captured these characteristics, and had a resting membrane potential of -68 mV (Ali and Thomson 1998). OLM model cells were also tuned to produce the observed slow AHP, rebound spikes and the characteristic sag with negative current injections. Granule cells in DG

display a very low basal firing rate in vivo with an average < 0.5 Hz, and bursts shorter than those in CA3 cells (Jung and McNaughton 1993). These cells predominantly fire in single spikes with spike frequency adaptation (Staley et al. 1992). DG model cells had resting membrane potential of -73 mV (Staley et al. 1992) and matched biological data including passive properties and responses to current injections (Staley et al. 1992). Interneurons in DG used the same BC model and used the OLM model for HIPP cells (Katona et al. 1999). A complete listing of the parameters for the four single cell models described above can be found in Appendix tables 1A-1C.

Network structure and connectivity

Typical of network models of brain regions, the network model was a scaled down version of the numbers of neurons in the rat hippocampus (Hummos et al. 2014; Li et al. 2011). The CA3 region contained 63 pyramidal cells, and 8 BCs and 8 OLM cells, while the DG region had 384 granule cells, 32 BCs and 32 HIPP cells (Fig. 1A). The number of cells in each region was selected keeping the ratio between population cell numbers as close to biology as possible.

Model cells in CA3, DG and EC were distributed in three dimensions, corresponding to the rat hippocampal morphology. Perforant path projections from EC follow a lamellar organization across a longitudinal axis of the hippocampus (Naber et al. 1997; Witter 2010), and projections from DG to CA3 follow a similar longitudinal organization (Hummos et al. 2014). Projections from EC to pyramidal cells and BCs in DG and CA3 were most likely to project to neurons in the center of their longitudinal neighborhood, using a Gaussian connection probability function that depended on the

longitudinal distance between cells. The Gaussian function had a peak probability value of 0.4 for projections from EC to pyramidal cells and BCs in CA3. EC projections to DG had similar values. Mossy fiber projections from DG to CA3 followed a similar lamellar pattern as of EC to CA3 and EC to DG projections. Each DG granule cell connected to a maximum of two CA3 pyramidal neurons (Rolls and Kesner 2006), in order to create sparse MF connections. Previous studies have determined that projections from DG granule cells to CA3 BCs outnumber projections to CA3 pyramidal neurons by a ratio of 10:1 (Acsády et al. 1998). Accordingly, DG projections to BCs followed a Gaussian distribution with a higher peak probability and standard deviation than projections from DG to CA3 PNs. Recurrent connections between CA3 PNs were generated with a fixed probability of 0.3, since these recurrents generally reveal limited spatial organization (Wittner et al. 2007).

OLM cells make many more synapses compared to BCs (Fig 1B; Sik et al. 1995), but have limited axonal arborization, and are believed to participate in feedback inhibitory loops (Maccaferri 2005). BCs have a more diffuse axonal arborization with higher likelihoods of connecting to pyramidal cells in the vicinity of the BCs (Sik et al. 1995). BCs also provide inhibitory connections to neighboring OLM cells (Bartos et al. 2010), but OLM cells do not project to BC cells. Again, Gaussian functions were used for connection probabilities (Fig. 1B). BC projections to PNs and to OLM cells shared the same spatial domain, while OLMs received reciprocal connections from the PNs they projected to (Maccaferri 2005). PNs in both DG and CA3 projected to BCs with a fixed probability of 0.15, based on the lack of specific topography for these projections (Wittner et al. 2007). CA3 back-projections inhibit DG granule cells through a direct pathway (Ishizuka et al. 1990; Li et al. 1994; Scharfman 1994) and indirectly by exciting hilar mossy cells

(Scharfman 2007; 1994) and also DG interneurons with dendrites in the hilus (Kneisler and Dingledine 1995; Scharfman 1994).

Connections between cells were generated randomly, based on the probabilities described in Hummos et al. (2014), and background input was used to match spontaneous firing rates of PNs and interneurons in CA3 (Mizuseki et al. 2012) and in DG (Bower and Buckmaster 2008).

Synaptic currents

The synaptic AMPA, NMDA, GABA_A, and GABA_B currents were modeled based on (Destexhe et al. 1998) and their dynamics were matched to available literature. AMPA currents in CA3 PNs were fastest for inputs from DG and slowest for inputs from EC, while inputs from other CA3 cells had intermediate values (Hoskison et al. 2004; Tóth 2010). Additionally, BC inhibitory currents had faster dynamics than those from OLM (Bartos et al. 2010). Synaptic weights were assigned based on available literature. The synapses from DG to CA3 were selected so multiple inputs to a CA3 cell would cause the CA3 cell to spike, while a single synaptic input would not (Henze et al. 2002). Recurrent CA3 synapses used a low initial synaptic weight, based on biological data indicating low transmission probability of action potentials (4%) at the recurrent CA3 synapses (Miles and Wong 1983). CA3 pyramidal cell to BC and OLM interneurons used a higher synaptic level based on biological data indicating a higher transmission probability of action potentials (~60%) (Gulyas et al. 1993; Miles 1990). In the DG region, synapses between DG granule cells and DG interneurons were selected to provide sparse DG firing (Bower and Buckmaster 2008).

Long-term synaptic plasticity

Biological studies have shown classical Hebbian associative long-term potentiation (LTP) at the glutamatergic perforant path synapses to DG (Bliss and Gardner-Medwin 1973) and to CA3 (Do et al. 2002). Many types of synaptic plasticity exist at GABAergic synapses (for a review, see Maffei (2011)). Woodin et al. (2003) reported LTP between hippocampal cells if the pre- and post-synaptic spikes were within 20ms of each other, LTD if within 50ms, and no change if longer. They also found plasticity to be dependent on activation of postsynaptic L-type voltage dependent calcium channels (VDCCs).

Consistent with these findings, the model implemented LTP using a learning rule based on the concentration of a post-synaptic calcium pool at each modifiable synapse (Shouval et al. 2002a). At excitatory synapses, calcium entered post-synaptic pools via NMDA receptors, and at inhibitory synapses, calcium entered through VDCCs. The postsynaptic pool also received Ca^{2+} from internal stores upon GABA_B receptor stimulation. This approach has been used in other models by our group (Kim et al. 2013b; Li et al. 2009). For both types of synapses, a calcium concentration above a lower threshold caused synaptic weight depression, while a concentration exceeding an upper threshold cause synaptic weight potentiation. Because the characteristics of DG to CA3 mossy fiber potentiation are controversial (Neves et al. 2008), we only modeled short-term plasticity in the MF connections, as described below. Long-term plasticity in all synapses was constrained to 100%.

Short-term synaptic plasticity

In addition to long-term plasticity described above, we included short-term plasticity in the model based on the formulation by (Varela et al. 1997). We modeled short-term facilitation reported at the DG to CA3 mossy fiber connections (Toth et al. 2000) and frequency-dependent synaptic depression reported at the recurrent CA3 connections (Hoskison et al. 2004). In CA1, projections from pyramidal cells to OLM cells have been shown to experience short-term facilitation (Ali and Thomson 1998), while projections to BC cells experience short-term depression (Ali et al. 1998). In the opposite direction, inhibitory currents from OLM cells to CA3 pyramidal cells show no short-term facilitation or depression (Maccaferri 2005), while inhibitory currents from BC cells to CA3 pyramidal cells show depression (Hefft and Jonas 2005).

Acetylcholine effects

The hippocampus receives cholinergic inputs from the septum-diagonal band complex (Woolf 1991). To implement the effects of ACh in our model on cells and synaptic connections, a variable 'ACh' was used to represent discrete ACh levels of 0 (low), 1 (baseline), and 2 (high). Under cholinergic stimulation, synaptic transmission from EC to CA3 is suppressed by 50%, and is suppressed by 85% at the recurrent connections in CA3 (Barry et al. 2012; Hasselmo et al. 1995; Kremin and Hasselmo 2007). In contrast, DG to CA3 synaptic transmission is enhanced by 49% under cholinergic stimulation (Vogt and Regehr 2001). We did not modify inhibitory synaptic connections in the model based on ACh levels. AMPA synaptic currents were scaled by the value of ACh in our model to represent ACh effects on the synapses. A parameter bACh was used to determine the

direction and magnitude of ACh effects on a particular synapse. Values of bACh for different synapses were set according to experimental results. In addition to the synaptic effects described above, cholinergic stimulation also enhanced cellular excitability, depolarized the resting membrane potential of principal cells, eliminated AHP, decreased spike frequency adaptation and induced rhythmic burst activity (Bianchi and Wong 1994; Misgeld et al. 1989). Effects on BC and OLM interneurons were subtype-dependent (McQuiston and Madison 1999a; b). Muscarinic stimulation of OLM interneurons depolarized the resting membrane potential, and also lowered spike frequency adaptation and AHP (Lawrence et al. 2006). In contrast, BC cells have low levels of nicotinic ACh receptors, and they respond to muscarinic receptor activation with a limited resting membrane potential depolarization (Cea-del Rio et al. 2010; Cobb and Lawrence 2010). We modeled effects of ACh on neurons by linearly scaling cell parameters by the ACh level (see Hummos et al. 2014).

Other model features

Random Poisson inputs were provided to principal cells in CA3 and DG to generate the biological spontaneous firing rates reported *in vivo*: CA3 – 0.49 Hz model, 0.50 Hz biology (Mizuseki et al. 2012); DG - 2.90 Hz model, 2-4 Hz biology (Santhakumar et al. 2005). For inhibitory interneurons: 2 Hz model, 1.9 Hz biology (Seegerstrale, 2010). As also noted in Hummos et al. (2014), 10 EC inputs were found to be optimal for our specific network size, in the sense that any more caused run-away excitation in CA3 (Fig. 1C). The training protocol had five 500-ms trials, involving repeated presentation of pattern 1 from EC (Fig. 1D). For this, pattern 1 was presented for the first 250 ms of a trial at a theta rate

of 12 Hz, with no input for the next 250 ms of the trial. After such a training, a neuron was considered ‘active’ during the presentation of a pattern if its average firing rate was significantly higher than the spontaneous value using a z-score cut-off of 2.58. We used the same parameters as in Hummos et al. (2014) and so did not perform any de novo tuning at all. The only modifications made were to the following parameters: initial connection weights from CA3 to BCs and to OLM cells were 1.5; from DG granule cells to interneurons in the DG region were 1.5; and from EC to DG granule cells were 1.5. Also, the calcium threshold for depression at EC to CA3 pyramidal cell synapses was 0.2 and the upper calcium threshold for potentiation was 0.4. All the other parameters and the tuning process including during encoding (high ACh) and retrieval (low ACh) were exactly the same as in Hummos et al. (2014).

In each retrieval trial, the number of spikes for each CA3 and DG PN in response to each of the eleven different patterns presented at EC was recorded (Fig. 1D; Hummos et al. 2014). Subsequently, for each EC input pattern, a trial “output” pattern was formed in each region (CA3 and DG) by combining the spike counts from all of the region’s principal cells into a vector that was then normalized to a length of one. The correlation between the output patterns of any two EC input pattern retrieval trials was then determined by performing a dot product of the two corresponding output pattern vectors. A correlation value of 0 indicated that the two output patterns being compared had non-overlapping sets of spiking neurons. Conversely, a correlation value of 1 indicates that the two vectors had the same set of neurons firing at the same rates.

For each region in the model (CA3 and DG), we calculated correlations between the output from EC input pattern 1 and the output from each of the EC input patterns from

1 to 11. Figure 1E illustrates these correlation values for EC, CA3 and DG regions. Because inputs arrived directly at EC neurons, EC correlation levels are identical to the similarity between input patterns. CA3 output patterns had a higher correlation than EC correlation (Fig. 1E), indicating that CA3 was engaged in retrieval of stored patterns. For instance, EC input pattern 3 had a correlation of 0.8 with EC input pattern 1, compared to a CA3 output pattern correlation of 0.95 between pattern 1 and pattern 3. This indicates that even for dissimilar EC inputs, CA3 retrieved output patterns that are more similar to the learned pattern 1. Therefore, even when sensory input patterns change, CA3 may still retrieve a previously learned memory pattern. On the other hand, DG output patterns exhibited lower correlation relative to the EC input patterns, indicating that DG was biased towards creating new neuronal representations (Fig. 1E). These results are consistent with computational theories of the roles of DG and CA3 in pattern completion and separation (Kremin and Hasselmo 2007; McClelland and Goddard 1996; O'Reilly and McClelland 1994; Treves and Rolls 1992) and recent experimental evidence (Bakker et al. 2008; Lee and Kesner 2004; Leutgeb et al. 2007; Neunuebel and Knierim 2014).

As cited earlier, we developed the model using the modeling software NEURON, and ran the model on a desktop with an integration time-step of 0.1 ms (Carnevale and Hines 2006). We then analyzed recorded spike times using MATLAB (Mathworks, Inc.). As mentioned above, cell model membrane potential values, network connectivity and initial synaptic weights were selected from random distributions. Accordingly, for each experiment, five instantiations of the network with different random initializations were considered. Numbers reported in results are averages \pm SD over data pooled from five different runs.

RESULTS

We developed a biophysical network model of the rodent hippocampus using the same structure and parameters as in our previous model (Hummos et al. 2014), but with all the Izhikevich single cell models in CA3 and DG regions replaced by more realistic biophysical models. The revised model reproduced the pattern separation/completion characteristic and the findings of the prior model. The model was then used to investigate the hitherto unexplored underlying interactions among the excitatory and inhibitory connections in CA3 and DG during pattern formation. To do this, we classified individual cells using z-scores, and systematically investigated the training-induced effects of specific synaptic pathways on pattern storage in CA3.

To provide context to the findings reported below, we briefly describe the functioning of the overall model. The network included models for the CA3 and DG regions, with EC providing inputs to both regions; the model also included cholinergic modulation (Hasselmo et al. 1995; Hummos et al. 2014). At high levels of ACh, DG granule cells increased their firing rate through a more depolarized membrane potential, lower spike frequency adaptation, and lower AHP. Aided by prominent short-term facilitation at MF synapses, high ACh levels enhanced the flow of information from DG to CA3. Concurrently, the high cholinergic state also suppressed synaptic transmission from EC to CA3, and at the recurrent synapses in CA3, minimizing any interference produced by similarity to any previously stored patterns. At the same time, connections from DG to CA3 BCs further increased the level of inhibition on CA3 pyramidal cells, minimizing retrieval. As a result, high ACh levels facilitated formation of distinct representations of input patterns in CA3. In contrast, the following effects enabled low ACh levels to enhance

retrieval of stored patterns in CA3: reduced firing rate of DG granule cells, and increased transmission in EC-CA3 and CA3-CA3 synapses, all of which have also been shown in previous models (Barkai et al. 1994; Hasselmo et al. 1995; Hasselmo and Wyble 1997). Although these processes are understood at the larger regional level, the relative roles of the underlying mechanisms within CA3 and DG are unclear and have not been quantified.

The reader is reminded that the network model of Hummos et al. (2014) that we used after adding biologically realistic cells had connectivity between the EC, CA3, and DG regions that was more realistic than previous reported models (Fig. 1A). Consistent with previous studies (Hummos et al. 2014; Myers and Scharfman 2011), the training protocol lasted five 500-ms trials, involving repeated presentation of pattern 1. For this, the EC inputs (representing pattern 1) were presented for the first 250 ms of a trial at a theta rate of 12 Hz, with no input for the next 250 ms of the trial (see methods). To study the synaptic and cellular correlates of pattern formation, we first determined the underlying mechanisms that made certain CA3 PNs ‘active’ (based on z-scores; see methods) and others ‘inactive’. As cited, the cells that were ‘active’ formed the CA3 ‘pattern’. We then examined the numbers of intrinsic and extrinsic connections received by these two categories, i.e., active and inactive CA3 PNs. All results below used a large dataset with cells pooled from all five instantiations of the network. This pooled dataset indicated that a typical CA3 cell received the following numbers of afferents: 1.9 ± 1.0 from EC cells, 16.2 ± 3.7 from other CA3* cells, 7.4 ± 3.5 from DG* cells, 3.1 ± 1.0 from BCs and 2.8 ± 0.8 from OLM cells. A typical BC cell received the following numbers of afferents (CA3* and DG* indicate PNs that received at least one active EC input, as described further below): 1.7 ± 1.3 from EC cells, 2.2 ± 1.4 from CA3* cells, and 19.1 ± 6.0 from DG* cells. A typical

OLM cell received the following numbers of afferents: 18.9 ± 3.2 from CA3* cells and 4.0 ± 1.4 from BCs. The initial synaptic weights for these connections were drawn from uniform distributions with maximum values as follows: EC-CA3 of 1.5, CA3-CA3 of 0.3, DG-CA3 of 0.15, DG-BC of 0.75, BC-CA3 of 2.25, and OLM-CA3 of 2.25.

Inhibition and EC inputs are dominant in CA3 pattern selection

We investigated the roles of the following CA3 afferents in recruiting a CA3 PN into the pattern, i.e., making it ‘active’ (during training; high ACh levels): from EC, from within CA3 (CA3 principal cells and two inhibitory interneurons, BCs and OLM cells), and from DG regions. To ensure that the pattern in CA3 had stabilized after five trials, we performed a separate experiment where we continued training the network for 20 trials, instead of just five. This resulted in the pattern size in CA3 decreasing by 19% from trial 5 to trial 20. The weights of all the connections did not change significantly indicating that training for five trials provided a stable learned state in the system for analysis purposes.

We used two approaches to investigate the role of individual afferents in making a particular CA3 PN active. In the first approach, we compared active vs. inactive CA3* PNs based on the numbers and types of its afferents, i.e., an analysis of differences in afferents. We note that a cell is considered active if its average firing rate during the presentation of pattern 1 from EC was higher than its spontaneous rate using a z-score cut-off of 2.58 (see methods). In the second approach, we used correlation and regression analyses to examine how the firing rate of a CA3 PN varied as a function of the types and numbers of its afferents.

Active vs. inactive CA3 PNs and afferent connectivity

A key initial finding was that, for all five random instantiations of the network, all CA3 PNs that were part of the stored pattern in CA3 received inputs from EC. This suggests that competition among PNs to get recruited into a stored pattern (memory) occurs only among PNs that receive active input from EC. These PNs are hereafter termed CA3* PNs. Similar to CA3, all DG PNs that were included into the DG pattern received input from EC, and these PNs are termed DG* PNs. Considering the CA3 region, the primary focus of this study, the afferents that these PNs receive are as follows: excitatory afferents from EC, CA3* and DG* PNs; and inhibitory ones from BC and OLM interneurons.

A total of 36% (99/272) of CA3* cells were found to be active after the training protocol described above; considering all CA3 cells, the percentage was 31% (99/315). An analysis of connections showed that EC afferents were significantly higher for active vs. inactive CA3* PNs (active 2.4 ± 1.0 v/s inactive 1.6 ± 0.8 ; $p < 0.001$), and that DG* afferents were significantly higher for active vs. inactive CA3* PNs (active 8.9 ± 2.9 v/s inactive 6.6 ± 3.5 ; $p < 0.001$). However, excitatory connections from CA3* PNs to other CA3* PNs did not differ significantly between the groups (active 16.3 ± 3.8 v/s inactive 16.0 ± 3.5 ; $p < 1$). Also, inhibitory connections (BC and OLM combined) did not differ significantly between the groups (active 5.7 ± 1.4 v/s inactive 6.0 ± 1.4 ; $p < 0.5$). In summary, an aggregate level analysis showed that CA3* PNs in a stored CA3 pattern received significantly higher inputs from both EC and DG* PNs, compared to other CA3* PNs. After training with pattern 1, it was seen that 100% (20/20) of CA3* cells that received four connections from active EC cells were active, regardless of the other excitatory (CA3* or DG*) or inhibitory (BC or OLM) afferents. However, a similar trend was not seen for excitatory inputs from DG*.

This indicates that strong connectivity from EC can make a CA3 cell active irrespective of other afferent types and numbers. To study the contributions from the other afferents, we differentiated CA3* cells into groups that received 3, 2 or 1 EC input and analyzed their afferents separately.

CA3 cells receiving 3 EC inputs:* Of the CA3* cells that received three connections from active EC cells, 62% (31/50) were active after training. The 38% (19/50) that were inactive received significantly more inhibitory connections from BCs and OLM cells combined (active 5.5 ± 1.5 v/s inactive 6.7 ± 1.3 ; $p < 0.01$), and significantly less excitatory inputs from DG* cells (active 8.9 ± 2.7 v/s inactive $7.2 \pm .6$; $p < 0.05$). The difference between the groups for excitatory connections from CA3* cells was not significant (inactive 15.5 ± 3.9 v/s active 15.6 ± 3.2 ; $p < 1$).

CA3 cells receiving 2 EC inputs:* Of the CA3* cells that received two connections from active EC cells, 37% (30/81) were active after training. The 63% (51/81) that were inactive received significantly less excitatory inputs from DG* cells (active 9.3 ± 3.1 v/s inactive 7.4 ± 4.0 ; $p < 0.05$). The difference between the groups for excitatory inputs from CA3* cells was not significant (active 16.1 ± 4.0 v/s inactive 15.9 ± 3.4 ; $p < 1$), and the difference between the groups for inhibitory connections from BCs and OLM cells combined was not significant (active 5.9 ± 1.4 v/s inactive 6.1 ± 1.4 ; $p < 1$).

CA3 cells receiving 1 EC input:* Of the CA3* cells that received one connection from active EC cells, 15% (18/121) were active after training. The 85% (103/121) that were inactive received significantly less excitatory connections from DG* cells (active 8.2 ± 2.7 v/s inactive 6.0 ± 3.0 ; $p < 0.01$). The difference between the groups for excitatory inputs from CA3* cells was not significant (active 16.7 ± 3.4 v/s inactive 16.6 ± 4.0 ; $p < 1$), and the

difference between the groups for inhibitory connections from BCs and OLM cells combined was not significant (active 5.2 ± 1.5 v/s inactive 5.6 ± 1.4 ; $p < 0.5$).

The connections analysis suggested input from EC as an important afferent in making a CA3 PN active. Separating the cells based on the numbers of EC inputs received showed that the numbers of afferents from DG* cells and from inhibitory interneurons (BCs and OLM cells combined) were significantly different between active and inactive CA3* PNs for at least some EC input levels, but their relative importance was unclear. Next, we discuss two additional analyses to compare the relative influence of these three afferents on activity of CA3* PNs.

Firing rates of CA3* PNs and afferent connectivity

We performed two additional analyses to shed further light on the relative roles of the various afferents in recruiting a PN into the pattern in CA3.

Correlation analysis. Across all CA3* cells ($n=272$), average firing frequency of a CA3* PN was significantly correlated with the number of active EC input afferents ($p < 0.001$), the number of DG* afferents ($p < 0.001$), and the number of inhibitory afferents from BCs and OLM cells combined ($p < 0.01$). However, the number of CA3* recurrent excitatory connections by CA3* cells was not significantly correlated with CA3* firing frequency ($p < 1$). Interestingly, CA3* recurrent synapses did not show any significant trends when grouped by EC input levels similar to the analysis in the previous section, but the others did.

Regression analysis. A regression analysis was performed to determine the relative importance of the afferents of a CA3 PN. This yielded the following equation: CA3* cell

firing frequency = $2.14 + 1.86 * (\# \text{ of active EC inputs}) + 0.02 * (\# \text{ of CA3* cell excitatory connections}) + 0.36 * (\# \text{ of DG* cell excitatory connections}) - 0.92 * (\# \text{ of combined monosynaptic inhibitory connections from BC cells and OLM cells})$. All coefficients were statistically significant ($p < 0.001$) with the exception of CA3* excitatory connections ($p < 1$). When the coefficients were multiplied by their respective average connection numbers and normalized to the most significant connection (inhibition), the resulting relative importance of each afferent was as follows: Inhibition (by BCs and OLM cells combined): 1; EC: 0.65; DG: 0.49; CA3: 0.07.

These two additional analyses suggest that inhibition via BCs and OLM cells is the most important afferent in making a CA3 PN active, followed by excitation from EC. Furthermore, excitation from DG* cells was the third, with excitation from CA3* cells being a remote fourth. It is noted that this is not inconsistent with the fact that the EC afferent is very important as stated earlier, since EC directly contributes to inhibition via projections to BCs.

Role of Plasticity: The average growth in the different synapse types was as follows: EC-CA3* of 33%; EC-BC of 26%; CA3*-CA3* of 48%, CA3*-BC of -1%; CA3*-OLM of 18%; DG-CA3* of 0% (no plasticity); DG-BC of 0% (no plasticity); BC-CA3* of 6%; OLM-CA3* of -6%. As expected, the EC-CA3 synapses and CA3-CA3 synapses had the largest average growth among the synapse types, indicating that the EC-CA3 connections and CA3-CA3 connections play the primary role in storing the pattern during training. Interestingly, except for the CA3*-OLM connections, there was little change in synaptic strengths to and from interneurons within CA3. Excitation from EC makes BCs more active

compared to OLMs during encoding (Fig. 2; and Fig. 3A), and is an important reason for their differential involvement. This also suggests that these BCs may also effectively inhibit some local CA3 PNs that might receive fewer or no EC inputs. On the other hand, OLMs may provide general inhibition to prevent runaway excitation. Also, the larger potentiation of CA3-OLM synapses compared to CA3-BC synapses suggests that disynaptic inhibition from CA3* PNs to other CA3* PNs comes primarily from OLM cells. However, greater potentiation of EC-BC synapses compared to CA3-BC synapses suggests that disynaptic inhibition (discussed below) onto other CA3* PNs via BCs comes primarily from EC.

Role of neuromodulation. Most of the preceding analyses were for the encoding phase, with high ACh. For completion, we also studied the cellular and synaptic correlates during the ‘retrieval’ phase, with low ACh. Compared to the high ACh state, the CA3 pattern size increased by 51% at low ACh. Analysis to determine the relative importance of the afferents during low ACh provided the following regression equation: CA3* cell firing frequency = $3.24 + 8.68 * (\# \text{ of active EC inputs}) + 0.21 * (\# \text{ of CA3* cell excitatory connections}) + 0.04 * (\# \text{ of DG* cell excitatory connections}) - 1.93 * (\# \text{ of combined monosynaptic inhibitory connections from BC cells and OLM cells})$. All coefficients were statistically significant ($p < 0.01$) with the exception of DG* connections ($p < 1$). When the coefficients are multiplied by their respective average connection numbers and normalized to the most significant connection (EC, in this case), the resulting relative importance of each CA3 afferent in making a CA3* PN active, during the retrieval phase, was as follows: EC: 1; Combined BC and OLM: 0.69; DG: 0.02; CA3: 0.21. Several interesting findings

were revealed by this analysis as compared to the results in the high ACh state. First, in the low ACh state, DG* connections were no longer significantly correlated with CA3* firing frequency ($p < 1$ low ACh vs. $p < 0.001$ high ACh), and had a significantly reduced importance relative to the other connections types (0.02 low ACh vs. 0.49 high ACh). Second, CA3* recurrent connections became significantly correlated with CA3* firing frequency ($p < 0.01$ low ACh vs. $p < 1$ high ACh), and had an increased relative importance (0.21 low ACh vs. 0.07 high ACh). Third, EC inputs had increased relative importance (1.0 low ACh vs. 0.65 high ACh), while inhibition (BCs and OLM cells combined) had reduced relative importance (0.69 low ACh vs. 1.0 high ACh). Although these trends are perhaps expected, the benefit of such analyses is that they help provide important insights by quantifying the relative importance of the interactions.

To summarize, we performed two levels of analyses in this section to determine the importance of afferents in making a CA3 cell active. The first was at an aggregate level considering all CA3 PNs and analyzing whether differences in afferent connectivity would help classify PNs as active or inactive based on z-scores. However, connectivity considers neither afferent activity nor the connection weight. To incorporate both of these factors, at a second level, we directly correlated the firing frequency of a CA3* PN to its numbers of afferents. Inhibition (from BCs and OLM cells combined) was shown to be the most important among all afferents and EC afferents were the second most important in selecting a CA3 PN to be part of a stored pattern. This is consistent with the fact that EC is the excitatory input that drives inhibition via BCs as we explain in more detail below. The next afferent in importance was DG*. Interestingly, recurrent connections from CA3* PNs were

less important. For completion, we also note that the synaptic and cellular correlates of pattern formation in CA3 were also replicated for the corresponding pattern in DG (data not shown). We consider a third level of analysis in the next section, to separate the contributions of BCs and OLM cells to the overall inhibition, i.e., we asked what the differential roles of BCs and OLM cells were in making a PN active, and how these cell types influence competition among CA3* PNs. The model also suggested the existence of excitatory plasticity in EC-CA3* and CA3*-CA3* connections, and minimal inhibitory plasticity. Finally, the model helped quantify the shift in relative importance of the afferents in impacting the firing frequency of a PN during the retrieval phase (low ACh) as EC: 1; Combined BC and OLM: 0.69; DG: 0.02; CA3: 0.21.

Inhibition by BC and OLM interneurons differentially effect CA3* PNs

The analysis in the previous section indicated that the most important input in determining which PN was recruited into the CA3 pattern was the number of inhibitory connections that a PN received from BC and OLM interneurons as a group. We then asked what the individual contributions of the interneuron types might be to this overall inhibition and to competition among CA3* PNs. Considering morphology (Fig. 2), BCs make perisomatic synapses onto CA3 cells, have arborized axons and also project to neighboring OLM cells; OLM cells synapse distally on dendrites. BCs and OLM cells have similar biological spontaneous rates of 1.9 Hz (Seegerstrale et al. 2010).

We first studied the influence of the two inhibitory cell types on pattern size in CA3 by considering three cases: control, BCs inactivated and OLMs inactivated. The reader is reminded that the number of active cells ($z > 2.58$, see methods) represented the pattern

size, and that a typical CA3 cell received the following numbers of connections from BCs and OLM cells: 3.1 ± 1.0 from BCs and 2.8 ± 0.8 from OLM cells. The BCs or OLM cells were selectively inactivated (by inactivating synaptic projections to and from the cells), and the model was run for 20 trials to ensure that the pattern size stabilized. With inactivation of BCs, the pattern size increased by about 17% from the control case in five trials and then decreased by 4% from trial 5 to trial 20. When OLM cells were inactivated, the pattern size increased by about 50% from the control case in five trials and then decreased by 28% from trial 5 to trial 20. While these ‘artificial’ scenarios did demonstrate the role of inhibition, they failed to shed light on the specific roles that each cell type may play.

We then performed a comparison of connections for active and inactive CA3* PNs, by afferents from BCs and OLM cells separately for various cases of EC inputs, as in the preceding section. To our surprise, such a connection analysis did not reveal any trends between BCs and OLM cells, although the combined inhibition from both cell types had a clear trend as described in the previous section. This led us to explore the differences in firing rates between BCs and OLM cells as a potential factor that led to this negative result. Interestingly, such an analysis revealed significant differences in firing rate distributions among the two cell types (Fig. 3A), with BCs having widely varying rates (range: 4.4 to 79.6 Hz; mean 41.3 ± 20.3) while OLM cells were comparatively homogeneous (6.4 to 34.4 Hz; mean 16.9 ± 6.8). Variation in firing rates were found to be consistent with biological afferent connectivity, with BCs receiving excitation from CA3*, DG* and EC PNs, and OLM cells only from CA3* PNs (Fig. 2). We then performed two additional analyses

described next, to characterize inhibition from these two interneurons: a regression analysis, and a selective inactivation of inhibition by BCs and by OLM cells.

Regression analysis. To incorporate the huge variations in firing rates for BCs, we first normalized the connection numbers from BCs with a factor = (its own firing rate/maximum BC firing rate). For consistency, the same normalization was also performed for the OLM connections. These normalized values for BC and OLM cell connections were used to develop a regression model for CA3 firing frequency as follows: CA3* cell firing frequency = $8.20 - 1.19 * (\# \text{ of normalized BC inputs}) - 0.41 * (\# \text{ of normalized OLM inputs})$, for CA3* cells receiving 2, 3 or 4 EC inputs. The correlation with BC inputs was significant (coefficient $p < 0.05$), but no significant correlation was found for connections from OLM cells (coefficient $p < 0.5$). This suggests that, for CA3* PNs receiving 2, 3 or 4 EC inputs, both BCs and OLMs contribute to CA3* firing frequency, with the coefficient related to BCs being three times larger than the one for OLMs. However, OLM cells had a larger effect on CA3* cells that received only 1 EC input, as indicated by the regression equation: CA3* cell firing frequency = $2.50 - 0.03 * (\# \text{ of normalized BC inputs}) - 0.99 * (\# \text{ of normalized OLM inputs})$. The correlation was significant with OLM inputs (coefficient $p < 0.001$), but not with BC inputs (coefficient $p < 1$). This suggests that effectiveness of inhibition by these two cell types on CA3* PNs may depend on the types of afferents a CA3* PN receives. We tested whether this finding could be replicated using another study described next.

Selective inactivation of BCs and OLM cells. We investigated further the finding that inhibition by BCs was more potent for CA3* cells receiving more EC inputs and inhibition

by OLM cells was more important for CA3* cells receiving fewer or no EC inputs. For this we performed two additional inactivation runs. Running the model with BCs inactivated revealed that 12% of previously inactive CA3* cells (26/216) became active. These PNs received an average of 1.84 ± 0.8 inputs from active EC cells (see Fig. 2D). On the other hand, running the model with OLM cells inactivated revealed that 56% of previously inactive CA3* PNs (120/216) became active. Those 120 cells received an average of 1.47 ± 0.8 inputs from active EC cells. The numbers of EC inputs that these two groups received differed significantly ($p < 0.05$). This then provides support to the finding above from a regression analysis that BCs are more effective in inhibiting CA3* PNs that received more inputs from EC, and the OLM cells for the ones that receive fewer EC inputs.

Competition among CA3* PNs for recruitment into a CA3 pattern

The preceding analysis indicated that inhibition from both BCs and OLM cells plays a major role in determining activity in CA3. Since excitation to these interneurons shapes this inhibition, we then probed the characteristics of this disynaptic inhibition. For this we first investigated the relative roles of the excitatory inputs from EC, CA3* and DG* PNs in shaping the firing frequency of BCs via a regression model, and found that BC firing frequency = $-8.1 + 13.9 * (\# \text{ EC connections}) + 0.59 * (\# \text{ CA3* connections}) + 1.30 * (\# \text{ of DG* connections})$; the significance values for the coefficients were $p < 0.001$, 0.1, and 0.01, in that order. Since the numbers of connections and synaptic weights differed among the afferents, we normalized them as cited earlier (see methods for # of connections and weights). This revealed the relative factors for EC, CA3* and DG as 1, 0.04 and 0.35, respectively. In a similar regression model for OLM cells, a significant correlation with the

number of CA3 inputs ($p < 0.005$) was found, as expected (Fig. 3B). Separate regression analyses for CA3* PN groups with different numbers of EC inputs also showed the same trends (Fig. 3C). This analysis suggests that there might be competition among CA3* cells for recruitment into the stored pattern, via BCs and OLM cells. To investigate the competitive effect among CA3* PNs further, we performed a connections analysis of disynaptic inhibition via these two interneuron types.

Firing frequency vs. disynaptic inhibitory inputs. A connections analysis was performed using disynaptic inhibitory connections from other CA3* PNs to a CA3* PN via BCs and OLM cells separately. Since EC had a dominant effect on firing frequency of CA3* PNs, subgroups with different numbers of EC inputs were considered as in previous cases. Such an analysis showed that the number of disynaptic inhibitory inputs that a CA3* PN received from excitatory PNs (EC + DG* + CA3* PNs) via BCs correlated with high significance to firing frequency for PNs that received 3 EC inputs ($p < 0.001$); the correlation was comparatively less significant for connections via OLMs ($p < 0.05$). For CA3* PNs receiving 2 EC inputs, the number of disynaptic connections via BCs was not significantly correlated ($p < 0.5$), while those via OLM cells was again weakly significant ($p < 0.05$). On the other hand, for CA3* PNs that received 1 EC input, the opposite was noted, i.e., the number of disynaptic connections via OLMs was very significantly correlated to the firing frequency of CA3* PNs ($p < 0.001$), while the number of disynaptic connections via BCs was not ($p < 0.5$).

These analyses provided several insights about competition among CA3* PNs. First, EC and DG* afferents have a larger influence on BC firing rates, compared to

recurrent collaterals from CA3* cells. Second, in one form of competition, both EC and DG* afferents aid CA3* PNs in inhibiting other CA3* PNs via BCs. This disynaptic inhibition could then prevent a CA3* PN from being recruited into the stored CA3 pattern. This form of disynaptic inhibition was effective for PNs that received higher numbers of EC inputs. Third, disynaptic inhibition via OLM cells was different from that via BCs, in that OLM cells received excitatory afferents only from CA3* PNs, an artifact of biological connectivity (see methods). Disynaptic inhibition via OLM cells was also important in the competition, but was effective for PNs that received fewer EC inputs.

Role of inhibitory plasticity. We next asked whether plasticity of inhibition was significant and whether it had any role in pattern formation. Model runs showed that excitatory plasticity in the EC-CA3* and CA3*-CA3* synapses grew in five trials by an average of 33% and 48%, respectively; extending the trials to 50 showed the additional growth to be very modest, confirming that sufficient balance between excitation and inhibition had been achieved in five trials. Interestingly, in five trials, BC-CA3* synapses showed a potentiation of only 6%, and OLM-CA3* showed a small depression of 6%. This suggests that excitatory plasticity is important, but it is inhibition and not inhibitory plasticity that is significant.

Back-projections from CA3 to DG promote separation as well as increased storage in CA3

Experiments suggest that the back-projection from CA3 to DG increases pattern separation during the encoding phase (high ACh), via disynaptic inhibition pathway in DG

(Leutgeb et al. 2007). That is, pyramidal cells in CA3 inhibit those DG granule cells which project to them and help increase pattern separation in both DG and in CA3. A consequence is increased capacity for storing patterns in CA3. Myers et al. (2011) were the first to investigate this using an innovative framework involving an artificial neural network. These authors assumed direct inhibition from CA3 pyramidal cells to DG granule cells and showed that back-projections increases the storage capacity in CA3. We extend this investigation by exploring the underlying cellular processes involved in this change in storage capacity using a biologically realistic model. Myers et al. (2011) included one back-projecting inhibitory CA3-DG connection for every DG-CA3 connection. We used the same logic, but in contrast to the Myers et al. (2011) scheme where the CA3 cell directly inhibited DG granule cells, we used an indirect pathway. That is, back projections in our model were from the same CA3 cell to DG interneurons, consistent with biology (Leutgeb et al., 2007), and these interneurons then inhibited the DG granule cell. These CA3-DG back-projections resulted in both increased pattern completion in CA3 (17% change in area under the curve of Fig.4; $p < 0.005$), and increased pattern separation in DG (23% similarly for the DG curve; $p < 0.005$). Importantly, back-projection to DG resulted in a decrease in pattern size in CA3 by 16%.

For comparison, we replicated the effect of a hypothetical direct pathway in Myers et al. (2011) by adding inhibitory back-projection connections (probability of 1.5% for each DG-CA3 connection), i.e., a back-projecting CA3-DG inhibitory connection for each mossy fiber DG-CA3 excitatory connection. The hypothetical direct pathway increased pattern separation in DG by 13% ($p < 0.005$; data not shown), increased pattern completion in CA3 by 9% ($p < 0.005$; data not shown), and decreased pattern size in CA3 by 10%.

Compared to the hypothetical direct pathway, the physiological indirect pathway additionally improved pattern separation in DG 10%, and pattern completion in CA3 by 8%, and increased pattern storage in CA3 by 6%.

DISCUSSION

We adapted a prior model (Hummos et al. 2014) to develop a fully biophysical conductance-based network model of the CA3 and DG regions of the hippocampus. As stated in methods, we used exactly the same prior model except for the single cell components, i.e., all network parameters including spatial connectivity patterns, channel and synaptic function, short- and long-term plasticity, as well as neuromodulatory state, were unchanged. Single cell models in CA3 and DG regions of the present model have all the reported currents (see methods) and reproduced the passive and current injection responses reported in biology (Brown and Randall 2009; Staley et al. 1992). We first confirmed that the network model matched the characteristics of pattern separation/completion and the hypothesized role of the intrinsic mechanisms in stabilizing network dynamics during encoding and retrieval phases (Hummos et al. 2014). The realistic network model was then used to study the cellular and synaptic correlates of pattern formation in CA3, including the differential roles of the excitatory (EC, DG, CA3 recurrent collaterals) and inhibitory (BC, OLM) afferents. Specifically, we investigated how the various afferents interacted with intrinsic mechanisms to form a memory in CA3 of the pattern projected from EC. Furthermore, the analysis shed new light on the differing functional roles of BCs and OLM cells in this memory formation.

Differential roles of afferents in memory formation in CA3

Memory formation is thought to involve several factors including extrinsic and intrinsic connectivity among the cell types, as well as cell intrinsic, synaptic and plasticity mechanisms. We explored the role of these factors in the formation of the memory in CA3, termed ‘encoding’, with the repeated presentation of an input pattern via EC. During this encoding phase, ACh levels are known to be high in the hippocampus, aiding separation of patterns in CA3, including via enhanced inputs from DG (Hasselmo et al. 1995).

EC inputs arrive at CA3 via both direct and indirect (via DG) pathways, engendering modest excitatory and minimal inhibitory plasticity in specific connections that, together with short-term plasticity and neuromodulatory effects formed the model memory pattern in CA3. Analysis revealed that although 86% of the CA3 cells received inputs from EC (CA3* cells), only 31% were recruited into the pattern, or were ‘active’ (the corresponding number in DG was 10%); the rest of the CA3* cells were inactive. Competition was also shown to play a role in constraining the size of the memory/pattern in CA3. CA3* PNs with increasing numbers of afferents from EC were found to have a higher probability of being active, with a maximum of 1 for CA3* cells with four EC afferents. As cited in results, two separate analyses (using connection numbers and a regression analysis) revealed that the most significant afferent in recruiting a PN into a CA3 pattern was combined inhibition from BCs and OLM cells. We elaborate on the underlying mechanisms in inhibition in the next section. Consistent with this, input from EC was 35% less important than combined inhibition, based on the regression coefficients cited in results. Several underlying mechanisms contributed to the EC afferent being the most important when considered individually. First, the connection probabilities from EC

to CA3 were higher compared to the corresponding ones from DG (see methods). Second, EC excitatory connections to CA3 potentiated more than those to DG. Finally, EC afferents also helped generate plasticity in CA3*-CA3* connections for effective ‘binding’ of the pattern. Afferents from DG* cells were also significant in pattern formation, but played a much less prominent role, 51% less important than inhibition. Interestingly, contrary to expectations, excitation from the recurrent CA3* collaterals did not appear to play a role in the selection of CA3* PNs to the stored pattern. In fact, the number of recurrent connections from other active CA3* cells was similar for both active and inactive CA3* PNs. However, as we report in the next section, an important finding was that CA3* PNs play a key role in disynaptic inhibition.

Analysis also revealed a process of competition among the CA3* cells during recruitment into the stored pattern, i.e., in determining which CA3* PN became active after the five-trial training with EC pattern 1. This is consistent with the formation of memories in other regions, e.g., Pavlovian fear conditioning results in ~20% of the amygdala PNs being recruited into the fear memory trace, even though 70% of PNs receive tone and shock inputs. The amygdalar fear memory trace was hypothesized to occur via competition among the PNs (e.g., Han et al. 2009), and this competition among PNs was demonstrated using a computational model (Feng et al. 2016; Kim et al. 2013a). Different from the process in the amygdala where the pairing of tone and shock led to memory formation, the strong shock input of amygdala is replaced by the physiological setting of multiple afferents from EC, DG* and CA3* PNs in the present model, as described in results. However, similar to the amygdala, inhibition was found to play a key role in the formation of the pattern in CA3, with two functionally distinct inhibitory synapses BC-CA3 and

OLM-CA3, and with BCs reacting earlier than OLM cells due to their faster rise and decay times; we elaborate on the differential roles of BCs and OLM cells in the next section.

As another finding, we showed how back-projections from CA3 to DG reduced pattern size in DG in a state-dependent manner, and how the strong mossy fiber connections to the CA3* PNs can both supplement lack of EC input, or add inhibition via disynaptic connections involving BCs (recall that BCs receive 10 times more connections from DG compared to those from CA3). The net effect in our model was a 16% reduction in pattern size in CA3. Also, during the retrieval phase (low levels of ACh), CA3*-CA3* connections were found to be more important compared to the DG* afferents, i.e., there was a switch in importance between these two CA3 afferents.

Two distinct inhibitory mechanisms facilitate pattern storage in CA3

The functional significance of different types of interneurons in the hippocampus, as in other brain regions, is still not well understood (Hu et al. 2014). Our model considered BCs and OLM cells, which are thought to be the important inhibitory cells in CA3 (Lawrence et al. 2006; Vida 2010). Several physiological considerations endow the two cell types with different roles. First, compared to OLM cells, BCs receive fewer connections from CA3 PNs (Buhl and Whittington, 2007). However, projections from DG to BCs outnumber those from CA3 by a factor of 10 (Acsády et al. 1998). OLM cells, on the other hand make many more synapses compared to BCs, and receive reciprocal connections from the same PNs they project to, in line with their function as feedback cells. They receive limited input from sources other than pyramidal cells (Maccaferri, 2005). Second, BCs provide peri-somatic inhibition, while OLM cells project to dendrites.

Finally, BC synapses exhibit considerably faster rise and decay dynamics compared to OLM cells (Bartos et al. 2010).

Model runs suggest that these differential connectivity and synaptic dynamic characteristics enable BCs and OLM cells to participate in memory formation via distinct mechanisms. Compared to BCs, OLM cells exhibit slow membrane dynamics with time constants of 10 ms and 71 ms, respectively (Bartos and Elgueta 2012; Lawrence et al. 2006), and, as cited, receive limited input from sources other than CA3 PNs (Maccaferri, 2005). Also, the inhibitory projections to PNs differed considerably between BCs and OLM cells, with synaptic GABA_A rise/decay times of 0.21/3.3 ms and 2.8/20.8 ms, respectively (Bartos et al. 2010). This implies that BCs are well suited to respond to intense activity such as that follows each theta stimulation from EC. However, since they receive limited connections from CA3 PNs and have fast membrane dynamics, BCs are not positioned to capture the ‘reverberation’ activity among the CA3 PNs. On the other hand, OLM cells receive multiple CA3 afferents. This, together with their slower membrane dynamics permit them to ‘integrate’ activity among CA3 PNs effectively. Indeed, this ability to integrate, together with their reciprocal connectivity to CA3 PNs, underlies the very important role of OLM cells in controlling run-away excitation within CA3 (Hummos et al. 2014). So, although inhibition by OLM is delayed, it is nevertheless effective as shown in the preceding section. Due to their extensive connectivity, inhibition by OLMs cells tends to be somewhat generalized. Also, the slower synaptic dynamics implies that OLM inhibition cannot suppress CA3 PN activity immediately following EC input. On the other hand, differential excitatory connectivity (reduced afferents from CA3 PNs, but recipient of EC and DG afferents) and faster synaptic dynamics positions BCs to provide

rapid and targeted inhibition of CA3 PNs. Interestingly, the connectivity pattern also favored targeted inhibition by BCs. This was because EC projections targeting a CA3 PN also contacted local BCs with high probability indicating that a PN receiving multiple EC afferents was also likely to receive inhibition by BCs that were recipients of the same EC afferents. The opposite was true for PNs that received fewer inputs, i.e., they were more likely to receive effective inhibition from OLMs and not BCs, because the local BCs for those PNs also received fewer EC inputs. These insights from the model reveal how the functional requirements of inhibition are divided and effectively performed by BCs and OLM cells.

Another finding was that although plasticity in the excitatory connections (EC-CA3 and CA3-CA3) was modest but important, inhibitory plasticity (in BC-CA3 and OLM-CA3 synapses) was insignificant in pattern formation. This suggests that excitatory plasticity and inhibition by BCs and OLM cells, and not inhibitory plasticity, are important in CA3 pattern formation. Also, this excitatory plasticity would exert its effect via disynaptic inhibition as discussed in results. That is, increased firing of select CA3* cells due to this excitatory plasticity can effectively suppress other CA3* cells via BCs and OLM cells. Analysis of model output revealed training-induced increase in z-scores for 41% and decrease for 11% of the CA3* PNs, providing support for such a competitive effect.

Model predictions

The study provides several predictions, some of which are testable. First, the probability that a CA3 PN is recruited into a pattern/memory trace is proportional to its EC afferent abundance: for our model structure, the probabilities were 1 for CA3 PNs

that received 4 EC inputs, 0.62 for those that received 3 EC inputs, 0.37 for those that received 2 EC inputs and 0.15 for those that received 1 EC input. Second, the model predicts the relative importance of the CA3 afferents in determining whether it would be part of the memory trace as inhibitory afferents (BCs and OLM cells combined): 1.0; EC: 0.65, DG*: 0.49, CA3*: 0.07. The third prediction is that inactivation of OLM-CA3 connections should result in a larger memory trace, compared to inactivation of the BC-CA3 connections. Finally, the model predicts that BCs control CA3 PNs that receive larger numbers of EC afferents, and OLM cells the opposite. Of these, the last two should be testable presently with modern tools such as optogenetics.

CONCLUSION

The functional relationship between structure, connectivity, cell types, plasticity and the role of extrinsic inputs in memory formation is difficult to study in experiments due to distributed and simultaneous interactions. A biologically-based model of the hippocampus (CA3 and DG regions) is suited for such studies. As cited earlier, although some of the trends reported may perhaps be expected, model analyses of the type reported provide biological realism and also enable quantification of the notion of relative importance for the contributory mechanisms. Such a network model comprising realistic single cell models with channel and synaptic dynamics, short- and long-term plasticity, and known effects of neuromodulation, provided important insights into the cellular and synaptic correlates of pattern formation. First, the model enabled quantification of the relative importance of the afferents to a CA3 cell as cited in the previous section on predictions. Second, BCs and OLM cells had differential roles in inhibition, with BCs

being effective for CA3 PNs that received higher numbers of inputs from EC, and OLMs for PNs that received fewer inputs. This enabled larger involvement by BCs in selecting CA3 cells that formed part of the pattern, while OLM cells had a more general role of controlling the spread of excitation, and regulating pattern size. The model also shed light on the underlying mechanisms involved in such pattern formation, including a new disinaptic inhibitory mechanism that involved excitation from both EC and DG regions. Third, we quantified the known effects of back-projections from CA3 to DG and showed that they reduced pattern size by 16% in CA3. Finally, these findings also provided predictions cited in the previous section. We also note that the biologically-based model and analysis framework is suited for studying other hippocampal phenomena such as oscillations that require high fidelity in modeling the intrinsic mechanisms. Furthermore, the deeper insights into the cellular and synaptic correlates of pattern formation provided by the proposed formulations have potential applicability to formation of memory in other brain regions.

REFERENCES

- Acsády L, Kamondi A, Sík A, Freund T, and Buzsáki G.** GABAergic cells are the major postsynaptic targets of mossy fibers in the rat hippocampus. *J Neurosci* 18: 3386-3403, 1998.
- Ali AB, Deuchars J, Pawelzik H, and Thomson AM.** CA1 pyramidal to basket and bistratified cell EPSPs: dual intracellular recordings in rat hippocampal slices. *J Physiol* 507 (Pt 1): 201-217, 1998.
- Ali AB, and Thomson AM.** Facilitating pyramid to horizontal oriens-alveus interneurone inputs: dual intracellular recordings in slices of rat hippocampus. *J Physiol* 507: 185-199, 1998.
- Bakker A, Kirwan CB, Miller M, and Stark CE.** Pattern separation in the human hippocampal CA3 and dentate gyrus. *Science* 319: 1640-1642, 2008.
- Barkai E, Bergman RE, Horwitz G, and Hasselmo ME.** Modulation of associative memory function in a biophysical simulation of rat piriform cortex. *J Neurophysiol* 72: 659-677, 1994.
- Barry C, Heys JG, and Hasselmo ME.** Possible role of acetylcholine in regulating spatial novelty effects on theta rhythm and grid cells. *Front Neural Circuits* 6: 5, 2012.
- Bartos M, and Elgueta C.** Functional characteristics of parvalbumin- and cholecystokinin-expressing basket cells. *J Physiol* 590: 669-681, 2012.
- Bartos M, Sauer J-F, Vida I, and Kulik Á.** Fast and slow GABAergic transmission in hippocampal circuits. In: *Hippocampal Microcircuits: A Computational Modeler's Resource Book*, edited by Cutsuridis V, Graham B, Cobb S, and Vida I. New York, NY: Springer New York, 2010, p. 129-161.
- Bianchi R, and Wong RK.** Carbachol-induced synchronized rhythmic bursts in CA3 neurons of guinea pig hippocampus in vitro. *J Neurophysiol* 72: 131-138, 1994.
- Bliss TV, and Gardner-Medwin AR.** Long-lasting potentiation of synaptic transmission in the dentate area of the unanaesthetized rabbit following stimulation of the perforant path. *J Physiol* 232: 357-374, 1973.
- Bower MR, and Buckmaster PS.** Changes in granule cell firing rates precede locally recorded spontaneous seizures by minutes in an animal model of temporal lobe epilepsy. *J Neurophysiol* 99: 2431-2442, 2008.
- Brown JT, and Randall AD.** Activity-dependent depression of the spike after-depolarization generates long-lasting intrinsic plasticity in hippocampal CA3 pyramidal neurons. *J Physiol* 587: 1265-1281, 2009.
- Buhl EH, Szilagy T, Halasy K, and Somogyi P.** Physiological properties of anatomically identified basket and bistratified cells in the CA1 area of the rat hippocampus in vitro. *Hippocampus* 6: 294-305, 1996.
- Byrne JH, Roberts JL, and Waxham MN.** *From Molecules to Networks: An introduction to cellular and molecular neuroscience*. Elsevier, 2014.
- Carnevale N, and Hines M.** *The NEURON Book*. UK: Cambridge University Press, 2006.
- Cea-del Rio CA, Lawrence JJ, Tricoire L, Erdelyi F, Szabo G, and McBain CJ.** M3 muscarinic acetylcholine receptor expression confers differential cholinergic modulation to neurochemically distinct hippocampal basket cell subtypes. *J Neurosci* 30: 6011-6024, 2010.
- Cobb S, and Lawrence JJ.** Neuromodulation of hippocampal cells and circuits. In: *Hippocampal Microcircuits: A Computational Modeler's Resource Book*, edited by Cutsuridis V, Graham B, Cobb S, and Vida I. New York, NY: Springer New York, 2010, p. 187-246.
- Cutsuridis et al. e.** *Hippocampal microcircuits : a computational modeler's resource book*. New York: Springer, 2010.
- Destexhe A, Mainen ZF, and Sejnowski TJ.** Kinetic models of synaptic transmission. *Methods Neuronal Model* 2: 1-26, 1998.
- Do VH, Martinez CO, Martinez JL, Jr., and Derrick BE.** Long-term potentiation in direct perforant path projections to the hippocampal CA3 region in vivo. *J Neurophysiol* 87: 669-678, 2002.

Feng F, Samarth P, Pare D, and Nair SS. Mechanisms underlying the formation of the amygdalar fear memory trace: A computational perspective. *Neuroscience* 322: 370-376, 2016.

Gulyas AI, Miles R, Sik A, Toth K, Tamamaki N, and Freund TF. Hippocampal pyramidal cells excite inhibitory neurons through a single release site. *Nature* 366: 683-687, 1993.

Han JH, Kushner SA, Yiu AP, Hsiang HL, Buch T, Waisman A, Bontempo B, Neve RL, Frankland PW, and Josselyn SA. Selective erasure of a fear memory. *Science* 323: 1492-1496, 2009.

Hasselmo ME, Schnell E, and Barkai E. Dynamics of learning and recall at excitatory recurrent synapses and cholinergic modulation in rat hippocampal region CA3. *J Neurosci* 15: 5249-5262, 1995.

Hasselmo ME, and Wyble BP. Free recall and recognition in a network model of the hippocampus: simulating effects of scopolamine on human memory function. *Behav Brain Res* 89: 1-34, 1997.

Hefft S, and Jonas P. Asynchronous GABA release generates long-lasting inhibition at a hippocampal interneuron-principal neuron synapse. *Nat Neurosci* 8: 1319-1328, 2005.

Hemond P, Epstein D, Boley A, Migliore M, Ascoli GA, and Jaffe DB. Distinct classes of pyramidal cells exhibit mutually exclusive firing patterns in hippocampal area CA3b. *Hippocampus* 18: 411-424, 2008.

Henze DA, Wittner L, and Buzsaki G. Single granule cells reliably discharge targets in the hippocampal CA3 network in vivo. *Nat Neurosci* 5: 790-795, 2002.

Hoskison MM, Connor JA, and Shuttleworth CW. GABAB-receptor modulation of short-term synaptic depression at an excitatory input to murine hippocampal CA3 pyramidal neurons. *Neurosci Lett* 365: 48-53, 2004.

Hu H, Gan J, and Jonas P. Interneurons. Fast-spiking, parvalbumin(+) GABAergic interneurons: from cellular design to microcircuit function. *Science* 345: 1255-1263, 2014.

Hummos A, Franklin CC, and Nair SS. Intrinsic mechanisms stabilize encoding and retrieval circuits differentially in a hippocampal network model. *Hippocampus*, in press: 2014.

Hunsaker MR, and Kesner RP. The operation of pattern separation and pattern completion processes associated with different attributes or domains of memory. *Neurosci Biobehav Rev* 37: 36-58, 2013.

Ishizuka N, Weber J, and Amaral DG. Organization of intrahippocampal projections originating from CA3 pyramidal cells in the rat. *J Comp Neurol* 295: 580-623, 1990.

Jung MW, and McNaughton BL. Spatial selectivity of unit activity in the hippocampal granular layer. *Hippocampus* 3: 165-182, 1993.

Katona I, Acsady L, and Freund TF. Postsynaptic targets of somatostatin-immunoreactive interneurons in the rat hippocampus. *Neuroscience* 88: 37-55, 1999.

Kim D, Pare D, and Nair SS. Assignment of model amygdala neurons to the fear memory trace depends on competitive synaptic interactions. *J Neurosci* 33: 14354-14358, 2013b.

Kim D, Pare D, and Nair SS. Mechanisms contributing to the induction and storage of Pavlovian fear memories in the lateral amygdala. *Learn Mem* 20: 421-430, 2013a.

Kneisler TB, and Dingledine R. Spontaneous and synaptic input from granule cells and the perforant path to dentate basket cells in the rat hippocampus. *Hippocampus* 5: 151-164, 1995.

Kremin T, and Hasselmo ME. Cholinergic suppression of glutamatergic synaptic transmission in hippocampal region CA3 exhibits laminar selectivity: Implication for hippocampal network dynamics. *Neuroscience* 149: 760-767, 2007.

Kunec S, Hasselmo ME, and Kopell N. Encoding and retrieval in the CA3 region of the hippocampus: a model of theta-phase separation. *J Neurophysiol* 94: 70-82, 2005.

Lawrence JJ, Statland JM, Grinspan ZM, and McBain CJ. Cell type-specific dependence of muscarinic signalling in mouse hippocampal stratum oriens interneurons. *J Physiol* 570: 595-610, 2006.

Lee I, and Kesner RP. Encoding versus retrieval of spatial memory: double dissociation between the dentate gyrus and the perforant path inputs into CA3 in the dorsal hippocampus. *Hippocampus* 14: 66-76, 2004.

Leutgeb JK, Leutgeb S, Moser MB, and Moser EI. Pattern separation in the dentate gyrus and CA3 of the hippocampus. *Science* 315: 961-966, 2007.

Li G, Amano T, Pare D, and Nair SS. Impact of infralimbic inputs on intercalated amygdala neurons: a biophysical modeling study. *Learn Mem* 18: 226-240, 2011.

Li G, Nair SS, and Quirk GJ. A biologically realistic network model of acquisition and extinction of conditioned fear associations in lateral amygdala neurons. *J Neurophysiol* 101: 1629-1646, 2009.

Li XG, Somogyi P, Ylinen A, and Buzsaki G. The hippocampal CA3 network: an in vivo intracellular labeling study. *J Comp Neurol* 339: 181-208, 1994.

Maccaferri G. Stratum oriens horizontal interneurone diversity and hippocampal network dynamics. *J Physiol* 562: 73-80, 2005.

Maffei A. The many forms and functions of long term plasticity at GABAergic synapses. *Neural Plast* 2011: 254724, 2011.

Marr D. Simple memory: a theory for archicortex. *Philos Trans R Soc Lond B Biol Sci* 262: 23-81, 1971.

McClelland JL, and Goddard NH. Considerations arising from a complementary learning systems perspective on hippocampus and neocortex. *Hippocampus* 6: 654-665, 1996.

McQuiston AR, and Madison DV. Muscarinic receptor activity has multiple effects on the resting membrane potentials of CA1 hippocampal interneurons. *J Neurosci* 19: 5693-5702, 1999a.

McQuiston AR, and Madison DV. Nicotinic receptor activation excites distinct subtypes of interneurons in the rat hippocampus. *J Neurosci* 19: 2887-2896, 1999b.

Miles R. Synaptic excitation of inhibitory cells by single CA3 hippocampal pyramidal cells of the guinea-pig in vitro. *J Physiol* 428: 61-77, 1990.

Miles R, and Wong RK. Single neurones can initiate synchronized population discharge in the hippocampus. *Nature* 306: 371-373, 1983.

Misgeld U, Müller W, and Polder HR. Potentiation and suppression by eserine of muscarinic synaptic transmission in the guinea-pig hippocampal slice. *J Physiol* 409: 191-206, 1989.

Mizuseki K, Royer S, Diba K, and Buzsaki G. Activity dynamics and behavioral correlates of CA3 and CA1 hippocampal pyramidal neurons. *Hippocampus* 22: 1659-1680, 2012.

Myers CE, and Scharfman HE. Pattern separation in the dentate gyrus: a role for the CA3 backprojection. *Hippocampus* 21: 1190-1215, 2011.

Naber PA, Caballero-Bleda M, Jorritsma-Byham B, and Witter MP. Parallel input to the hippocampal memory system through peri- and postrhinal cortices. *Neuroreport* 8: 2617-2621, 1997.

Neunuebel Joshua P, and Knierim James J. CA3 retrieves coherent representations from degraded input: Direct evidence for CA3 pattern completion and dentate gyrus pattern separation. *Neuron* 81: 416-427, 2014.

Neves G, Cooke SF, and Bliss TVP. Synaptic plasticity, memory and the hippocampus: a neural network approach to causality. *Nat Rev Neurosci* 9: 65-75, 2008.

O'Reilly RC, and McClelland JL. Hippocampal conjunctive encoding, storage, and recall: avoiding a trade-off. *Hippocampus* 4: 661-682, 1994.

Rolls ET, and Kesner RP. A computational theory of hippocampal function, and empirical tests of the theory. *Prog Neurobiol* 79: 1-48, 2006.

Santhakumar V, Aradi I, and Soltesz I. Role of mossy fiber sprouting and mossy cell loss in hyperexcitability: a network model of the dentate gyrus incorporating cell types and axonal topography. *J Neurophysiol* 93: 437-453, 2005.

Scharfman HE. The CA3 "backprojection" to the dentate gyrus. *Prog Brain Res* 163: 627-637, 2007.

Scharfman HE. Evidence from simultaneous intracellular recordings in rat hippocampal slices that area CA3 pyramidal cells innervate dentate hilar mossy cells. *J Neurophysiol* 72: 2167-2180, 1994.

Segerstrale M, Juuri J, Lanore F, Piepponen P, Lauri SE, Mulle C, and Taira T. High firing rate of neonatal hippocampal interneurons is caused by attenuation of afterhyperpolarizing potassium currents by tonically active kainate receptors. *J Neurosci* 30: 6507-6514, 2010.

Shouval HZ, Castellani GC, Blais BS, Yeung LC, and Cooper LN. Converging evidence for a simplified biophysical model of synaptic plasticity. *Biol Cybern* 87: 383-391, 2002a.

Sik A, Penttonen M, Ylinen A, and Buzsaki G. Hippocampal CA1 interneurons: an in vivo intracellular labeling study. *J Neurosci* 15: 6651-6665, 1995.

Staley KJ, Otis TS, and Mody I. Membrane properties of dentate gyrus granule cells: comparison of sharp microelectrode and whole-cell recordings. *J Neurophysiol* 67: 1346-1358, 1992.

Tóth K. Glutamatergic neurotransmission in the hippocampus. In: *Hippocampal Microcircuits: A Computational Modeler's Resource Book*, edited by Cutsuridis V, Graham B, Cobb S, and Vida I. New York, NY: Springer New York, 2010, p. 99-128.

Treves A, and Rolls ET. Computational constraints suggest the need for two distinct input systems to the hippocampal CA3 network. *Hippocampus* 2: 189-199, 1992.

Tropp Sneider J, Chrobak JJ, Quirk MC, Oler JA, and Markus EJ. Differential behavioral state-dependence in the burst properties of CA3 and CA1 neurons. *Neuroscience* 141: 1665-1677, 2006.

Varela JA, Sen K, Gibson J, Fost J, Abbott LF, and Nelson SB. A quantitative description of short-term plasticity at excitatory synapses in layer 2/3 of rat primary visual cortex. *J Neurosci* 17: 7926-7940, 1997.

Vida I. Morphology of hippocampal neurons. In: *Hippocampal Microcircuits: A Computational Modeler's Resource Book*, edited by Cutsuridis V, Graham B, Cobb S, and Vida I. New York, NY: Springer New York, 2010, p. 27-67.

Vogt KE, and Regehr WG. Cholinergic modulation of excitatory synaptic transmission in the CA3 area of the hippocampus. *J Neurosci* 21: 75-83, 2001.

Witter MP. Connectivity of the Hippocampus. In: *Hippocampal Microcircuits: A Computational Modeler's Resource Book*, edited by Cutsuridis V, Graham B, Cobb S, and Vida I. New York, NY: Springer New York, 2010, p. 5-26.

Wittner L, Henze DA, Zaborszky L, and Buzsaki G. Three-dimensional reconstruction of the axon arbor of a CA3 pyramidal cell recorded and filled in vivo. *Brain Struct Funct* 212: 75-83, 2007.

Wong RK, and Prince DA. Afterpotential generation in hippocampal pyramidal cells. *J Neurophysiol* 45: 86-97, 1981.

Woodin MA, Ganguly K, and Poo MM. Coincident pre- and postsynaptic activity modifies GABAergic synapses by postsynaptic changes in Cl⁻ transporter activity. *Neuron* 39: 807-820, 2003.

Wolf NJ. Cholinergic systems in mammalian brain and spinal cord. *Prog Neurobiol* 37: 475-524, 1991.

APPENDIX

1. Mathematical Equations for voltage-dependent ionic currents

The equation for each compartment (soma or dendrite) followed the Hodgkin-Huxley formulations (Byrne et al. 2014) in eqn. A1,

$$C_m dV_s/dt = -g_L(V_s - E_L) - g_c(V_s - V_d) - \sum I_{cur,s}^{int} - \sum I_{cur,s}^{syn} + I_{inj} \quad (A1)$$

where V_s/V_d are the somatic/dendritic membrane potential (mV), $I_{cur,s}^{int}$ and $I_{cur,s}^{syn}$ are the intrinsic and synaptic currents in the soma, I_{inj} is the electrode current applied to the soma, C_m is the membrane capacitance, g_L is the is the conductance of leak channel, and g_c is the coupling conductance between the soma and the dendrite (similar term added for other dendrites connected to the soma). The intrinsic current $I_{cur,s}^{int}$, was modeled as $I_{cur,s}^{int} = g_{cur} m^p h^q (V_s - E_{cur})$, where g_{cur} is its maximal conductance, m its activation variable (with exponent p), h its inactivation variable (with exponent q), and E_{cur} its reversal potential (a similar equation is used for the synaptic current $I_{cur,s}^{syn}$ but without m and h). The kinetic equation for each of the gating variables x (m or h) takes the form

$$\frac{dx}{dt} = \frac{x_\infty(V, [Ca^{2+}]_i) - x}{\tau_x(V, [Ca^{2+}]_i)} \quad (A2)$$

where x_∞ is the steady state gating voltage- and/or Ca^{2+} - dependent gating variable and τ_x is the voltage- and/or Ca^{2+} - dependent time constant. Unless otherwise indicated, x_∞ is equal to $\alpha / (\alpha + \beta)$ and τ_x is equal to $1 / (\alpha + \beta)$ as listed in **Tables 1A-1C**. The equation for the dendrite follows the same format with ‘ s ’ and ‘ d ’ switching positions in eqn. A1. The specific current equations and other parameter values for each cell type are provided in **Tables 1A-1C**. For further details on the equations used for synaptic currents, calcium dynamics and Hebbian learning, and short-term plasticity, please refer to our previous study (Hummos et al., 2014).

Table A1: Parameter values for CA3 PNs.

Current Type	Soma G_{\max} (S/cm2)	Dend $_{\rho}$ G_{\max} (S/cm2)	Gating Variable	α	β
I_{Na}	0.031	0.015	$p = 3$	$\frac{0.32(13.1 - v)}{\exp[(13.1 - v)/4] - 1}$	$\frac{0.28(v - 40.1)}{\exp[(v - 40.1)/5] - 1}$
			$q = 1$	$0.128\exp[(17 - v)/18]$	$\frac{4}{\exp[(40 - v)/5] + 1}$
I_{Kdr}	0.06	0.03	$p = 3$	$\frac{-0.07(v - 47)}{\exp[(v - 47)/-6] - 1}$	$\frac{0.264}{\exp[(v - 22)/40]}$
			$q = 1$	$0.001\exp\left[-2(v + 61) \cdot \frac{F}{RT}\right]$	0.001
I_{KCa}	0.00055135	0.00055	$p = 1$	$\frac{0.28[Ca^{2+}]}{[Ca^{2+}] + \exp1(0.00048, 0.84, v)}$	$\frac{0.48}{1 + [Ca^{2+}]/\exp1(0.13e^{-6}, 1, v)}$
				$\exp1 = 0.00048\exp\left[-\frac{0.12Fv}{R[273.15 + degC]}\right]$	$\exp1 = 0.13e^{-6}\exp\left[-\frac{Fv}{R[273.15 + degC]}\right]$
I_M	0.007	0.001	$p = 4$	$-0.006\exp\left[0.6(v + 55) \cdot \frac{F}{RT}\right]$	$0.06\exp\left[-9.4(v + 55) \cdot \frac{F}{RT}\right]$
I_{CaL}	0.025	0.025	$p = 2$	$\frac{15.69(81.5 - v)}{\exp[(81.5 - v)/10] - 1}$	$0.29\exp[-v/10.86]$
			$p = 2$	$\frac{0.1967(19.98 - v)}{\exp[(19.98 - v)/10] - 1}$	$0.046\exp[-v/20.73]$
I_{CaN}	0.01	0.0001	$q = 1$	$0.00016\exp[-v/48.4]$	$\frac{1}{\exp[(39 - v)/10] + 1}$
			$p = 2$	$\frac{0.2(19.26 - v)}{\exp[(19.26 - v)/10] - 1}$	$0.009\exp[-v/22.03]$
I_{CaT}	0.0079	0.007	$q = 1$	$0.00016\exp[-v/16.26]$	$\frac{1}{\exp[(29.79 - v)/10] + 1}$
			$p = 1$	$1.3 * 10^{13}[Ca^{2+}]_i^4$	0.005
I_{KAHP}	0.001	0.0004	$p = 1$	$0.02\exp\left[1.8(v + 33.6) \cdot \frac{F}{RT}\right]$	$0.02\exp\left[-1.2(v + 33.6) \cdot \frac{F}{RT}\right]$
			$q = 1$	$0.08\exp\left[4(v + 83) \cdot \frac{F}{RT}\right]$	0.08
Diam μm	16	3	$C_m = 1.0 \mu F/cm^2$	$R_{axial} = 210 \Omega\text{-cm}$	$G_{leak} = 0.00018$
Length μm	16.8	150	$E_{Na} = 45 mV$	$E_K = -85 mV$	$E_{leak} = -70 mV$
				$X_{\infty} = \frac{\alpha}{\alpha + \beta}$	$\tau_x (ms) = \frac{1}{\alpha + \beta}$

Table A2: Parameter values for DG PNs.

Current Type	Soma G_{\max} (S/cm ²)	Dend ρ G_{\max} (S/cm ²)	Gating Variable	α	β
I_{Na}	0.08	0.08	$p = 3$ $q = 1$	$\frac{-0.3(v-25)}{\exp[(v-25)/-5] - 1}$ 0.23	$\frac{0.3(v-53)}{\exp[(v-53)/5] - 1}$ 3.33
I_{fKdr}	0.04	0.04	$p = 4$	$\frac{\exp[(v-3)/20] - 0.07(v-47)}{\exp[(v-47)/-6] - 1}$	$\frac{\exp[(v-55.5)/-10] + 1}{0.264}$
I_{sKdr}	0.13889	0.012	$p = 4$	$\frac{-0.028(v-35)}{\exp[(v-35)/-6] - 1}$ $-0.00642Vm - 0.1152$	$\frac{0.1056}{\exp[(v-10)/40]}$
I_C	0.0001	0.0001	$p = 2$	$\frac{\exp[-(Vm+18)/12] - 1}{Vm = v + 40\log(1000[Ca]_{i2})}$	$1.7\exp[-(Vm+152)/30]$ $Vm = v + 40\log(1000[Ca]_{i2})$
I_{CaL}	0.0004	0.0004	$p = 2$	$\frac{15.69(81.5-v)}{\exp[(81.5-v)/10] - 1}$	$0.29\exp[-v/10.86]$
I_{CaN}	0.0005	0.0005	$p = 2$ $q = 1$	$\frac{0.19(19.98-v)}{\exp[(19.98-v)/10] - 1}$ $0.00016\exp[-v/48.4]$	$0.046\exp[-v/20.73]$ $\frac{1}{\exp[(39-v)/10] + 1}$
I_{CaT}	0.0005	0.0005	$p = 2$ $q = 1$	$\frac{0.19(19.98-v)}{\exp[(19.98-v)/10] - 1}$ $0.00016\exp[-v/48.4]$	$0.046\exp[-v/20.73]$ $\frac{1}{\exp[(39-v)/10] + 1}$
I_{AHP}	0.00005	0.00005	$p = 1$	$\frac{0.0048}{\exp[-0.5(Vm-35)]}$ $Vm = 10\log(1000[Ca]_{i1})$	$\frac{0.012}{\exp[0.2(Vm+100)]}$ $Vm = 10\log(1000[Ca]_{i1})$
I_{KA}	0.005	—	$p = 1$ $q = 1$	$\frac{-0.05(v+25)}{\exp[(v+25)/-15] - 1}$ 0.00015	$\frac{0.1(v+15)}{\exp[(v+15)/8] - 1}$ 0.06
Diam. (μm)	16	3	$C_m = 1.0$	$R_{axial} = 210 \Omega\text{-cm}$	$G_{leak} = 0.0002$
Length (μm)	16.8	150	$E_{Na} = 45 \text{ mV}$	$E_K = -85 \text{ mV}$	$E_{leak} = -70 \text{ mV}$
$\tau_{[Ca^{2+}]}$ (sAHP)(msec)	1000	1000	$[Ca^{2+}]_{rest} = 50 \text{ nM}$	$x_{\infty} = \frac{\alpha}{\alpha + \beta}$	$\tau_x \text{ (ms)} = \frac{1}{\alpha + \beta}$
$\tau_2[Ca^{2+}]$ (C)(msec)	1	1			

Table A3: Parameter values for BC and OLM cells (*all values for are for both unless otherwise indicated*).

Current	Soma G_{\max} (S/cm2)	Dend _p G_{\max} (S/cm2)	Gat. Var.	α	β
I_{Na}	BC-0.12; OLM-0.08	BC-0.12; OLM-0.08	$p = 3$ $q = 1$	$\frac{-0.3(v - 43)}{\exp[(v - 43)/-5] - 1}$ 0.23	$\frac{0.3(v - 15)}{\exp[(v - 15)/5] - 1}$ 3.33
I_{fKdr}	BC-0.0013; OLM-0.01	BC-0.0013; OLM- 0.01	$p = 4$	$\frac{\exp[(v - 65)/20]}{-0.07(v - 47)}$ $\exp[(v - 47)/-6] - 1$	$\frac{\exp[(v - 12.5)/-10] + 1}{0.264}$ $\exp[(v - 22)/40]$
I_{sKdr}	BC-0.0013; OLM-0.01	BC-0.0013; OLM- 0.01	$p = 4$	$\frac{-0.028(v - 35)}{\exp[(v - 35)/-6] - 1}$ 0.28[Ca ²⁺]	$\frac{0.1056}{\exp[(v - 10)/40]}$ 0.48
I_{KCa} (BC)	0.0002	0.0002	$p = 1$	$\frac{[Ca^{2+}] + \exp1(0.00048, 0.84, v)}{0.12Fv}$ exp1 = 0.00048exp[- $\frac{1}{R[273.15 + degC]}$]	$\frac{1 + [Ca^{2+}]/\exp1(0.13e^{-6}, 1, v)}{Fv}$ exp1 = 0.13e ⁻⁶ exp[- $\frac{1}{R[273.15 + degC]}$]
I_H (OLM)	0.00002	0.00002	$p = 1$	$X_{\infty} = \frac{1}{\exp[(84.1 - v)/10.2] + 1}$ 15.69(81.5 - v)	τ_x (ms) = $\frac{1}{\exp[0.116v - 17.9] + \exp[0.09v - 1.84]}$
I_{CaL}	0.09	0.09	$p = 2$	$\frac{\exp[(81.5 - v)/10] - 1}{0.19(19.98 - v)}$	0.29exp[-v/10.86]
I_{CaN} (BC)	0.0008	0.0008	$p = 2$ $q = 1$	$\frac{\exp[(19.98 - v)/10] - 1}{0.00016\exp[-v/48.4]}$	0.046exp[-v/20.73]
I_{CaT} (OLM)	0.0005	0.0005	$p = 2$ $q = 1$	$\frac{0.2(19.26 - v)}{\exp[(19.26 - v)/10] - 1}$ 0.00016exp[-v/16.26]	$\frac{1}{\exp[(39 - v)/10] + 1}$ 0.009exp[-v/22.03]
I_{KAHP}	0.00002	0.00002	$p = 1$	$1.25 * 10^{13} [Ca^{2+}]^4$	$\frac{1}{0.00025}$ exp[(29.79 - v)/10] + 1
I_A	BC-0.00015; OLM-0.0001	BC-0.00015; OLM- 0.0001	$p = 1$ $q = 1$	0.02exp[(1.8(v + 33.6) · $\frac{F}{RT}$)] 0.08exp[(4(v + 83) · $\frac{F}{RT}$)]	0.02exp[(-1.2(v + 33.6) · $\frac{F}{RT}$)] 0.08
Diam. (μm)	BC-15; OLM- 10	BC-2.5; OLM-3	$C_m =$ BC-2.5; OLM-2.0	$R_{axial} =$ BC-100; OLM-150 Ω-cm	$G_{leak} =$ BC-0.0002; OLM-0.0003
Length(μm)	20	BC-300; OLM-250	$E_{Na} =$ 55 mV	$E_K =$ -90 mV $X_{\infty} = \frac{\alpha}{\alpha + \beta}$	$E_{leak} =$ -64 (BC); -60 (OLM) mV τ_x (ms) = $\frac{1}{\alpha + \beta}$

Figure Titles

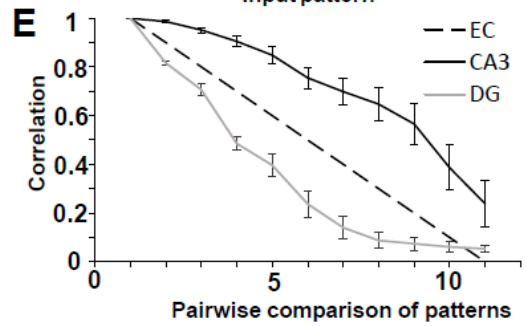
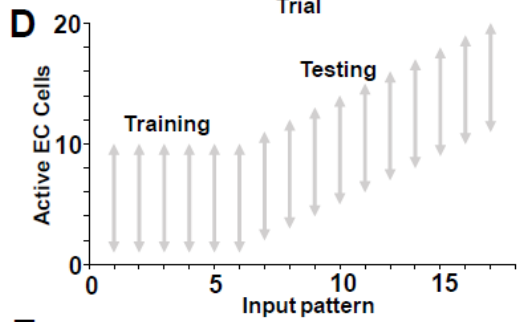
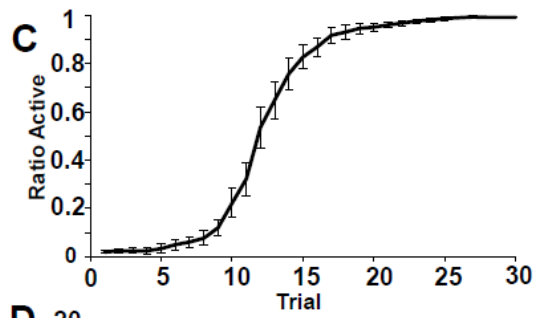
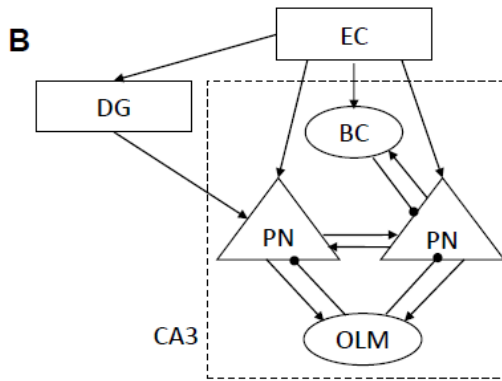
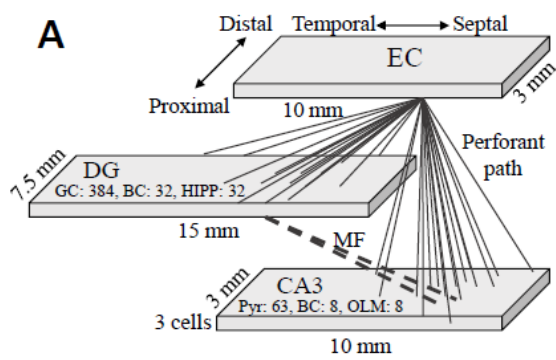
Figure 1. Structure and characterization of the 3D hippocampal network. (A) Schematic of the network showing the modeled regions EC, CA3, and DG with their dimensions, cell numbers, and longitudinally organized connectivity patterns (Hummos et al. 2014). Neurons in EC were more likely to send connections to DG and CA3 neurons in their longitudinal vicinity. Similarly, DG granule cells tended to project to CA3 neurons in the same lamella. Cells were compacted into three sheets, in the radial dimension, representing stratum-pyramidale in CA3 and the granular layer in DG. (B) Schematic of internal circuitry within CA3. Excitatory connections terminate in arrows and inhibitory ones in black filled circles. (C) Activity in CA3 with increasing numbers of EC afferents, without inhibitory interneurons and short-term depression at the CA3 recurrent connections. Uncontrolled spread of excitation among CA3 PNs can be noticed when the number of EC inputs exceeds 10. Accordingly, we chose 10 as input size of EC afferents to the CA3-DG network. (D) EC cells activated during each the training protocol. The ‘training’ phase consisted of five presentations of EC pattern 1 to the network, followed by a ‘retrieval’ phase where 11 patterns of EC inputs were presented with decreasing levels of similarity to the encoded pattern 1. (E) Correlation of output patterns in EC, CA3 and DG during the retrieval phase, in response to the probe patterns 1-11 from EC. The correlation between input pattern 1 and the probe EC patterns is shown as a reference point. Correlation values at CA3 pyramidal neurons lie well above the input correlation indicating a tendency towards pattern completion in CA3. Conversely, DG correlation values lie below input correlation levels indicating pattern separation. This provides validation that the network performs pattern completion and separation as expected.

Figure 2. Morphology of inhibitory connections in the CA3 network. BCs make perisomatic synapses onto CA3 cells, have arborized axons, and also project to neighboring OLM cells. In contrast, OLM cells synapse distally onto dendrites. The CA3 pyramidal cell receives excitatory input from EC cells, and mossy fiber (MF) inputs from DG cells. DG cells also provide excitatory inputs to BCs. BCs inhibit OLM cells, but this projection is not reciprocated.

Figure 3. Distinctive features of inhibition by BCs and OLM cells. (A) Average firing rate distributions of BC (blue) and OLM (orange) cells. BCs had a significantly larger dynamic range in firing rate compared to OLM cells. (B) Dependence of firing rate of BCs (blue) and cells OLM (orange) on the number of CA3* afferents. The former received afferents from EC and DG* but the latter did not. (C) Grouping BC firing rate by number of EC afferents revealed a linear trend in BC firing rates with the total number of CA3*+DG* afferents. (D) Inactivation of BCs resulted in significantly more ($p < 0.05$) CA3* cells with higher EC afferents added to the pattern, as compared to inactivation of OLM cells.

Figure 4. Comparison of effects of back-projection from CA3 to DG. Normal correlation for CA3 (red) and DG (blue) is shown in solid, and correlation with back-projection using disynaptic inhibition in dashed lines. This CA3-DG back-projection resulted in both increased pattern completion in CA3 (17% change in area under the curve;

$p < 0.005$), and increased pattern separation in DG (23% change in area under the curve; $p < 0.005$).



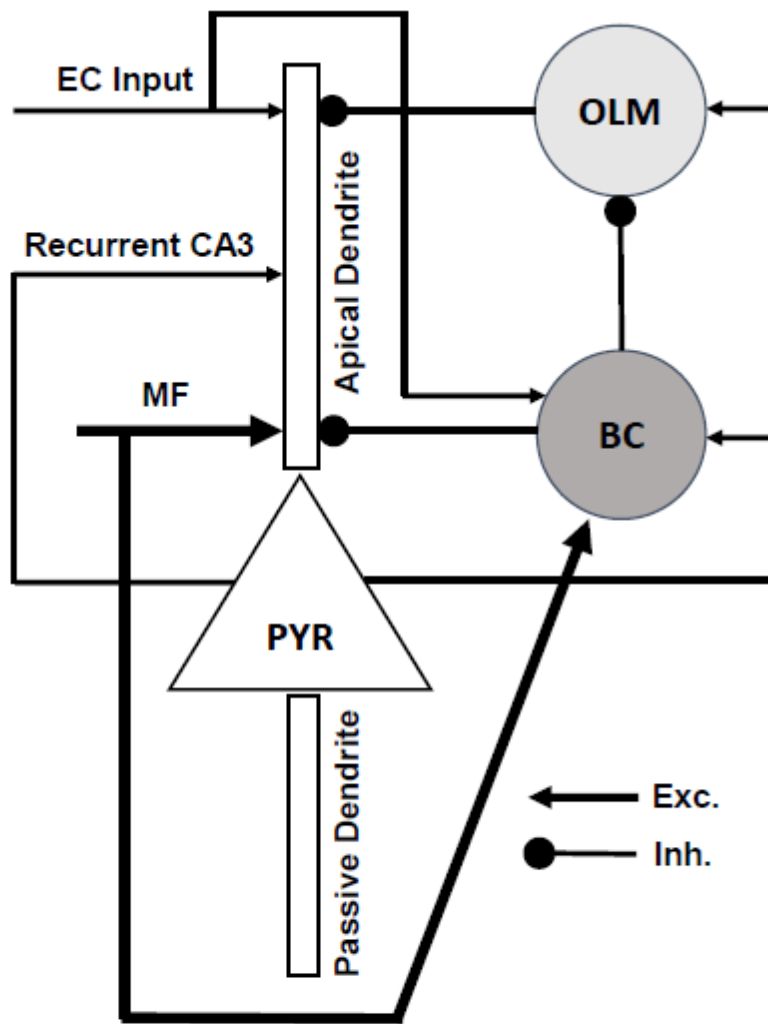


Figure 2

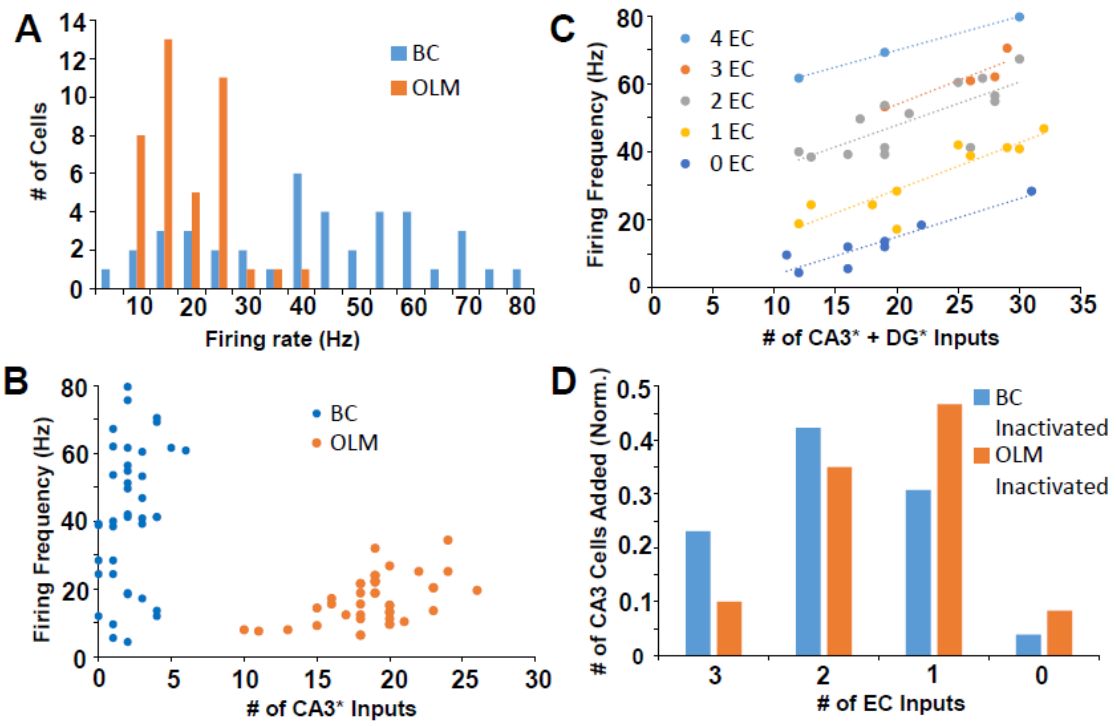


Figure 3

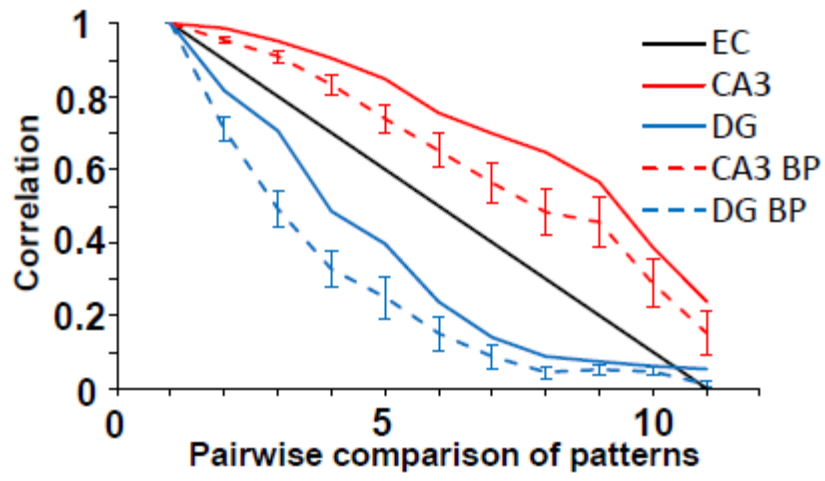


Figure 4

CHAPTER 4

GENESIS OF HIPPOCAMPAL THETA RHYTHM IN A COMPUTATIONAL MODEL

ABSTRACT

The mechanisms involved in the generation of hippocampal theta remain poorly understood. We studied the underlying mechanisms in the genesis of theta by adapting a computational network model of the rodent hippocampus. The model had biologically realistic conductance-based single cells models for principal cells and the two abundant interneuron types in CA3 and dentate gyrus (DG) regions. The interneuron types were, basket cells (BCs) and oriens lacunosum-moleculare (OLM) interneurons, and the present study incorporated realistic gap junction and chemical synapse connectivity among and between these interneurons. The network model also included synaptic current dynamics, spatial connectivity patterns, short-term synaptic plasticity, and known effects of acetylcholine. Work to be completed - Improve the model to include accurate LFP type theta detection rather than using population firing rate; Study in-depth the uncovered mechanisms; and investigate theta-gamma coupling.

INTRODUCTION

Hippocampal theta frequency (4-12 Hz) oscillations are consistently recorded during working memory tasks, spatial navigation, and storage of episodic memory (for review, see Buzsáki, 2002; Colgin, 2013). During *in vitro* isolation, the hippocampus can generate its own theta rhythm (Goutagny et al., 2009), and several potential intrinsic mechanisms of hippocampal theta rhythm generation have been identified (for review,

see Buzsáki, 2002; Colgin, 2013). However, *in vivo* hippocampal theta is attenuated by disruption of input from the medial septum (Petsche et al., 1962; Brazhnik and Vinogradova, 1986; Stewart and Fox, 1990; Vinogradova, 1995; Boyce et al., 2016) and from the entorhinal cortex (EC, Alonso and García-Austt, 1987), which raises questions about the capability of intrinsic hippocampal theta mechanism to provide robust and sufficient theta rhythm generation. Further, even though multiple potential sources of intrinsic hippocampal theta rhythm generation have been identified, no single intrinsic mechanism has been shown to be sufficient for generation of theta rhythms *in vivo*, and there is currently a lack of understanding of which intrinsic mechanisms are involved in particular hippocampal system states. Here we study model intrinsic hippocampal theta mechanisms to understand their respective state-dependent roles in generating theta rhythms.

While computational models have previously identified multiple potential individual theta mechanisms, experiments aimed at confirming these mechanisms individually continue to reveal conditions where these intrinsic mechanisms are not involved in generation of hippocampal theta rhythms. For example, the slow firing oriens-lacunosum moleculare (OLM) cells exhibit behavior close to theta rhythm *in vivo* (Klausberger et al., 2003), and computational models have therefore proposed OLM cells as intrinsic generators of the theta rhythm (Gloveli et al., 2005; Rotstein et al., 2005; Neymotin et al., 2013). However, subsequent biological experiments have shown that OLM cells exhibit modest resonance at the theta frequency (Kispersky et al., 2012), and silencing OLM cells *in vivo* did not diminish hippocampal theta activity (Royer et al., 2012). As a second example, intrinsic membrane conductances have been suggested as

contributing to generation of hippocampal theta rhythm using computational models, such as the spike-frequency adaptation currents (Crook et al., 1998; Fuhrmann et al., 2002; Hu et al., 2002; Gigante et al., 2007; Augustin et al., 2013), or the h-current (Orbán et al., 2006; Zemankovics et al., 2010; Neymotin et al., 2013). It is difficult to study spike-frequency adaptation currents experimentally, but a genetic knockout of the h-current did not disrupt hippocampal theta rhythm (Nolan et al., 2004; Giocomo et al., 2011). Recurrent excitatory connections between pyramidal cells is a third mechanism proposed by computational models (Traub et al., 1989, 1992; Hansel et al., 1995; Crook et al., 1998; Fuhrmann et al., 2002; Netoff et al., 2005); but biological experiments again revealed occurrence of hippocampal theta oscillations even where excitatory AMPA transmission at the recurrent excitatory connections between pyramidal cells is disrupted (Gillies et al., 2002). In addition, a fourth proposed intrinsic mechanism for generation of hippocampal theta rhythm from is the divergence of afferent projections to an area, which has been suggested in computational models (Teramae and Tanaka, 2004; Nakao et al., 2005; Springer and Paulsson, 2006) and in experiments involving the olfactory cortex (Galán et al., 2006). However, the role of these divergent projections in generating hippocampal theta rhythms has not been explored.

We used a biophysical computational model of the hippocampus that included principal cells and two types of interneurons (Basket Cells (BCs) and OLM cells), to investigate how the various intrinsic theta mechanisms might be integrated, and to examine their relative contributions to the hippocampal theta rhythm generation. The model included neuromodulatory inputs, spatially realistic connectivity between model cells, and short-term synaptic plasticity, which were all constrained by prior experimental

observations. We examined the intrinsic hippocampal theta generation mechanisms independently of external rhythmic input, by removing the well-studied medial septal input (Denham and Borisyuk, 2000) and suppressing any rhythmicity in EC (Alonso and García-Austt, 1987). We found five intrinsic mechanisms that contributed differentially to hippocampal theta rhythm generation. Importantly, no one intrinsic mechanism was critical to generating the theta rhythm, which is consistent with experimental results. These model findings suggest that intrinsic hippocampal theta generation is robust and sufficient. We found that even with random Poisson activity, EC input was very important for theta rhythm generation. Notably, EC input had the largest relative contribution to theta power, followed by the recurrent connections and OLM cells. This is consistent with the significant drop in theta power following removal of medial septum external inputs (Vinogradova, 1995) or EC inputs (Alonso and García-Austt, 1987) to the hippocampus *in vivo*. Finally, we also found that the low and the high cholinergic states used distinct intrinsic mechanisms for theta rhythm generation, which allowed us to examine which network parameters foster the engagement of specific intrinsic mechanisms during different cholinergic network states.

METHODS

We developed a network model of the rodent hippocampus in a prior study using Izhikevich single cell models, synaptic currents, spatial connectivity patterns, short- and long-term plasticity and known neuromodulator effects (Hummos et al. 2014). The model included CA3 and DG regions that received inputs from EC. The present study used the same model, except for replacing the Izhikevich single cell models with biophysical

conductance-based models matched to biological data. We provide information related to the single cell models below, followed by an overview of the overall model. The reader is referred to our previous study for detailed descriptions including parameters related to other model features (Hummos et al. 2014). The model, developed using the package NEURON (Carnevale and Hines 2006), will be made available upon publication via the public database ModelDB (<http://senselab.med.yale.edu/ModelDB/>).

Single Cell models

Single neurons were modeled using the Hodgkin-Huxley formulation (Byrne et al. 2014) and included multiple compartments known currents and neuromodulator receptors. CA3 model cells PNs and the two most abundant interneuron types, BCs and OLM cells (Vida, 2010). DG model cells included granule cells, BCs, and Hilar Perforant Path-associated (HIPP) cells. All model neurons were matched to the salient features reported in biology: CA3 PNs fire in bursts of 2-3 action potentials as well as individual spikes (Tropp Sneider et al. 2006). These PNs respond to current injections with an initial burst followed by either silence or tonic firing of different frequencies (Brown and Randall 2009; Hemond et al. 2008) and are also capable of bursting in response to a very short (2-5ms) current pulse with a burst of action potentials that outlive the stimulus (Brown and Randall 2009; Wong and Prince 1981). Granule cells in DG display a very low basal firing rate in vivo with an average < 0.5 Hz, and bursts shorter than those in CA3 cells (Jung and McNaughton 1993). These cells predominantly fire in single spikes with spike frequency adaptation (Staley et al. 1992). We used a resting membrane potential of -73 mV (Staley et al. 1992) and matched biological membrane potential

responses to current injection (Staley et al. 1992). Parvalbumin-positive basket cells are characterized by fast spiking patterns and a small membrane time constant (~10 ms) and little spike frequency adaptation (Bartos and Elgueta 2012). The cell model had these characteristics, with a resting potential of -64 mv and firing rate vs current injection relationship that matched data in (Buhl et al. 1996). OLM cells have a high input resistance (496 M Ω) and slow membrane time constant (71 ms) (Lawrence et al. 2006). Action potentials are followed by a characteristic long-lasting, slow after-hyperpolarization with rebound spikes occurring commonly on repolarization. Model OLM cells captured these characteristics, and had a resting membrane potential of -68 mv (Ali and Thomson 1998). OLM model cells were also tuned to produce the observed slow AHP, rebound spikes and the characteristic sag with negative current injections. Appendix tables 1A-1C provide a complete listing of the parameters for the four single cell models described above.

Network structure and connectivity

Typical of most models, the network model was a scaled down version of the rat hippocampus (Hummos et al. 2014; Li et al. 2011). The CA3 region contained 63 pyramidal cells, and 8 BCs and 8 OLM cells, while the DG region had 384 granule cells, 32 BCs and 32 HIPP cells. The number of cells in each region was selected keeping the ratio between population cell numbers as close to biology as possible. Perforant path projections from EC follow a lamellar organization across a longitudinal axis of the hippocampus (Naber et al. 1997; Witter 2010), and projections from DG to CA3 follow a similar longitudinal organization (Hummos et al. 2014).

Model cells in CA3, DG and EC were distributed in three dimensions, which correspond to respective dimensions of the rat hippocampus. Projections from EC to pyramidal cells and BCs in DG and CA3 were most likely to project to neurons in the center of their longitudinal neighborhood, using a Gaussian connection probability function that depended on the longitudinal distance between cells. The Gaussian function had a peak probability value of 0.4 for projections from EC to pyramidal cells and BCs in CA3 (Fig. 1). EC projections to DG had similar values. Mossy fiber projections from DG to CA3 followed a similar lamellar pattern as of EC to CA3 and EC to DG projections (Fig. 1). Each DG granule cell connected to a maximum of two CA3 pyramidal neurons (Rolls and Kesner, 2006), in order to create sparse MF connections. Previous studies have determined that projections from DG granule cells to CA3 BCs out-number projections to CA3 pyramidal neurons by a ratio of 10:1 (Acsady et al., 1998). Accordingly, DG projections to BCs followed a Gaussian distribution with a higher peak probability and standard deviation than projections from DG to CA3 PNs (Fig. 1). Recurrent connections between CA3 PNs were generated with a fixed probability of 0.3, since these recurrenents generally reveal no spatial organization (Wittner et al. 2007).

OLM cells make many more synapses compared to BCs (Sik et al. 1995), but have limited axonal arborization, and are believed to participate in feedback inhibitory loops (Maccaferri 2005). BCs have a more diffuse axonal arborization with higher likelihoods of connecting to pyramidal cells in the vicinity of the BCs (Sik et al. 1995). BCs also provide inhibitory connections to neighboring OLM cells (Bartos et al. 2010), but OLM cells do not project to BC cells. A Gaussian function was used to determine these connectivities (Fig. 1). BC projections to pyramidal cells and to OLM cells shared

the same spatial domain, while OLMs received reciprocal connections from the pyramidal cells they projected to (Maccaferri 2005). Principal cells in both DG and CA3 projected to BCs with a fixed probability of 0.15, based on the lack of specific topography for these projections (Wittner et al. 2007). CA3 back-projections inhibit DG granule cells through a direct pathway (Ishizuka et al. 1990; Li et al. 1994; Scharfman 1994) and indirectly by exciting hilar mossy cells (Scharfman 2007; 1994) and also DG interneurons with dendrites in the hilus (Kneisler and Dingledine 1995; Scharfman 1994)

Connections between cells were generated randomly, based on the probabilities described above, and experimental data was used to match spontaneous firing rates of pyramidal cells in CA3 (Mizuseki et al. 2012) and granule cells in DG (Bower and Buckmaster 2008).

Synaptic currents

The synaptic AMPA, NMDA, GABA_A, and GABA_B currents were modeled based on (Destexhe et al. 1998) and their dynamics were matched to available literature. AMPA currents in CA3 PNs were fastest for inputs from DG and slowest for inputs from EC, while inputs from other CA3 cells had intermediate values (Hoskison et al. 2004; Tóth 2010). Additionally, BC inhibitory currents had faster dynamics than those from OLM (Bartos et al. 2010). Synaptic weights were assigned based on available literature. The synapses from DG to CA3 were selected so multiple inputs to a CA3 cell would cause the CA3 cell to spike, while a single synaptic input would not (Henze et al. 2002). Recurrent CA3 synapses used a low initial synaptic weight, based on biological data indicating low transmission probability of action potentials (4%) at the recurrent CA3 synapses (Miles and Wong

1983). CA3 pyramidal cell to BC and OLM interneurons used a higher synaptic level based on biological data indicating a higher transmission probability of action potentials (~60%) (Gulyas et al. 1993; Miles 1990). In the DG region, synapses between DG granule cells and DG interneurons were selected to provide sparse DG firing (Bower and Buckmaster 2008).

Long-term synaptic plasticity

Biological studies have shown classical Hebbian associative long-term potentiation (LTP) at the glutamatergic perforant path synapses to DG (Bliss and Gardner-Medwin 1973) and to CA3 (Do et al. 2002). Many types of synaptic plasticity exist at GABAergic synapses (for a review, see (Maffei 2011)). (Woodin et al. 2003) reported LTP between hippocampal cells if the pre- and post-synaptic spikes were within 20ms of each other, LTD if within 50ms, and no change if longer. They also found plasticity to be dependent on activation of postsynaptic L-type voltage dependent calcium channels (VDCCs).

Consistent with these findings, the model implemented LTP using a learning rule based on the concentration of a post-synaptic calcium pool at each modifiable synapse (Shouval et al. 2002a). At excitatory synapses, calcium entered post-synaptic pools via NMDA receptors, and at inhibitory synapses, calcium entered through VDCCs. The postsynaptic pool also received Ca^{2+} from internal stores upon GABA_B receptor stimulation. This approach has been used in other models by our group (Kim et al. 2013b; Li et al. 2009). For both types of synapses, a calcium concentration above a lower threshold caused synaptic weight depression, while a concentration exceeding an upper

threshold cause synaptic weight potentiation. Because the characteristics of DG to CA3 mossy fiber potentiation are controversial (Neves et al. 2008), we only modeled short-term plasticity in the MF connections, as described below. Long-term plasticity in all synapses was constrained to 100%.

Short-term synaptic plasticity

In addition to long-term plasticity described above, we included short-term plasticity in the model based on the formulation by (Varela et al. 1997). We modeled short-term facilitation reported at the DG to CA3 mossy fiber connections (Toth et al., 2000) and frequency-dependent synaptic depression reported at the recurrent CA3 connections (Hoskison et al. 2004). In CA1, projections from pyramidal cells to OLM cells have been shown to experience short-term facilitation (Ali and Thomson 1998), while projections to BC cells experience short-term depression (Ali et al. 1998). In the opposite direction, inhibitory currents from OLM cells to CA3 pyramidal cells show no short term facilitation or depression (Maccaferri 2005), while inhibitory currents from BC cells to CA3 pyramidal cells show depression (Hefft and Jonas 2005).

Acetylcholine effects

The hippocampus receives cholinergic inputs from the septum-diagonal band complex (Woolf 1991). To implement the effects of ACh in our model on cells and synaptic connections, a variable ‘ACh’ was used to represent discrete ACh levels of 0 (low), 1 (baseline), and 2 (high). Under cholinergic stimulation, synaptic transmission from EC to CA3 is suppressed by 50%, and is suppressed by 85% at the recurrent

connections in CA3 (Barry et al. 2012; Hasselmo et al. 1995; Kremin and Hasselmo 2007). In contrast, DG to CA3 synaptic transmission is enhanced by 49% under cholinergic stimulation (Vogt and Regehr 2001). We did not modify inhibitory synaptic connections in the model based on ACh levels. AMPA synaptic currents were scaled by the value of ACh in our model to represent ACh effects on the synapses. A parameter bACh was used to determine the direction and magnitude of ACh effects on a particular synapse. Values of bACh for different synapses were set according to experimental results. In addition to the synaptic effects described above, cholinergic stimulation also enhanced cellular excitability, depolarized the resting membrane potential of principal cells, eliminated AHP, decreased spike frequency adaptation and induced rhythmic burst activity (Bianchi and Wong 1994; Misgeld et al. 1989). Effects on BC and OLM interneurons were subtype-dependent (McQuiston and Madison 1999a; McQuiston and Madison 1999b). Muscarinic stimulation of OLM interneurons depolarized the resting membrane potential, and also lowered spike frequency adaptation and AHP (Lawrence et al. 2006). In contrast, BC cells have low levels of nicotinic ACh receptors, and they respond to muscarinic receptor activation with a limited resting membrane potential depolarization (Cea-del Rio et al. 2010; Cobb and Lawrence 2010). We modeled effects of ACh on neurons by linearly scaling cell parameters by the ACh level (see Hummos et al., 2014).

Inputs and data analysis

For the full model and sub-circuit cases considered, appropriate model cells (identified in the figures) received external input as trains of Poisson-distributed spikes

that arrived at a dedicated synapse associated with each cell, triggering an influx of AMPA and NMDA currents into the cell. To limit the focus of this study to intrinsic hippocampal theta mechanisms, we chose to exclude input from medial septum which is known to generate theta in CA3 (Vinogradova, 1995). We studied two model cases: one with external input arriving at EC, and the other with input arriving directly at CA3 pyramidal cells. The two types of inputs differed in the weight of the associated input synapses, and the base rate of the Poisson spike trains arriving at these synapses. Input to EC arrived at synapses with a 100% spike transmission rate to ensure that EC firing pattern was dictated by the Poisson input, whereas input to CA3 pyramidal cells had a lower weight value with parameters matching the EC to CA3 synapses (Table 1).

To determine the base rates of the Poisson processes generating these input trains, we considered place cells in CA3. Place cells respond to certain areas in the environment and their firing rates approximate a lognormal distribution (Mizuseki and Buzsáki, 2013) with an average of ~7 Hz (Mizuseki et al., 2012). In our model case where external inputs arrived to EC, each EC cell received a unique train of Poisson input spikes at a base rate of 15 Hz, which produced firing rates in CA3 pyramidal cells with a lognormal distribution and an average of 7 Hz (Fig. 2C1). In the model case where external inputs arrived directly to CA3 pyramidal cells, the input rates to different cells had to be drawn from a lognormal distribution (average: 50 Hz, standard deviation: 40 Hz), to produce firing rates with a lognormal distribution (Fig. 2C2) that matched experimental data.

For spectral analysis, we summed the spikes of all cells of each type in a region (e.g., CA3 pyramidal cells) in 0.1 ms bins and computed the fast-Fourier transform of the resulting vector, using the Matlab function `psautospk.m` (Koch and Segev, 1998), with a

moving window of size 1024 ms, and overlap of 512 ms. Spike data was used in spectral calculations as a proxy for LFP as used in network models (e.g., Brunel and Wang, 2003; Hoseini and Wessel, 2016; Samarth et al., 2016).

The model was developed using the NEURON software package (Carnevale and Hines, 2009) and run on a PC with an Intel i7-core processor with an integration time-step of 0.1 ms (key results were also verified with a time-step of 0.01 ms). The code is available as part of our previous publication via the public database ModelDB at Yale University. The recorded spike times were then analyzed using MATLAB (Mathworks, Inc.). All simulations ran for 3 seconds except for the experiment in figure 4, where single neuron spike data was analyzed over a 30 second period.

Model tuning and validation

The overall model was developed in stages: the single cell models, the properties of glutamatergic and GABAergic synapses, the intrinsic connections between cells, plasticity in appropriate connections, and, finally, neuromodulator effects. The following approach was used for modeling each of the above: (1) The experimental literature was mined, both to constrain the model and derive criteria to assess whether the model successfully reproduced the particular phenomena being modeled; (2) Iterative “tuning” of model parameters was performed until the model’s behavior matched experimental observations; and (3) Validation of the model, which took two forms. First, the ability of the model to reproduce the experimental data considered in its development. Second, the ability of the model to reproduce a set of experimental observations it was not designed to reproduce. The tuning and validation procedure used are described next.

Model Tuning: To further constrain the model and assess its functional capacity, we tuned it to perform pattern separation and pattern completion. The additional tuning required was mainly to adjust connection weights and LTP thresholds (Tables S4 and S5), to ensure practical neuron activity levels and synaptic learning rates.

Following Hasselmo et al. (1995), we ran the network through an encoding phase under high levels of ACh ($= 2$). In this encoding phase, an input pattern was constructed to consist of 10 randomly selected EC neurons (pattern 1), and the network was then presented with this input pattern for five 500 ms trials. 10 input cells were selected to study 10 different levels of input similarity, although other values would work for other experiment designs. For each trial, EC neurons in the pattern received inputs for 250 ms at 12 Hz. Five trials were selected to stay as close as possible to some fear conditioning studies that used five conditioning trials. After five learning trials the model had a sufficient learning accuracy of recall, similar to experiments with rodents that select a cut off above a certain percentage where the rodent is considered to have learned the behavior in question.

After the encoding phase, we tested for retrieval in response to 10 input patterns that had decreasing amounts of overlap with the encoded pattern 1. The 10 probe patterns, numbered 2 to 11, were constructed as follows. Pattern 2 contained nine of the neurons in pattern 1 and an additional neuron selected randomly. Similarly, pattern 3 shared eight neurons with pattern 1 and included two other neurons selected randomly. With this logic, Pattern 11 had no neurons in common with pattern 1. See Figure 1D. To test for retrieval, all long-term plasticity was inactivated and we examined the output retrieved in response to probe patterns 2 to 11 under the lowered (retrieval) level of ACh ($= 0$).

In each retrieval trial, one of the eleven patterns was presented at EC, and the number of spikes each neuron fired during the trial was recorded. Subsequently, to form a trial “output” pattern for each area, the spike counts from all its principal cells were populated into a vector that was normalized to a length of one. The correlation between the outputs of any two trials was then assessed by taking the dot product of the two corresponding output vectors. This correlation measure has a minimum value of 0 indicating that the two output patterns being compared had a non-overlapping set of neurons firing in each. Conversely, a correlation level maximum value of 1 indicates that the two vectors had the same set of neurons firing at the same rates.

For each area in the model, we calculated pair-wise correlation comparisons between the output from pattern 1 and the output from each of the patterns from 1 to 11. Figure 1E shows these pair-wise correlation values for EC, CA3 and DG. Inputs arrived directly at EC neurons, thus, EC correlation levels reflect the similarity between input patterns. Correlation between CA3 output patterns were above EC correlation (Fig. 1E), indicating that CA3 was engaged in retrieval of stored patterns. For instance, input pattern 3 had a correlation of 0.8 with input pattern 1, whereas in CA3, the output from pattern 3 had a correlation of 0.95 with pattern 1, indicating that even for dissimilar inputs CA3 retrieved output that are more similar to the learned pattern 1. Thus, even with changes in the sensory input, CA3 may still retrieve a previously learned memory pattern. On the other hand, DG outputs revealed lower correlation relative to inputs, indicating that DG was predisposed to create distinct neuronal representations (Fig. 1E).

These results are consistent with computational theories of the division of labor between DG and CA3 (Treves and Rolls, 1992; O’Reilly and McClelland, 1994; Hasselmo

et al., 1995; McClelland and Goddard, 1996) and recent experimental evidence (Lee and Kesner, 2004; Leutgeb et al., 2007; Bakker et al., 2008; Neunuebel and Knierim, 2014).

Model validation: Cholinergic transmission has been implicated in the modulation of activity in CA3 with high ACh favoring pattern separation and low ACh levels favoring pattern completion (Hasselmo et al., 1995; Rogers and Kesner, 2003; Meeter et al., 2004). Accordingly, to validate the model, we examined the effects of different levels on ACh on the dynamics during retrieval, and compared the results to reports in the literature. Averaged results from 10 random initializations of the network demonstrated that CA3 outputs in response to probe patterns 1-11 had significantly lower correlation levels to the encoded pattern 1 under high levels of ACh compared to low ACh levels, while DG correlation levels remained unchanged (not shown). These observations are in agreement with previous models (Hasselmo et al., 1995; Meeter et al., 2004; for review, see Newman et al., 2012) and experimental results (Ikonen et al., 2002; Rogers and Kesner, 2003, 2004).

Limitations: Synapses from DG granule cells to CA3 parvalbumin-BCs exhibit short-term synaptic facilitation (Szabadics and Soltesz, 2009). However, inputs from MF to other types of interneurons such as Cholecystinin-BC exhibit short-term depression. Therefore, we assumed that the combined input from DG to both populations of BC cells would then effectively have no short-term dynamics. Accordingly, the MF synapses to BCs in the present model did not have any short-term plasticity.

Comparison to reduced-order model: Hummos et al. (2014) showed how nonlinear mechanisms such as depressing synapses at recurrent CA3 collaterals and inhibition by OLM interneurons were suited to prevent runaway excitation whereas inhibition by BC interneurons might be inefficient. Their model also showed how these intrinsic

mechanisms stabilized encoding and retrieval phases differentially. The present study uses a more realistic single cell model with individual channel currents and neuromodulation receptors to extend the study and investigate pattern completion and separation processes at the synaptic level. All reported values below are mean \pm s.e.m., unless stated otherwise.

RESULTS

Issues to consider from previous study: Poisson spikes input generates theta oscillations in the model – cause for these ‘spurious’ oscillations; Pyramidal cells display theta stochastic resonance; Divergent projections produce theta oscillations; Short-term plasticity stabilizes theta oscillations in recurrent networks; Pyramidal-Interneuron sub-networks generate theta through two mechanisms; Theta mechanisms have different relative contributions across cholinergic states.

New issues to consider: Add connections among and between BCs and OLMs – something not presently in the model. Then use the model to study the following: (i) Role of I_h in theta rhythm – when I_h is added; disconnected cells show two power peaks in theta and beta range, but when connected the beta peak disappears. Also, interaction of ACh on individual currents? (ii) Different ways to quantify, interpret and detect theta? (iii) More deeper or thorough investigation of mechanisms proposed by previous study; (iv) CA3 pyr cells spike randomly and it was observed that even disconnected cells show theta resonance because of spurious correlations and the mechanisms proposed only help synchronize more these spurious correlations; (v) The 3-compartment bio-realistic cells we will use to replace the 1-compartment Izhikevich cells should give us the opportunity to accurately place BC and OLM inhibition and provide more insight into these

differential inhibitory circuits; (vi) Theta rhythms are usually measured biologically using LFPs. May be move to more accurate LFP model to detect theta in the network is needed than use of population firing rates; (vii) Analysis of synchrony on complete CA3 network.; (viii) Investigate more on the role of DG inputs on CA3.

REFERENCES

Acsady L, Kamondi A, Sik A, Freund T, Buzsaki G (1998) GABAergic cells are the major postsynaptic targets of mossy fibers in the rat hippocampus. *J Neurosci* 18:3386–3403.

Ali AB, Deuchars J, Pawelzik H, Thomson AM (1998) CA1 pyramidal to basket and bistratified cell EPSPs: dual intracellular recordings in rat hippocampal slices. *J Physiol* 507:201–217.

Ali AB, Thomson AM (1998) Facilitating pyramid to horizontal oriens-alveus interneurone inputs: dual intracellular recordings in slices of rat hippocampus. *J Physiol* 507:185–199.

Alonso A, García-Austt E (1987) Neuronal sources of theta rhythm in the entorhinal cortex of the rat. II. Phase relations between unit discharges and theta field potentials. *Exp Brain Res* 67:502–509.

Asghar AUR, Corte PFCL, LeBeau FEN, Dawoud MA, Reilly SC, Buhl EH, Whittington MA, King AE (2005) Oscillatory activity within rat substantia gelatinosa in vitro: a role for chemical and electrical neurotransmission. *J Physiol* 562:183–198.

Barkai E, Bergman RE, Horwitz G, Hasselmo ME (1994) Modulation of associative memory function in a biophysical simulation of rat piriform cortex. *J Neurophysiol* 72:659–677.

- Barry C, Heys JG, Hasselmo ME (2012) Possible role of acetylcholine in regulating spatial novelty effects on theta rhythm and grid cells. *Front Neural Circuits* 6.
- Bartos M, Sauer J-F, Vida I, Kulik Á (2010) Fast and slow GABAergic transmission in hippocampal circuits. In: *Hippocampal Microcircuits* (Cutsuridis V, Graham B, Cobb S, Vida I, eds), pp 129–161. New York: Springer.
- Baude A, Bleasdale C, Dalezios Y, Somogyi P, Klausberger T (2007) Immunoreactivity for the GABAA receptor $\alpha 1$ subunit, somatostatin and connexin36 distinguishes axoaxonic, basket, and bistratified interneurons of the rat hippocampus. *Cereb Cortex* 17:2094–2107.
- Benzi R, Sutera A, Vulpiani A (1981) The mechanism of stochastic resonance. *J Phys Math Gen* 14:L453.
- Berger T, Lüscher H-R, Giugliano M (2006) Transient rhythmic network activity in the somatosensory cortex evoked by distributed input in vitro. *Neuroscience* 140:1401–1413.
- Bezaire MJ, Soltesz I (2013) Quantitative assessment of CA1 local circuits: knowledge base for interneuron-pyramidal cell connectivity. *Hippocampus* 23:751–785.
- Bianchi R, Wong RK (1994) Carbachol-induced synchronized rhythmic bursts in CA3 neurons of guinea pig hippocampus in vitro. *J Neurophysiol* 72:131–138.
- Bower MR, Buckmaster PS (2008) Changes in granule cell firing rates precede locally recorded spontaneous seizures by minutes in an animal model of temporal lobe epilepsy. *J Neurophysiol* 99:2431–2442.
- Boyce R, Glasgow SD, Williams S, Adamantidis A (2016) Causal evidence for the role of REM sleep theta rhythm in contextual memory consolidation. *Science* 352:812–816.

- Brazhnik ES, Vinogradova OS (1986) Control of the neuronal rhythmic bursts in the septal pacemaker of theta-rhythm: effects of anaesthetic and anticholinergic drugs. *Brain Res* 380:94–106.
- Brown JT, Randall AD (2009) Activity-dependent depression of the spike afterdepolarization generates long-lasting intrinsic plasticity in hippocampal CA3 pyramidal neurons. *J Physiol* 587:1265–1281.
- Brunel N, Wang X-J (2003) What determines the frequency of fast network oscillations with irregular neural discharges? I. Synaptic dynamics and excitation-inhibition balance. *J Neurophysiol* 90:415–430.
- Budd JML (2005) Theta oscillations by synaptic excitation in a neocortical circuit model. *Proc Biol Sci* 272:101–109.
- Buhl E, Whittington M (2007) Local circuits. In: *The Hippocampus Book* (Andersen P, Morris R, Amaral D, Bliss T, O'Keefe J, eds), pp 297–320. New York: Oxford University Press.
- Buhl EH, Szilágyi T, Halasy K, Somogyi P (1996) Physiological properties of anatomically identified basket and bistratified cells in the CA1 area of the rat hippocampus in vitro. *Hippocampus* 6:294–305.
- Buzsáki G (2002) Theta oscillations in the hippocampus. *Neuron* 33:325–340.
- Buzsáki G, Wang X-J (2012) Mechanisms of gamma oscillations. *Annu Rev Neurosci* 35:203–225.
- Carnevale NT, Hines ML (2009) *The NEURON Book*. UK: Cambridge University Press.

Cea-del Rio CA, Lawrence JJ, Tricoire L, Erdelyi F, Szabo G, McBain CJ (2010) M3 muscarinic acetylcholine receptor expression confers differential cholinergic modulation to neurochemically distinct hippocampal basket cell subtypes. *J Neurosci* 30:6011–6024.

Cobb S, Lawrence JJ (2010) Neuromodulation of hippocampal cells and circuits. In: *Hippocampal Microcircuits*. (Cutsuridis V, Graham B, Cobb S, Vida I, eds), pp 187–246. New York: Springer.

Colgin LL (2013) Mechanisms and functions of theta rhythms. *Annu Rev Neurosci* 36:295–312.

Crook SM, Ermentrout GB, Bower JM (1998) Spike frequency adaptation affects the synchronization properties of networks of cortical oscillations. *Neural Comput* 10:837–854.

Denham MJ, Borisyuk RM (2000) A model of theta rhythm production in the septal-hippocampal system and its modulation by ascending brain stem pathways. *Hippocampus* 10:698–716.

Destexhe A, Mainen ZF, Sejnowski TJ (1998) Kinetic models of synaptic transmission. *Methods Neuronal Model* 2:1–26.

Eisen JS, Marder E (1984) A mechanism for production of phase shifts in a pattern generator. *J Neurophysiol* 51:1375–1393.

Freeman WJ (1968) Analog simulation of prepyriform cortex in the cat. *Math Biosci* 2:181–190.

Freund TF, Buzsáki G (1998) Interneurons of the hippocampus. *Hippocampus* 6:347–470.

Fuhrmann G, Markram H, Tsodyks M (2002) Spike frequency adaptation and neocortical rhythms. *J Neurophysiol* 88:761–770.

Galán RF, Fourcaud-Trocmé N, Ermentrout GB, Urban NN (2006) Correlation-induced synchronization of oscillations in olfactory bulb neurons. *J Neurosci* 26:3646–3655.

Geiger JR., Lübke J, Roth A, Frotscher M, Jonas P (1997) Submillisecond AMPA receptor-mediated signaling at a principal neuron–interneuron synapse. *Neuron* 18:1009–1023.

Gerstner W, Kistler W, Naud R, Paninski L (2014) *Neuronal Dynamics: From Single Neurons to Networks and Models of Cognition*, 1 edition. Cambridge, United Kingdom: Cambridge University Press.

Getting PA (1989) Emerging principles governing the operation of neural networks. *Annu Rev Neurosci* 12:185–204.

Gillies MJ, Traub RD, LeBeau FEN, Davies CH, Gloveli T, Buhl EH, Whittington MA (2002) A model of atropine-resistant theta oscillations in rat hippocampal area CA1. *J Physiol* 543:779–793.

Giocomo LM, Hussaini SA, Zheng F, Kandel ER, Moser M-B, Moser EI (2011) Grid cells use HCN1 channels for spatial scaling. *Cell* 147:1159–1170.

Gloveli T, Dugladze T, Rotstein HG, Traub RD, Monyer H, Heinemann U, Whittington MA, Kopell NJ (2005) Orthogonal arrangement of rhythm-generating microcircuits in the hippocampus. *Proc Natl Acad Sci USA* 102:13295–13300.

Goutagny R, Jackson J, Williams S (2009) Self-generated theta oscillations in the hippocampus. *Nat Neurosci* 12:1491–1493.

Gulyás AI, Miles R, Sik A, Tóth K, Tamamaki N, Freund TF (1993) Hippocampal pyramidal cells excite inhibitory neurons through a single release site. *Nature* 366:683–687.

Hansel D, Mato G, Meunier C (1995) Synchrony in excitatory neural networks. *Neural Comput* 7:307–337.

Hasselmo M, Schnell E, Barkai E (1995) Dynamics of learning and recall at excitatory recurrent synapses and cholinergic modulation in rat hippocampal region CA3. *J Neurosci* 15:5249–5262.

Hasselmo ME, Fehrlau BP (2001) Differences in time course of ACh and GABA modulation of excitatory synaptic potentials in slices of rat hippocampus. *J Neurophysiol* 86:1792–1802.

Hefft S, Jonas P (2005) Asynchronous GABA release generates long-lasting inhibition at a hippocampal interneuron–principal neuron synapse. *Nat Neurosci* 8:1319–1328.

Henze DA, Wittner L, Buzsaki G (2002) Single granule cells reliably discharge targets in the hippocampal CA3 network in vivo. *Nat Neurosci* 5:790–795.

Hoseini MS, Wessel R (2016) Coherent and intermittent ensemble oscillations emerge from networks of irregular spiking neurons. *J Neurophysiol* 115:457–469.

Hoskison M., Connor J., Shuttleworth C. (2004) GABAB-receptor modulation of short-term synaptic depression at an excitatory input to murine hippocampal CA3 pyramidal neurons. *Neurosci Lett* 365:48–53.

Hosseini-Sharifabad M, Nyengaard JR (2007) Design-based estimation of neuronal number and individual neuronal volume in the rat hippocampus. *J Neurosci Methods* 162:206–214.

Hummos A, Franklin CC, Nair SS (2014) Intrinsic mechanisms stabilize encoding and retrieval circuits differentially in a hippocampal network model. *Hippocampus* 24:1430–1448.

Ishizuka N, Weber J, Amaral DG (1990) Organization of intrahippocampal projections originating from CA3 pyramidal cells in the rat. *J Comp Neurol* 295:580–623.

Izhikevich EM (2003) Simple model of spiking neurons. *IEEE Trans Neural Netw* 14:1569–1572.

Izhikevich EM (2010) *Dynamical systems in neuroscience: the geometry of excitability and bursting*. London: MIT Press.

Jung MW, McNaughton BL (1993) Spatial selectivity of unit activity in the hippocampal granular layer. *Hippocampus* 3:165–182.

Katona I, Acsády L, Freund T. (1999) Postsynaptic targets of somatostatin-immunoreactive interneurons in the rat hippocampus. *Neuroscience* 88:37–55.

Kim D, Paré D, Nair SS (2013a) Assignment of model amygdala neurons to the fear memory trace depends on competitive synaptic interactions. *J Neurosci* 33:14354–14358.

Kim D, Paré D, Nair SS (2013b) Mechanisms contributing to the induction and storage of Pavlovian fear memories in the lateral amygdala. *Learn Mem* 20:421–430.

Kispersky TJ, Fernandez FR, Economo MN, White JA (2012) Spike resonance properties in hippocampal O-LM cells are dependent on refractory dynamics. *J Neurosci* 32:3637–3651.

Klausberger T, Magill PJ, Márton LF, Roberts JDB, Cobden PM, Buzsáki G, Somogyi P (2003) Brain-state- and cell-type-specific firing of hippocampal interneurons in vivo. *Nature* 421:844–848.

Koch C, Segev I (1998) *Methods in neuronal modeling: from ions to networks*. London: MIT Press.

- Kocsis B, Bragin A, Buzsáki G (1999) Interdependence of Multiple Theta Generators in the Hippocampus: a Partial Coherence Analysis. *J Neurosci* 19:6200–6212.
- Kopell N, Börgers C, Pervouchine D, Malerba P, Tort A (2010) Gamma and theta rhythms in biophysical models of hippocampal circuits. In: *Hippocampal Microcircuits* (Cutsuridis V, Graham B, Cobb S, Vida I, eds), pp 423–457. New York: Springer.
- Kosaka T, Katsumaru H, Hama K, Wu JY, Heizmann CW (1987) GABAergic neurons containing the Ca²⁺-binding protein parvalbumin in the rat hippocampus and dentate gyrus. *Brain Res* 419:119–130.
- Kremin T, Hasselmo ME (2007) Cholinergic suppression of glutamatergic synaptic transmission in hippocampal region CA3 exhibits laminar selectivity: Implication for hippocampal network dynamics. *Neuroscience* 149:760–767.
- Lawrence JJ, Statland JM, Grinspan ZM, McBain CJ (2006) Cell type-specific dependence of muscarinic signalling in mouse hippocampal stratum oriens interneurons. *J Physiol* 570:595–610.
- Li G, Amano T, Pare D, Nair SS (2011) Impact of infralimbic inputs on intercalated amygdala neurons: A biophysical modeling study. *Learn Mem* 18:226–240.
- Liljenstrom H, Hasselmo ME (1995) Cholinergic modulation of cortical oscillatory dynamics. *J Neurophysiol* 74:288–297.
- Maccaferri G (2005) Stratum oriens horizontal interneurone diversity and hippocampal network dynamics. *J Physiol* 562:73–80.
- Madison DV, Nicoll RA (1984) Control of the repetitive discharge of rat CA 1 pyramidal neurones in vitro. *J Physiol* 354:319–331.

Marder E (2012) Neuromodulation of neuronal circuits: back to the future. *Neuron* 76:1–11.

McQuiston AR, Madison DV (1999a) Muscarinic receptor activity has multiple effects on the resting membrane potentials of CA1 hippocampal interneurons. *J Neurosci* 19:5693–5702.

McQuiston AR, Madison DV (1999b) Nicotinic receptor activation excites distinct subtypes of interneurons in the rat hippocampus. *J Neurosci* 19:2887–2896.

Miles R (1990) Synaptic excitation of inhibitory cells by single CA3 hippocampal pyramidal cells of the guinea-pig in vitro. *J Physiol* 428:61–77.

Miles R, Wong RK (1986) Excitatory synaptic interactions between CA3 neurones in the guinea-pig hippocampus. *J Physiol* 373:397–418.

Misgeld U, Müller W, Polder HR (1989) Potentiation and suppression by eserine of muscarinic synaptic transmission in the guinea-pig hippocampal slice. *J Physiol* 409:191–206.

Mizuseki K, Buzsáki G (2013) Preconfigured, skewed distribution of firing rates in the hippocampus and entorhinal cortex. *Cell Rep* 4:1010–1021.

Mizuseki K, Royer S, Diba K, Buzsáki G (2012) Activity dynamics and behavioral correlates of CA3 and CA1 hippocampal pyramidal neurons. *Hippocampus* 22:1659–1680.

Naber PA, Caballero-Bleda M, Jorritsma-Byham B, Witter MP (1997) Parallel input to the hippocampal memory system through peri- and postrhinal cortices. *Neuroreport* 8:2617–2621.

Nakao H, Arai K, Nagai K, Tsubo Y, Kuramoto Y (2005) Synchrony of limit-cycle oscillators induced by random external impulses. *Phys Rev E* 72:26220.

Netoff TI, Acker CD, Bettencourt JC, White JA (2005) Beyond two-cell networks: experimental measurement of neuronal responses to multiple synaptic inputs. *J Comput Neurosci* 18:287–295.

Neymotin SA, Hilscher MM, Moulin TC, Skolnick Y, Lazarewicz MT, Lytton WW (2013) Ih tunes theta/gamma oscillations and cross-frequency coupling in an in silico CA3 model. *PloS One* 8:e76285.

Nolan MF, Malleret G, Dudman JT, Buhl DL, Santoro B, Gibbs E, Vronskaya S, Buzsáki G, Siegelbaum SA, Kandel ER, Morozov A (2004) A behavioral role for dendritic integration: HCN1 channels constrain spatial memory and plasticity at inputs to distal dendrites of CA1 pyramidal neurons. *Cell* 119:719–732.

Orbán G, Kiss T, Erdi P (2006) Intrinsic and synaptic mechanisms determining the timing of neuron population activity during hippocampal theta oscillation. *J Neurophysiol* 96:2889–2904.

Pendyam S, Bravo-Rivera C, Burgos-Robles A, Sotres-Bayon F, Quirk GJ, Nair SS (2013) Fear signaling in the prelimbic-amygdala circuit: a computational modeling and recording study. *J Neurophysiol* 110:844–861.

Petsche H, Stumpf C, Gogolak G (1962) The significance of the rabbit's septum as a relay station between the midbrain and the hippocampus. I. The control of hippocampus arousal activity by the septum cells. *Electroencephalogr Clin Neurophysiol* 14:202–211.

Pitler TA, Alger BE (1992) Cholinergic excitation of GABAergic interneurons in the rat hippocampal slice. *J Physiol* 450:127–142.

Rotstein HG, Pervouchine DD, Acker CD, Gillies MJ, White JA, Buhl EH, Whittington MA, Kopell N (2005) Slow and fast inhibition and an H-current interact to create a theta rhythm in a model of CA1 interneuron network. *J Neurophysiol* 94:1509–1518.

Royer S, Zemelman BV, Losonczy A, Kim J, Chance F, Magee JC, Buzsáki G (2012) Control of timing, rate and bursts of hippocampal place cells by dendritic and somatic inhibition. *Nat Neurosci* 15:769–775.

Samarth P, Ball JM, Unal G, Paré D, Nair SS (2016) Mechanisms of memory storage in a model perirhinal network. *Brain Struct Funct* Available at: <http://link.springer.com/10.1007/s00429-016-1210-4> [Accessed March 16, 2016].

Seress L, Pokorny J (1981) Structure of the granular layer of the rat dentate gyrus. A light microscopic and Golgi study. *J Anat* 133:181–195.

Sik A, Penttonen M, Ylinen A, Buzsáki G (1995) Hippocampal CA1 interneurons: an in vivo intracellular labeling study. *J Neurosci* 15:6651–6665.

Springer M, Paulsson J (2006) Biological physics: harmonies from noise. *Nature* 439:27–28.

Staley KJ, Otis TS, Mody I (1992) Membrane properties of dentate gyrus granule cells: comparison of sharp microelectrode and whole-cell recordings. *J Neurophysiol* 67:1346–1358.

Stark E, Eichler R, Roux L, Fujisawa S, Rotstein HG, Buzsáki G (2013) Inhibition-induced theta resonance in cortical circuits. *Neuron* 80:1263–1276.

Stewart M, Fox SE (1990) Do septal neurons pace the hippocampal theta rhythm? *Trends Neurosci* 13:163–168.

- Szabo GG, Holderith N, Gulyas AI, Freund TF, Hajos N (2010) Distinct synaptic properties of perisomatic inhibitory cell types and their different modulation by cholinergic receptor activation in the CA3 region of the mouse hippocampus. *Eur J Neurosci* 31:2234–2246.
- Teramae J, Tanaka D (2004) Robustness of the noise-induced phase synchronization in a general class of limit cycle oscillators. *Phys Rev Lett* 93:204103.
- Tóth K (2010) Glutamatergic neurotransmission in the hippocampus. In: *Hippocampal Microcircuits*. (Cutsuridis V, Graham B, Cobb S, Vida I, eds), pp 99–128. New York: Springer.
- Toth K, Soares G, Lawrence JJ, Philips-Tansey E, McBain CJ (2000) Differential mechanisms of transmission at three types of mossy fiber synapse. *J Neurosci* 20:8279–8289.
- Traub RD, Miles R, Buzsáki G (1992) Computer simulation of carbachol-driven rhythmic population oscillations in the CA3 region of the in vitro rat hippocampus. *J Physiol* 451:653–672.
- Traub RD, Miles R, Wong RK (1989) Model of the origin of rhythmic population oscillations in the hippocampal slice. *Science* 243:1319–1325.
- Vanderwolf CH (1969) Hippocampal electrical activity and voluntary movement in the rat. *Electroencephalogr Clin Neurophysiol* 26:407–418.
- Varela JA, Sen K, Gibson J, Fost J, Abbott LF, Nelson SB (1997) A quantitative description of short-term plasticity at excitatory synapses in layer 2/3 of rat primary visual cortex. *J Neurosci* 17:7926–7940.
- Vida I (2010) Morphology of hippocampal neurons. In: *Hippocampal Microcircuits*. (Cutsuridis V, Graham B, Cobb S, Vida I, eds), pp 27–67. New York: Springer.

- Vinogradova OS (1995) Expression, control, and probable functional significance of the neuronal theta-rhythm. *Prog Neurobiol* 45:523–583.
- Vogt KE, Regehr WG (2001) Cholinergic modulation of excitatory synaptic transmission in the CA3 area of the hippocampus. *J Neurosci* 21:75–83.
- Wang X-J (2010) Neurophysiological and computational principles of cortical rhythms in cognition. *Physiol Rev* 90:1195–1268.
- Wang XJ, Buzsáki G (1996) Gamma oscillation by synaptic inhibition in a hippocampal interneuronal network model. *J Neurosci* 16:6402.
- Witter MP (2010) Connectivity of the hippocampus. In: *Hippocampal Microcircuits*. (Cutsuridis V, Graham B, Cobb S, Vida I, eds), pp 5–26. New York: Springer.
- Wittner L, Henze DA, Záborszky L, Buzsáki G (2006) Hippocampal CA3 pyramidal cells selectively innervate aspiny interneurons. *Eur J Neurosci* 24:1286–1298.
- Wittner L, Henze D, Záborszky L, Buzsáki G (2007) Three-dimensional reconstruction of the axon arbor of a CA3 pyramidal cell recorded and filled in vivo. *Brain Struct Funct* 212:75–83.
- Woolf NJ (1991) Cholinergic systems in mammalian brain and spinal cord. *Prog Neurobiol* 37:475–524.
- Zemankovics R, Káli S, Paulsen O, Freund TF, Hájos N (2010) Differences in subthreshold resonance of hippocampal pyramidal cells and interneurons: the role of h-current and passive membrane characteristics: Impedance characteristics and h-current of hippocampal neurons. *J Physiol* 588:2109–2132.

FIGURES AND LEGENDS

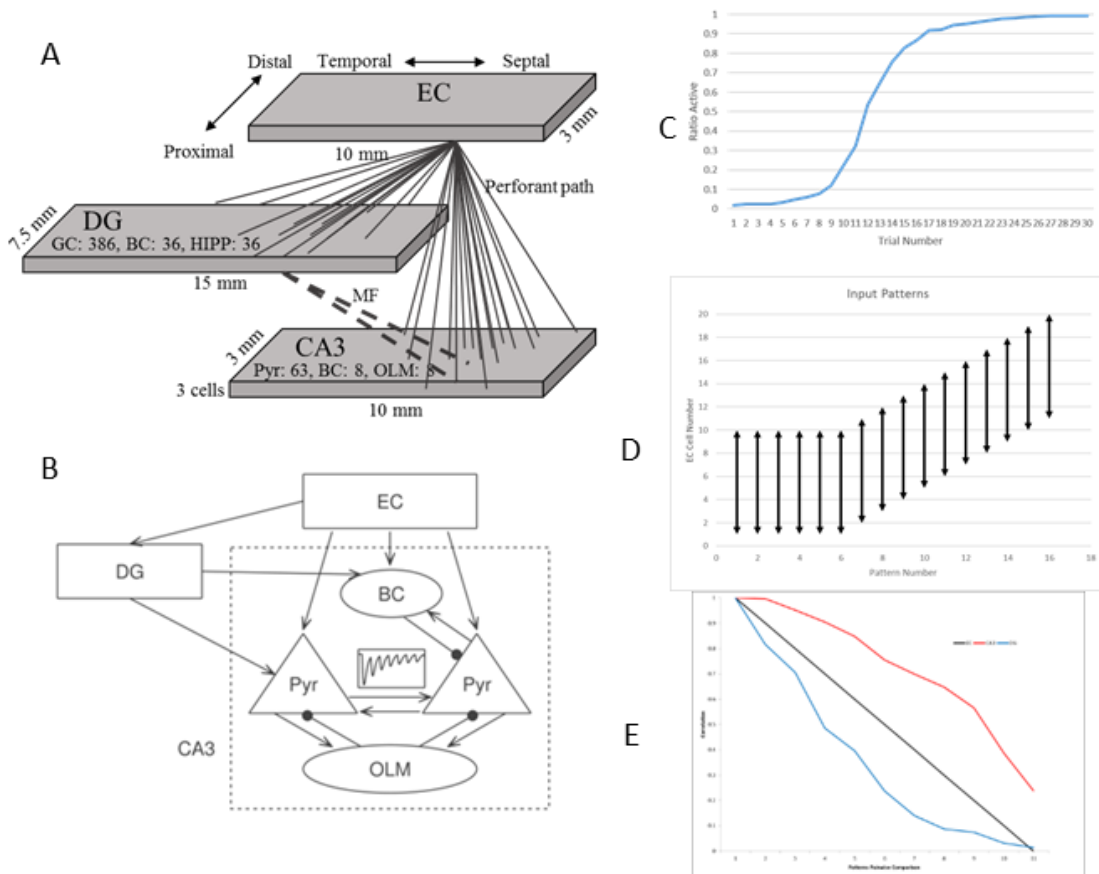


Figure 1:

Network 3D structure and CA3 local circuitry. (A) Schematic of the network implemented showing the modeled regions EC, CA3, and DG with their dimensions, cell numbers, and longitudinally organized connectivity patterns. Neurons in EC were more likely to send connections to DG and CA3 neurons in their longitudinal vicinity. Similarly, DG granule cells tended to project to CA3 neurons with similar EC input. Cells were compacted into three sheets of cells, in the radial dimension, representing stratum-pyramidale in CA3 and the granular layer in DG. (B) Schematic with details of CA3 internal circuitry. Excitatory connections terminate in arrows and inhibitory ones in black filled circles. (C) The ratio of active CA3 pyramidal cells versus the number of EC cells stimulated by external input, without intrinsic stabilizing CA3 mechanisms such as inhibitory interneurons and short-term depression at the CA3 recurrent connections (Hummos et. al., 2014). Using this titration informed choosing a practical number of EC cells to receive external input, to form various patterns of input to the network. Unstable spread of excitation appeared to explode exponentially with more than 10 EC cells receiving external input, and we accordingly, to construct various input patterns to the network, chose 10 different EC cells to receive external input. (D) EC input patterns during training and retrieval modes. (E) Pattern completion in the CA3 region and pattern separation in the DG region.

TABLES AND LEGENDS

Table 1:

bACh: a unit-less value determining the direction and magnitude of ACh effects on synapses (see Materials and Methods).

Table 1: Summary of synaptic properties used in the CA3 network model.

	<i>EC input</i>	<i>Recurrent</i>	<i>Pyr to OLM</i>	<i>Pyr to BC</i>	<i>OLM to pyr</i>	<i>BC to pyr</i>
<i>Spatial connectivity</i>	Diffuse (Witter, 2010)	Homogenous (Wittner, 2007)	Reciprocal (Maccaferri, 2005)	Homogenous (Wittner, 2006)	Dense, compact (Buhl et al., 2007)	Light, diffuse (Buhl et al., 2007)
<i>AMPA or GABA_A rise/decay time constants (ms)</i>	1.7/10.9 (Tóth, 2010) ^a	1.1/5 (Hoskison et al., 2004)	0.27/0.57 (Geiger et al., 1997)	0.27/0.57 (Geiger et al., 1997)	2.8/20.8 (Bartos et al., 2010) ^a	0.21/3.3 (Bartos et al., 2010) ^a
<i>Weight</i>	2	0.4	3	3	3	3
<i>Short-term synaptic plasticity</i>	None	Depressing (Hoskison et al., 2004)	Facilitating (Ali et al., 1998).	Depressing (Ali et al., 1998)	None	Depressing (Hefft et al., 2005).
<i>bACh</i>	-0.5 (Kremin et al., 2007)	-0.85 (Kremin et al., 2007)	None	None	None	-0.5 (Pitler and Alger, 1992)

^a We calculated the rise time constant from the reported 20-80% rise time or 10-90% rise time, see Hummos et al. (2014).

APPENDIX

1. Mathematical Equations for voltage-dependent ionic currents

The equation for each compartment (soma or dendrite) followed the Hodgkin-Huxley formulations (Byrne and Roberts, 2004) in eqn. A1,

$$C_m dV_s/dt = -g_L(V_s - E_L) - g_c(V_s - V_d) - \sum I_{cur,s}^{int} - \sum I_{cur,s}^{syn} + I_{inj} \quad (A1)$$

where V_s/V_d are the somatic/dendritic membrane potential (mV), $I_{cur,s}^{int}$ and $I_{cur,s}^{syn}$ are the intrinsic and synaptic currents in the soma, I_{inj} is the electrode current applied to the soma, C_m is the membrane capacitance, g_L is the is the conductance of leak channel, and g_c is the coupling conductance between the soma and the dendrite (similar term added for other dendrites connected to the soma). The intrinsic current $I_{cur,s}^{int}$, was modeled as $I_{cur,s}^{int} = g_{cur} m^p h^q (V_s - E_{cur})$, where g_{cur} is its maximal conductance, m its activation variable (with exponent p), h its inactivation variable (with exponent q), and E_{cur} its reversal potential (a similar equation is used for the synaptic current $I_{cur,s}^{syn}$ but without m and h). The kinetic equation for each of the gating variables x (m or h) takes the form

$$\frac{dx}{dt} = \frac{x_\infty(V, [Ca^{2+}]_i) - x}{\tau_x(V, [Ca^{2+}]_i)}$$

(A2)

where x_∞ is the steady state gating voltage- and/or Ca^{2+} - dependent gating variable and τ_x is the voltage- and/or Ca^{2+} - dependent time constant. Unless otherwise indicated, x_∞ is equal to $\alpha / (\alpha + \beta)$ and τ_x is equal to $1 / (\alpha + \beta)$ as listed in **Tables 1A-1C**. The equation for the dendrite follows the same format with ‘s’ and ‘d’ switching positions in eqn. A1. The specific current equations and other parameter values for each cell type are provided in **Tables 1A-1C**. For further details on the equations used for synaptic currents, calcium dynamics and Hebbian learning, and short-term plasticity, please refer to our previous study (Hummos et al., 2014).

Table A1: CA3 cell parameter values.

Current	Soma G_{\max}	Dend G_{\max}	Gating Variabl	α	β
I_{Na}	0.031	0.015	p = 3 q = 1	$\frac{0.32(13.1 - v)}{\exp[(13.1 - v)/4] - 1}$ $0.128\exp[(17 - v)/18]$	$\frac{0.28(v - 40.1)}{\exp[(v - 40.1)/5] - 1}$ $\frac{4}{\exp[(40 - v)/5] + 1}$
I_{Kdr}	0.06	0.03	p = 3 q = 1	$\frac{-0.07(v - 47)}{\exp[(v - 47)/-6] - 1}$ $0.001\exp\left[-2(v + 61) \cdot \frac{F}{RT}\right]$	$\frac{0.264}{\exp[(v - 22)/40]}$ 0.001
I_{KCa}	0.0005513 5	0.0005 5	p = 1	$\frac{0.28[Ca^{2+}]}{[Ca^{2+}] + \exp1(0.00048, 0.84, v)}$ $\exp1 = 0.00048\exp\left[-\frac{0.12Fv}{RT}\right]$	$\frac{0.48}{1 + [Ca^{2+}]/\exp1(0.13e^{-6}, 1, v)}$ $\exp1 = 0.13e^{-6}\exp\left[-\frac{Fv}{RT}\right]$
I_M	0.007	0.001	p = 4	$-0.006\exp\left[\left(0.6(v + 55) \cdot \frac{F}{RT}\right)\right]$	$0.06\exp\left[\left(-9.4(v + 55) \cdot \frac{F}{RT}\right)\right]$
I_{CaL}	0.025	0.025	p = 2	$\frac{15.69(81.5 - v)}{\exp[(81.5 - v)/10] - 1}$	$0.29\exp[-v/10.86]$
I_{CaN}	0.01	0.0001	p = 2 q = 1	$\frac{0.1967(19.98 - v)}{\exp[(19.98 - v)/10] - 1}$ $0.00016\exp[-v/48.4]$	$0.046\exp[-v/20.73]$ $\frac{1}{\exp[(39 - v)/10] + 1}$
I_{CaT}	0.0079	0.007	p = 2 q = 1	$\frac{0.2(19.26 - v)}{\exp[(19.26 - v)/10] - 1}$ $0.00016\exp[-v/16.26]$	$0.009\exp[-v/22.03]$ $\frac{1}{\exp[(29.79 - v)/10] + 1}$
I_{KAHP}	0.001	0.0004	p = 1	$1.3 * 10^{13}[Ca^{2+}]_i^4$	0.005
I_A	0.0012	0.001	p = 1 q = 1	$0.02\exp\left[\left(1.8(v + 33.6) \cdot \frac{F}{RT}\right)\right]$ $0.08\exp\left[\left(4(v + 83) \cdot \frac{F}{RT}\right)\right]$	$0.02\exp\left[\left(-1.2(v + 33.6) \cdot \frac{F}{RT}\right)\right]$ 0.08
Diam.	16	3	$C_m =$	$R_{axial} = 210 \Omega\text{-cm}$	$G_{leak} = 0.00018$
Length	16.8	150	$E_{Na} =$	$E_K = -85 \text{ mV}$	$E_{leak} = -70 \text{ mV}$
				$X_{\infty} = \frac{\alpha}{\alpha + \beta}$	$\tau_x \text{ (ms)} = \frac{1}{\alpha + \beta}$

Table A2: DG cell parameter values.

Current Type	Soma G_{\max}	Dend _P G_{\max}	Gating Variable	α	β
I_{Na}	0.08	0.08	$p = 3$ $q = 1$	$\frac{-0.3(v-25)}{\exp[(v-25)/-5] - 1}$ $\frac{0.23}{\exp[(v-3)/20] - 0.07(v-47)}$	$\frac{0.3(v-53)}{\exp[(v-53)/5] - 1}$ $\frac{3.33}{\exp[(v-55.5)/-10] + 1}$
I_{fKdr}	0.04	0.04	$p = 4$	$\frac{\exp[(v-47)/-6] - 1}{-0.028(v-35)}$	$\frac{0.264}{\exp[(v-22)/40]}$
I_{sKdr}	0.13889	0.012	$p = 4$	$\frac{\exp[(v-35)/-6] - 1}{-0.00642Vm - 0.1152}$	$\frac{0.1056}{\exp[(v-10)/40]}$
I_C	0.0001	0.0001	$p = 2$	$\frac{\exp[-(Vm+18)/12] - 1}{Vm = v + 40\log(1000[Ca]_{i2})}$	$1.7\exp[-(Vm+152)/30]$ $Vm = v + 40\log(1000[Ca]_{i2})$
I_{CaL}	0.0004	0.0004	$p = 2$	$\frac{15.69(81.5-v)}{\exp[(81.5-v)/10] - 1}$	$0.29\exp[-v/10.86]$
I_{CaN}	0.0005	0.0005	$p = 2$ $q = 1$	$\frac{0.19(19.98-v)}{\exp[(19.98-v)/10] - 1}$ $0.00016\exp[-v/48.4]$	$0.046\exp[-v/20.73]$ $\frac{1}{\exp[(39-v)/10] + 1}$
I_{CaT}	0.0005	0.0005	$p = 2$ $q = 1$	$\frac{0.19(19.98-v)}{\exp[(19.98-v)/10] - 1}$ $0.00016\exp[-v/48.4]$	$0.046\exp[-v/20.73]$ $\frac{1}{\exp[(39-v)/10] + 1}$
I_{AHP}	0.00005	0.00005	$p = 1$	$\frac{0.0048}{\exp[-0.5(Vm-35)]}$ $Vm = 10\log(1000[Ca]_{i1})$	$\frac{0.012}{\exp[0.2(Vm+100)]}$ $Vm = 10\log(1000[Ca]_{i1})$
I_{KA}	0.005	—	$p = 1$ $q = 1$	$\frac{-0.05(v+25)}{\exp[(v+25)/-15] - 1}$ $\frac{0.00015}{\exp[(v+13)/15]}$	$\frac{0.1(v+15)}{\exp[(v+15)/8] - 1}$ $\frac{0.06}{\exp[(v+68)/-12] + 1}$
Diam.	16	3	$C_m = 1.0$	$R_{axial} = 210 \Omega\text{-cm}$	$G_{leak} = 0.0002$
Length	16.8	150	$E_{Na} = 45$	$E_K = -85 \text{ mV}$	$E_{leak} = -70 \text{ mV}$
$\tau_{[Ca^{2+}]}$	1000	1000	$[Ca^{2+}]_{rest}$	$X_{\infty} = \frac{\alpha}{\alpha+\beta}$	$\tau_x \text{ (ms)} = \frac{1}{\alpha+\beta}$
$\tau_2[Ca^{2+}]$	1	1	$= 50 \text{ nM}$		

Table A3: BC and OLM cell parameter values (*all values for are for both BC and OLM cells unless otherwise indicated*).

Curren	Soma	Dend _p	Gat.	α	β
I_{Na}	BC- 0.12;	BC- 0.12;	p = 3	$\frac{-0.3(v-43)}{\exp[(v-43)/-5]-1}$	$\frac{0.3(v-15)}{\exp[(v-15)/5]-1}$
	OLM- BC- 0.0013;	OLM- BC- 0.0013;	q = 1	$\frac{0.23}{\exp[(v-65)/20]}$	$\frac{3.33}{\exp[(v-12.5)/-10]+1}$
I_{fKdr}	OLM- 0.01	OLM- 0.01	p = 4	$\frac{-0.07(v-47)}{\exp[(v-47)/-6]-1}$	$\frac{0.264}{\exp[(v-22)/40]}$
	BC- 0.0013;	BC- 0.0013;	p = 4	$\frac{-0.028(v-35)}{\exp[(v-35)/-6]-1}$	$\frac{0.1056}{\exp[(v-10)/40]}$
I_{sKdr}	OLM- 0.01	OLM- 0.01	p = 4	$\frac{-0.028(v-35)}{\exp[(v-35)/-6]-1}$	$\frac{0.1056}{\exp[(v-10)/40]}$
I_{KCa} (BC)	0.0002	0.0002	p = 1	$\frac{0.28[Ca^{2+}]}{[Ca^{2+}] + \exp1(0.00048, 0.84, v)}$ exp1 = $0.00048 \exp[-\frac{0.12Fv}{RT}]$	$\frac{0.48}{1 + [Ca^{2+}]/\exp1(0.13e^{-6}, 1, v)}$ exp1 = $0.13e^{-6} \exp[-\frac{Fv}{RT}]$
I_H (OLM)	0.00002	0.00002	p = 1	$X_{\infty} = \frac{1}{\exp[(84.1-v)/10.2]+1}$	$\tau_x \text{ (ms)} = \frac{1}{\exp[0.116v-17.9]+\exp[0.09v-1.84]}$
I_{CaL}	0.09	0.09	p = 2	$\frac{15.69(81.5-v)}{\exp[(81.5-v)/10]-1}$	$0.29 \exp[-v/10.86]$
I_{CaN} (BC)	0.0008	0.0008	p = 2	$\frac{0.19(19.98-v)}{\exp[(19.98-v)/10]-1}$	$0.046 \exp[-v/20.73]$
			q = 1	$0.00016 \exp[-v/48.4]$	$\frac{1}{\exp[(39-v)/10]+1}$
I_{CaT} (OLM)	0.0005	0.0005	p = 2	$\frac{0.2(19.26-v)}{\exp[(19.26-v)/10]-1}$	$0.009 \exp[-v/22.03]$
			q = 1	$0.00016 \exp[-v/16.26]$	$\frac{1}{\exp[(29.79-v)/10]+1}$
I_{KAHP}	0.00002	0.00002	p = 1	$1.25 * 10^{13} [Ca^{2+}]_i^4$	0.00025
I_A	BC- 0.00015	BC- 0.00015	p = 1	$0.02 \exp[(1.8(v+33.6) \cdot \frac{F}{RT})]$	$0.02 \exp[(-1.2(v+33.6) \cdot \frac{F}{RT})]$
	; OLM- ; OLM-	; OLM- ; OLM-	q = 1	$0.08 \exp[(4(v+83) \cdot \frac{F}{RT})]$	0.08
Diam.	BC-15; OLM-	BC-2.5; OLM-3	$C_m =$ BC-	$R_{axial} =$ BC-100; OLM- 150 Ω -cm	$G_{leak} =$ BC-0.0002; OLM- 0.0003
Length	20	BC-	$E_{Na} =$	$E_K = -90$ mV	$E_{leak} = -64$ (BC); -60 (OLM)
				$X_{\infty} = \frac{\alpha}{\alpha+\beta}$	$\tau_x \text{ (ms)} = \frac{1}{\alpha+\beta}$

CHAPTER 5 – SUMMARY

Computational models play an important role in the study of neuroscience. Computational models can involve either single cells or networks. Single cell models can be biologically realistic in which the cell is modeled as an electrical circuit with parameters of the cell and its ionic currents selected to match closely to biological values in an attempt to accurately reproduce the exact behavior of the membrane potential and individual ionic currents.

Computational models can be used to experiment with parameter variation that would be too time consuming to conduct solely with biological experiments. Parameter variation can be done to systematically adjust parameters of each of the ionic currents to determine relationships between individual currents that affect cell behavior. Once relationships are discovered, these specific predictions can be tested with biological experiments to confirm the results. Networks of neuronal nodes can be constructed using synaptic connections to study biological processes and systems involving larger scale structures. These network models give neuroscientists additional tools to analyze biological systems with simultaneous time course data of hundreds or even thousands of neurons and synaptic connections all at once. These network models can be used to study complex biological processes such as fear conditioning and fear extinction in the brain.

CONTRIBUTIONS

Generation and preservation of the slow underlying membrane potential: We have shown that different ionic currents can co-regulate to preserve output function of a neuron. Conductance parameters of pairs of ionic currents can be adjusted together and compensate

for variations in the paired conductance to preserve the output function. Conductances of a pair of opposing currents can be adjusted to preserve the generation of slow underlying membrane oscillations in a cell. Another separate pair of current conductances can be adjusted to preserve the peak height and duration of the membrane oscillation. Yet another separate ionic current can control termination of the oscillation to provide the cell with a mechanism to adjust duration of the oscillation without affecting the height. These current modules can be found in a class of slow wave bursting cells and can help explain how cells can maintain their outputs even with variations in the expressed ionic currents between cells.

Cellular and synaptic correlates of pattern formation in a hippocampal model: We developed a biologically-based model of the hippocampus (CA3 and DG regions) that had realistic single cell models with channel and synaptic dynamics, short- and long-term plasticity, and known effects of neuromodulation provided important insights into the cellular and synaptic correlates of pattern formation. The model enabled quantification of the relative importance of the afferents to a CA3 cell in determining whether it would be part of the pattern. BCs and OLM cells had differential roles in inhibition, with BCs being effective for cells that received higher numbers of inputs from EC, and OLMs for the others. This enabled larger involvement by BCs in selecting CA3 cells that formed part of the pattern, while OLM cells had the more general role of controlling the spread of excitation. The model also shed light on the role of BCs in selecting active pyramidal cells via a disynaptic inhibitory mechanism that involved inputs from both EC and DG regions. We quantified the known effects of back-projections from CA3 to DG and showed reduction of pattern size in CA3. Finally, the biologically-based model provides a test-bed

for studying other phenomena such as oscillations that require high fidelity in modeling the dynamics. Furthermore, the deeper insights into the cellular and synaptic correlates provided by the proposed formulations have applicability to memory formation in other regions of the brain.

Genesis of Hippocampal Theta Rhythm in a Computational Model: The mechanisms involved in the generation of hippocampal theta remain poorly understood. We have outlined the procedure to study the genesis of theta by adapting a computational network model of the rodent hippocampus. The model had biologically realistic conductance-based single cells models for principal cells and the two abundant interneuron types in CA3 and dentate gyrus (DG) regions. The interneuron types were, basket cells (BCs) and oriens lacunosum-moleculare (OLM) interneurons, and the present study incorporated realistic gap junction and chemical synapse connectivity among and between these interneurons. The network model also included synaptic current dynamics, spatial connectivity patterns, short-term synaptic plasticity, and known effects of acetylcholine.

CO-AUTHORSHIP

Three additional works of co-authorship are summarized briefly below. The abstracts of each paper are included in the appendix.

Coregulation of ion channel conductances preserves output in a computational model of a crustacean cardiac motor neuron. A computational model was developed of the crustacean cardiac ganglion using biological data to study coregulation of ion channel conductances. Measurements of mRNA transcripts that encode ion channel proteins revealed correlations between certain channel types. The computational model was used to

determine whether balances of ionic currents from the revealed correlations preserved output of the cell, as determined by certain electrical properties of the cell. A systematic methodology was developed to sample a multidimensional parameter space to select an appropriate model set for meaningful comparison with variations in correlations seen in biological datasets.

Intrinsic mechanisms stabilize encoding and retrieval circuits differentially in a hippocampal network model. A reduced order model of the hippocampus was developed to study context dependent fear conditioning and extinction. The hippocampus is linked to processing contextual information and could play an important role in the context dependence of fear conditioning and extinction. The study involves both network structure and the effects of neuromodulators. The study shows that different regions of the hippocampus can separate novel patterns in a learning mode in one region, while completing similar patterns in a retrieval mode in another region. Whether the memory is stored as a new novel memory context or an old retrieval memory context determines the context dependence of the fear extinction. Neuromodulator levels can control which mode or region is used during this process and therefore control the context dependence of the fear extinction in the hippocampus.

Perceptions of professional skills by graduate students – A comparative study between Engineering, Education and Biology. A survey of graduate students from engineering, biology, and education was administered to determine perceived importance and curriculum coverage of several professional skills, including pedagogy, teamwork and communication, proposal development, and globalization. These responses were analyzed statistically to compare results between departments and between perceived importance

and curriculum coverage. In all professional skill categories, students viewed each skill as more important than it was actually covered in the curriculum, indicating the need for educators to increase curriculum coverage to provide more instruction in these important professional skills. Education students rated pedagogy higher and biology students rated proposal development higher. The study then proposes methods for engineering educators to implement successful strategies from these other areas to further improve and address professional skills in the engineering curriculum to overcome its current inadequate coverage.

APPENDICES

Appendix A1 ---- Coregulation of ion channel conductances preserves output in a computational model of a crustacean cardiac motor neuron

Appendix A2 ---- Intrinsic mechanisms stabilize encoding and retrieval circuits differentially in a hippocampal network model

Appendix A3 ---- Perceptions of Professional Skills by Graduate Students – A Comparative Study between Engineering, Education and Biology

APPENDIX A1

Coregulation of ion channel conductances preserves output in a computational model of a crustacean cardiac motor neuron

Similar activity patterns at both neuron and network levels can arise from different combinations of membrane and synaptic conductance values. A strategy by which neurons may preserve their electrical output is via cell type-dependent balances of inward and outward currents. Measurements of mRNA transcripts that encode ion channel proteins within motor neurons in the crustacean cardiac ganglion recently revealed correlations between certain channel types. To determine whether balances of intrinsic currents potentially resulting from such correlations preserve certain electrical cell outputs, we developed a nominal biophysical model of the crustacean cardiac ganglion using biological data. Predictions from the nominal model showed that coregulation of ionic currents may preserve the key characteristics of motor neuron activity. We then developed a methodology of sampling a multidimensional parameter space to select an appropriate model set for meaningful comparison with variations in correlations seen in biological datasets.

APPENDIX A2

Intrinsic Mechanisms Stabilize Encoding and Retrieval Circuits Differentially in a Hippocampal Network Model

Acetylcholine regulates memory encoding and retrieval by inducing the hippocampus to switch between pattern separation and pattern completion modes. However, both processes can introduce significant variations in the level of network activity and potentially cause a seizure-like spread of excitation. Thus, mechanisms that keep network excitation within certain bounds are necessary to prevent such instability. We developed a biologically realistic computational model of the hippocampus to investigate potential intrinsic mechanisms that might stabilize the network dynamics during encoding and retrieval. The model was developed by matching experimental data, including neuronal behavior, synaptic current dynamics, network spatial connectivity patterns, and short-term synaptic plasticity. Furthermore, it was constrained to perform pattern completion and separation under the effects of acetylcholine. The model was then used to investigate the role of short-term synaptic depression at the recurrent synapses in CA3, and inhibition by basket cell (BC) interneurons and oriens lacunosumoleculare (OLM) interneurons in stabilizing these processes. Results showed that when CA3 was considered in isolation, inhibition solely by BCs was not sufficient to control instability. However, both inhibition by OLM cells and short-term depression at the recurrent CA3 connections stabilized the network activity. In the larger network including the dentate gyrus, the model suggested that OLM inhibition could control the network during high cholinergic levels while depressing synapses at the recurrent CA3 connections were important during low cholinergic states. Our results demonstrate that short-term plasticity

is a critical property of the network that enhances its robustness. Furthermore, simulations suggested that the low and high cholinergic states can each produce runaway excitation through unique mechanisms and different pathologies. Future studies aimed at elucidating the circuit mechanisms of epilepsy could benefit from considering the two modulatory states separately.

APPENDIX A3

Perceptions of Professional Skills by Graduate Students – A Comparative Study between Engineering, Education and Biology

College graduates are increasingly expected to collaborate across disciplines in the modern workplace. In addition to possessing content knowledge, this requires them to be adept in professional skills including written and verbal communication skills, team building and leadership, and to have an understanding of relevant global issues.

A growing awareness exists among educators for the need to better equip students with professional skills for the changing workplace. Student perceptions related to the importance of these topics, and to their coverage in the formal curriculum have, however, not been examined. A comparative study between graduate students from three disciplines (engineering, education and biology) is reported that quantifies these perceptions. A Likert survey was administered to graduate students in engineering, education, and biology, to determine their perceptions of the importance of professional skills to their careers, and whether such skills were addressed in their undergraduate and graduate curricula.

Students from all disciplines rated professional skills as very important, and they also emphasized the lack of attention to these topics in their formal curricula. Engineering students rated pedagogy and interpersonal communication skills and proposal writing lower compared to students in education and biology. Students from engineering, education and biology perceive professional skills as being very important for their careers, and also report inadequate attention to these topics in their curricula. A comparative analysis suggests that engineering could investigate how the other disciplines incorporate content related to some of these important professional skills into their curricula.

PUBLICATIONS, CONFERENCES AND OTHER PRESENTATIONS

Referred Journal papers

Franklin CC, Hummos A, Guntu V, Nair SS (2017) Cellular and synaptic correlates of pattern formation in a hippocampal model (submitted to *Journal of Neurophysiology*)

Hummos A, Franklin CC, Nair SS (2014) Intrinsic mechanisms stabilize encoding and retrieval circuits differentially in a hippocampal network model. *Hippocampus* 24(12): 1430-48.

Franklin CC, Mohan A, Merle D, Lannin J, Nair SS (2012) Perceptions of professional skills by graduate students – A comparative study between Engineering, Education and Biology. *International Journal of Engineering Education* 28(3):588-598.

Franklin CC, Ball JM, Schulz DJ, Nair SS (2010) Generation and preservation of the slow underlying membrane potential oscillation in model bursting neurons. *Journal of Neurophysiology* 104:1589-602.

Ball JM, Franklin CC, Tobin AE, Schulz DJ, SS Nair (2010) Coregulation of ion channel conductances preserves output in a computational model of a crustacean cardiac motor neuron. *Journal of Neuroscience* 30:8637-8649.

In preparation

Guntu VSK, Franklin CC, Hummos A, Nair SS (2017) Genesis of hippocampal theta rhythm in a computational model (in preparation)

NSF GK-12 Lesson Plans

Nair S, Catanho M, Franklin CC, Nair SS (2013) Our Bodies have Computers and Sensors, Curricular Unit #2 with 3 Lessons and 5 Activities, *TEACHEngineering Digital Library* (peer-reviewed resources for K-12; includes powerpoint files, word docs, worksheets and assessments, totaling 200 pages).

Nair A, Upendram K, Franklin CC, Mohan A, Nair SS (2011) Humans are Like Robots, Curricular Unit #1 with 4 Lessons, *TEACHEngineering Digital Library* (peer-reviewed resources for K-12; includes powerpoint files, word docs, worksheets and assessments, totaling 320 pages).

Conference papers and abstracts

Franklin CC, Guntu V, Nair SS (2014) Development of neuronal single cell models for network simulations. *Society for Neuroscience Abstract*, Washington DC.

Franklin CC, Hummos A, Guntu VSK, Nair SS (2012) A biologically realistic computational model of the hippocampus. *Society for Neuroscience Abstract*, New Orleans, LA.

Franklin CC, Chen Y, Guntu VSK, Nair SS (2012) Reduced order modeling of neurons for network simulations,” *Presented to the American Society of Mechanical Engineers Dynamic Systems and Control conference*, p. 597-603, Fort Lauderdale, FL.

Franklin CC, Ball JM, Tobin AE, Schulz DJ, Nair SS (2009) Modeling the role of membrane currents in maintaining the robustness of output in a crab cardiac ganglion. *Society for Neuroscience Poster*, Chicago, IL.

Ball JM, Franklin CC, Tobin AE, Schulz DJ, SS Nair (2009) A combined computational and molecular analysis of a crustacean cardiac motorneuron reveals conductance relationships that may be co-regulated for output maintenance. *Society for Neuroscience Poster*, Chicago, IL.

Ball JM, Franklin CC, Schulz DJ, Nair SS (2008) Co-regulation of calcium and delayed rectifier currents maintains neuronal output in a model of a crustacean cardiac motor neuron. *Presented to the American Society of Mechanical Engineers Dynamic Systems and Control conference*, p. 1449-1456, Ann Arbor, MI.

VITA

Charlie Franklin was born July 13, 1984, in Independence Missouri. He participated in undergraduate research as a freshman under a Discovery Fellowship through the Honors College. He received his B.S. in Electrical and Computer Engineering from the University of Missouri-Columbia in 2007 and graduated Magna Cum Laude. He was a GK-12 Fellow from 2008-2009, during which period he was also a mentor for LEGO-Robotics at Blue Ridge Elementary school (title 1 school) in Columbia, Missouri. His academic background includes computational neuroscience, systems and control. He received his J.D. from the Washington University School of Law in 2013 and currently practices patent law in the area of electrical systems and computer software.